
Retrieval of microphysical properties of desert dust and volcanic ash aerosols from ground-based remote sensing

Josef Konrad Gasteiger



München 2011

Retrieval of microphysical properties of desert dust and volcanic ash aerosols from ground-based remote sensing

Josef Konrad Gasteiger

Dissertation
an der Fakultät für Physik
der Ludwig-Maximilians-Universität
München

vorgelegt von
Josef Konrad Gasteiger
aus Rosenheim

München, den 30. September 2011

Erstgutachter: Prof. Dr. Bernhard Mayer

Zweitgutachter: apl. Prof. Dr. Ulrich Schumann

Tag der mündlichen Prüfung: 6. Dezember 2011

Contents

Abstract	ix
1. Introduction	1
1.1. Volcanic ash aerosols	1
1.2. Desert dust aerosols	2
1.3. Retrieval of microphysical properties	3
1.4. Objectives and outline	6
2. Aerosol properties: definitions, modeling, remote sensing	9
2.1. Microphysical properties of single particles	9
2.1.1. Particle shape	9
2.1.2. Particle size	11
2.1.3. Refractive index	11
2.2. Optical properties of single particles	12
2.2.1. Light as an electromagnetic wave	12
2.2.2. Extinction, scattering, absorption	14
2.2.3. Angular-dependent scattering	15
2.2.4. Backscattering	16
2.3. Modeling optical properties of single particles	17
2.3.1. Mie theory	18
2.3.2. T-matrix method (TMM)	18
2.3.3. Geometric optics method (GOM)	18
2.3.4. Discrete dipole approximation (DDA)	20
2.4. Optical properties of particle ensembles	23
2.4.1. Extinction, scattering, absorption	25
2.4.2. Angular-dependent scattering	26
2.4.3. Backscattering	27
2.5. Radiative transfer modeling	27
2.6. Remote sensing techniques	28
2.6.1. Lidar	28
2.6.2. Sun photometer	31
3. Methods for retrieval of microphysical properties	35
3.1. Bayesian formulation of retrieval problems	35
3.1.1. Determination of model space and priors	36

3.1.2. Monte Carlo sampling	37
3.2. Prerequisite: Optical data sets	38
3.2.1. Data set for spheroids	38
3.2.2. Data set for irregularly-shaped particles	40
3.3. Sensitivity of observed parameters	41
3.3.1. Optical properties of single particles	41
3.3.2. Optical properties of particle ensembles	50
3.3.3. Summary of sensitivity studies	61
3.4. Types of retrievals	62
3.4.1. Bayesian retrieval from lidar observations	62
3.4.2. Retrieval from photometer observations	67
3.4.3. Combined retrieval from lidar and photometer observations	70
4. Results	73
4.1. Ash properties from lidar retrieval	73
4.2. Ash properties from photometer retrieval	77
4.3. Dust properties from combined lidar and photometer retrieval	81
4.3.1. 19 May 2006 (SAMUM-1)	81
4.3.2. 4 June 2006 (SAMUM-1)	85
4.3.3. 29 January 2008 (SAMUM-2)	88
5. Discussion	93
5.1. Ash properties from lidar retrieval	93
5.2. Ash properties from photometer retrieval	94
5.3. Dust properties from combined lidar and photometer retrieval	96
6. Conclusions	99
6.1. Synopsis of findings	99
6.2. Outlook	100
A. Optics of very small particles	103
B. Settings of optical modeling codes	105
C. Modeling of spheroids with ADDA	109
D. Publications containing work from this thesis	111
Bibliography	113
Acknowledgements	125

Zusammenfassung

Aerosolpartikel sind ein wichtiger Bestandteil der Erdatmosphäre. Um die Auswirkungen von Aerosolpartikeln quantitativ bestimmen zu können, müssen deren Verteilung und Eigenschaften bekannt sein. Ein wichtiges Werkzeug für die Bereitstellung solcher Daten ist die Fernerkundung. Die vorliegende Arbeit behandelt vertikal-auflösende Fernerkundung mittels Lidar und vertikal-integrierende Fernerkundung mittels Photometer und berücksichtigt dabei Wüstenstaub-Aerosole, welche für größere Unsicherheiten bei Klimavorhersagen sorgen, ebenso wie Vulkanasche-Aerosole, welche zusätzlich bedeutend für die Flugsicherheit von Düsenflugzeugen sind. Beide Aerosol-Typen bestehen aus Mischungen von Partikeln verschiedener Größe, Form und chemischer Zusammensetzung. Die Ableitung der physikalischen Eigenschaften solcher Mischungen aus Fernerkundungs-Beobachtungen soll in dieser Arbeit verbessert werden, insbesondere durch Nutzung Bayesscher Ansätze und verbesserter Aerosol-Modelle.

Drei Methoden für die Ableitung der physikalischen Eigenschaften wurden entwickelt. Die erste Methode ist auf Lidar-Beobachtungen anwendbar, nimmt Sphäroid-Partikelform an, und basiert auf einem Bayesschen Monte-Carlo-Ansatz. Sie wurde auf Beobachtungen einer reinen Vulkanasche-Schicht aus Island, welche sich am 17. April 2010 über Maisach (Deutschland) befand, angewendet, um deren Massenkonzentration zu bestimmen. Die zweite Methode ist auf Photometer-Beobachtungen in der Aureole der Sonne anwendbar, nutzt einen festgelegten Satz an Mischungen aus unregelmäßig geformten Partikeln und wurde auf Beobachtungen der gleichen Asche-Schicht angewendet. Beide Methoden haben übereinstimmend eine maximale Massenkonzentration der Asche von etwa 1.1 mg m^{-3} über Maisach abgeleitet, mit einem Unsicherheitsbereich von 0.7 bis 1.5 mg m^{-3} . Die dritte Methode sucht Mischungen, die mit Beobachtungen beider Fernerkundungsmethoden übereinstimmen; sie nutzt einen festgelegten Satz an Mischungen, die von der Aerosol-Datenbank OPAC abgeleitet wurden, jedoch aus absorbierenden und nichtabsorbierenden unregelmäßig geformten Partikeln bestehen. Diese Methode wurde erfolgreich auf Saharastaub-Beobachtungen, welche im Rahmen der SAMUM-Messkampagnen in Marokko und auf den Kapverdischen Inseln durchgeführt wurden, angewendet.

Es hat sich gezeigt, dass neben der Partikelform auch das Vorhandensein von nichtabsorbierenden Bestandteilen deutlichen Einfluss auf die Rückstreu-Eigenschaften der Aerosole hat. In Gegensatz dazu sind Strahldichten in der Aureole nur in geringem Maße von der Partikelform und der chemischen Zusammensetzung abhängig, sodass sich Aureolen-Strahldichten sehr gut für die Ableitung der Größe von Asche- und Staub-Partikeln eignen. Es ist zu erwarten, dass sich die Genauigkeit der Methoden für die Ableitung physikalischer Eigenschaften weiter verbessert, wenn alle vom Photometer beobachteten Größen berücksichtigt werden.

Abstract

Aerosol particles are important constituents of the Earth's atmosphere. To quantify effects of aerosol particles, their distribution and properties need to be known. An important tool for the provision of such information is remote sensing. This thesis covers vertically-resolving remote sensing by lidar and vertically-integrating remote sensing by photometer, and thereby considers desert dust aerosols which cause a major uncertainty in climate forecasts, as well as volcanic ash aerosols which, in addition, are relevant for the flight safety of jet-driven aircrafts. Both aerosol types consist of ensembles of particles of varying size, shape, and chemical composition. This thesis aims to improve the retrieval of the physical properties of such mixtures from remote sensing observations, in particular by using Bayesian approaches and improved aerosol models.

Three types of retrievals were developed. The first retrieval type applies to lidar observations, assumes spheroidal particle shapes, and is based on a Bayesian Monte-Carlo-approach. It was applied to observations of a pure volcanic ash plume from Iceland on 17 April 2010 over Maisach (Germany) for the retrieval of the mass concentration of the ash particles. The second retrieval type applies to photometer observations in the solar aureole, uses a pre-defined set of ensembles of irregularly-shaped particles, and was applied to observations of the same ash plume. Both methods consistently retrieved a maximum ash mass concentration of about 1.1 mg m^{-3} over Maisach with an uncertainty range from 0.7 to 1.5 mg m^{-3} . The third retrieval type searches for ensembles that agree with the observations from both remote sensing techniques; it uses a pre-defined set of ensembles derived from the aerosol database OPAC, but consisting of absorbing and non-absorbing irregularly-shaped particles. This approach was successfully applied to Saharan dust observations, which were performed during the SAMUM field campaigns in Morocco and on the Cape Verde islands.

It turned out that, besides the particle shape, also the presence of non-absorbing components strongly influences the backscattering properties of the aerosols. In contrast, aureole radiances are hardly sensitive to particle shape and chemical composition, thus aureole radiances are well-suited for the retrieval of the size of ash and dust particles. It is expected that the accuracy of the retrievals further improves if all parameters observed by photometer are considered.

1. Introduction

Aerosols are small liquid or solid particles suspended in the Earth's atmosphere. They influence the radiative transfer in the atmosphere and, as a consequence, they are directly relevant for the Earth's climate (e.g., Satheesha and Moorthy, 2005). In addition, aerosols have indirect effects on the climate because they modify cloud properties (e.g., Lohmann and Feichter, 2005). Thus, knowledge about the aerosols and their interaction with radiation and clouds is essential for accurate modeling of the Earth's climate.

Remote sensing of aerosols is an important tool to gain such knowledge. For example, vertically-integrated, vertically-resolved, and global information about the aerosol particles can be obtained, depending on the sensing method. The most relevant ground-based aerosol remote sensing techniques are lidars (e.g., Weitkamp, 2005) and Sun photometers (e.g., Holben et al., 1998). Lidars are active remote sensing systems which provide information about the vertical distribution of aerosol particles and their properties, whereas Sun photometers are passive remote sensing systems providing information about columnar aerosol properties. This study aims to retrieve microphysical properties, that is particle size, particle shape, and refractive index, of volcanic ash and desert dust aerosols from lidar and Sun photometer observations. Both aerosol types impose challenges on the retrieval of microphysical properties from remote sensing observations because of their non-spherical shapes and their complex compositions.

1.1. Volcanic ash aerosols

Starting in the 1970's, when first lidar systems were deployed, stratospheric volcanic aerosols over Central Europe, including aerosols from the major eruptions of El Chichón and Pinatubo, have been observed by lidar (Jäger, 2005). Recently, Mattis et al. (2010) reported on multi-wavelength Raman lidar measurements of aerosols in the lower stratosphere over Europe emitted by different volcanoes. Volcanic eruptions emit aerosol particles to the troposphere; only major volcanic eruptions lift particles into the stratosphere. If larger amounts of volcanic aerosols are lifted into the stratosphere, the aerosols can have notable impact on global climate because in the stratosphere they are dispersed on nearly global scales and their residence time is on the order of months to several years. In contrast, the residence time of aerosols in the troposphere is only on the order of several days and its spatial distribution can be quite inhomogeneous, so that the assessment of their radiative effects is much more complicated than for stratospheric aerosols.

The eruption of the Eyjafjallajökull volcano (Iceland) in spring 2010 produced tropospheric aerosols; ash plumes from this eruption were advected to Europe. This offered

a unique opportunity for aerosol science and remote sensing, in particular, because this was the first event where significant amounts of tropospheric volcanic aerosols over large areas in Europe were observed by lidar. Although the Eyjafjallajökull eruption emitted only small amounts of volcanic ash compared to previous major volcanic eruptions, quite soon after the onset of the eruption a further aspect became apparent: Volcanic ash can be melted by jet engines so that it compromises the flight safety of jet-driven aircrafts; engine failures occur if certain amounts of ash are melted and deposited on critical parts of the engines (e.g., Casadevall, 1994; Pieri et al., 2002). For the formation of such deposits, the mass concentration of the ash in the atmosphere is an important parameter. Consequently, as a measure of precaution, air traffic was closed in regions with volcanic ash concentrations exceeding certain thresholds (Gertisser, 2010). The European Aerosol Research Lidar Network (EARLINET, e.g., Bösenberg et al., 2003) showed the potential of detecting volcanic ash plumes by networks of lidar systems (Sanderson, 2010). Reports concerning the dispersion of the plume were provided to the Volcanic Ash Advisory Centers on a hourly to daily basis, but only estimates of the mass concentration were available.

For the assessment of flight safety impacts, the distinction between ash and non-ash particles is necessary. Non-ash particles of volcanic origin are usually liquid particles, predominantly originating from condensation of volcanic gases. Ash particles are solid particles with non-spherical shapes, consisting of glass and crystals from the magma and fragments from the walls of the volcano vent (Mather et al., 2003). The non-sphericity of ash particles allows one to distinguish ash from other aerosol types by means of polarization lidars (Sassen et al., 2007). In case of external mixtures of ash particles with other particles, the contribution of ash particles can be quantified using depolarization lidar observations, if the polarization and backscattering properties of both particle types are known (Ansmann et al., 2011b).

1.2. Desert dust aerosols

Sand deserts, like the Sahara in Northern Africa or Gobi in Asia, are characterized by a low amount of average annual precipitation. Large areas are covered by sand and dust particles. Winds are able to lift particles from the ground. Due to gravitation, large mobilized particles rapidly fall back to ground; due to the viscosity of the air, however, small dust particles are able to stay airborne for much longer and are frequently transported over long distances in the order of several thousand kilometers (Morales, 1979).

The largest sand desert and the strongest source of desert dust aerosols is the Saharan desert located in Northern Africa. Several field campaigns have been performed to investigate the properties and the effects of dust aerosols from the Saharan desert. For example, the Puerto Rico Dust Experiment (PRIDE, June/July 2000) (Reid et al., 2003b) utilized a combination of aircraft and ground-based, in-situ and remote sensing methods, focusing on quantifying the radiative effects of long-range-transported Saharan dust. During PRIDE, dust size distributions simultaneously measured by a variety of aerodynamic, optical, and geometrical methods were quite dissimilar (Reid et al., 2003a). The Saharan Dust Exper-

iment (SHADE, September 2000) (Tanré et al., 2003) utilized a combination of different methods to quantify the direct radiative effect of Saharan dust aerosols on the Cape Verde islands, i.e., closer to the Saharan desert than the PRIDE experiment. The Dust and Biomass-burning Experiment (DABEX) and the African Monsoon Multidisciplinary Analysis Special Observing Period-0 (AMMA-SOP0, January/February 2006) (Haywood et al., 2008) was focused on the interaction between biomass-burning and dust aerosols in the South-Western part of the Sahara and on the consequences for their radiative properties. Furthermore, as part of field campaigns focusing on the climate impact of clouds, Saharan dust properties were measured to investigate their influence on the ice particle formation in clouds (e.g., during CRYSTAL-FACE, Sassen et al., 2003).

The largest mineral dust field campaigns to date are the SAMUM field campaigns (Heintzenberg, 2009; Ansmann et al., 2011a). They were conducted at different distances from the Saharan desert to investigate ageing effects: SAMUM-1 (2006) took place in Morocco close to the Saharan desert, and SAMUM-2 (2008) on the Cape Verde Islands in the Atlantic at a greater distance from the Sahara. Size distributions, optical, hygroscopic, chemical, and morphological characteristics were measured at ground. Research aircrafts measured solar spectral irradiances, surface albedos, in-situ physical properties, and lidar profiles. Dust samples were collected at ground and on the aircrafts. Several ground-based lidars were operated and complemented by Sun photometer measurements. Using these measurements many closure studies are possible. The comprehensive set of dust properties together with the corresponding closure studies allows for almost complete characterization of dust properties (e.g., the climate-relevant properties) and their uncertainties. Parts of this thesis use observations from the SAMUM campaigns (see below).

Closure studies using SAMUM measurements revealed that some Saharan dust properties are still very uncertain. These uncertainties may result from shortcomings of the methods and the underlying theories. For example, the microphysical properties of dust retrieved from the Sun photometer observations can not explain the lidar observations (Müller et al., 2010a), which points to shortcomings of the aerosol models or retrieval techniques. This study tries to improve the aerosol models and retrieval techniques to explain lidar as well as Sun photometer observations from SAMUM.

1.3. Retrieval of microphysical properties

Per definition, remote sensing methods acquire information about an object by observing the object at some distance. In case of aerosol remote sensing, effects due to interaction of light with aerosol particles are observed; a set of optical properties of the aerosol can be obtained from the observations, for example the backscatter or extinction coefficient from lidar observations. It is desirable to extract information about the microphysical properties (size, particle shape, chemical composition) from such observations because the microphysical properties of the aerosols provide the basis for many other applications; for example, the microphysical properties of aerosols are useful for understanding and quantifying their direct climate effects.

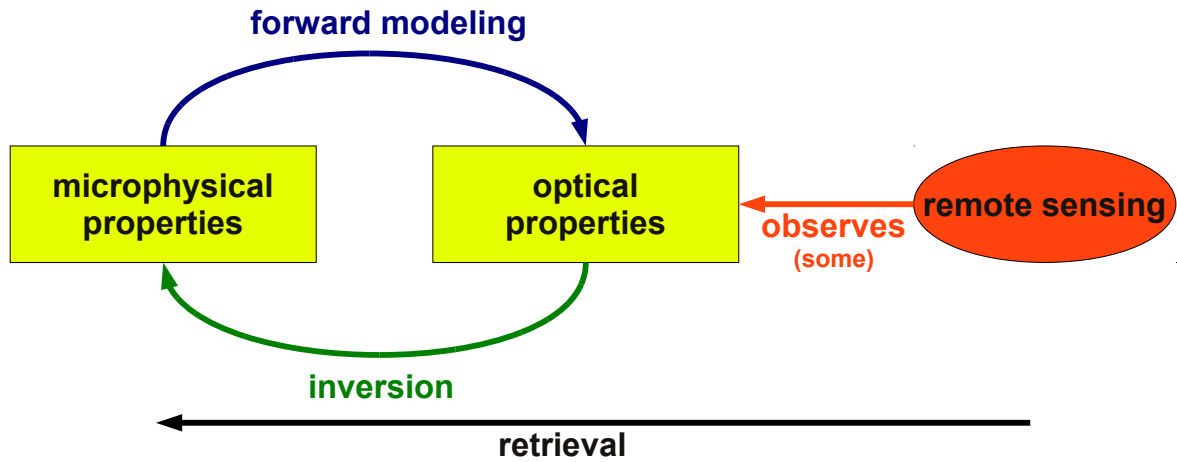


Figure 1.1.: Basic scheme for retrieval of microphysical properties from remote sensing observations.

Figure 1.1 illustrates the basic concept of the retrieval of microphysical properties from remote sensing observations. Forward modeling allows one to calculate the optical properties for known microphysical properties by using physical concepts, e.g., the Mie theory in case of spherical aerosol particles. The retrieval of microphysical properties from remote sensing observations requires one to go in the opposite direction, that is, to find microphysical properties which correspond to the observed optical properties. Different approaches have been used for aerosol retrievals, of which the most relevant are introduced here.

Advanced lidar systems observe the backscatter and the extinction coefficient of the aerosol particles at several wavelengths (Weitkamp, 2005). For the retrieval of microphysical properties from lidar observations, Müller and Quenzel (1985) used a method called *randomized minimization search technique*. They minimized the root mean square difference between modeled and observed optical properties by randomized variation of microphysical aerosol properties. More recently, regularization techniques were proposed for the inversion of lidar data (e.g., Müller et al., 1999; Böckmann and Wauer, 2001; Veselovskii et al., 2010; Osterloh et al., 2011). In principle, regularization techniques find microphysical properties that best agree with the lidar observations.

Multi-wavelength Sun photometry provides information about the wavelength dependence of the extinction of sunlight by the vertical aerosol column (e.g., Shaw, 1983). Sun photometers are, in addition, often used as sky radiometers, which measure spectral sky radiances from several directions, providing further information about the aerosols. For example, the presence of particles with sizes comparable or larger than the wavelength in the atmosphere causes a bright zone around the solar disc, which is known as the aureole of the Sun. The aureole is a result of diffraction of sunlight by the particles. The angular width of the main diffraction peak, which is around the forward scattering direction $\theta = 0^\circ$,

primarily depends on the ratio between particle size and wavelength (van de Hulst, 1981). Thus, aureole observations provide information about the size of the particles. Several authors investigated the possibility of retrieving size distributions from such observations (e.g., Shaw, 1979; Deepak et al., 1982; O'Neill and Miller, 1984). Thomalla and Quenzel (1982) applied the above-mentioned randomized minimization search technique to investigate the information content of forward scattering and extinction observations. Nakajima et al. (1983) and Dubovik et al. (2006) developed minimization methods for the retrieval of microphysical properties from Sun/sky photometer observations; the method of Dubovik et al. (2006) considers the non-sphericity of particles by assuming spheroidal dust particles, whereas spherical particles were assumed by the other authors. Nakajima et al. (1983) used the *constrained linear method of inversion*, whereas Dubovik et al. (2006) used a so-called *multiterm Least Squares Method* for solving a combined system of equations that describe the retrieval problem.

A basic principle of minimization methods is that they find microphysical properties that provide a minimum for the deviation from the observations (different metrics for the deviation are used by the different approaches). From the physical point of view, however, it is reasonable to accept all physically meaningful solutions that agree with the observations. Thus, a different approach for the search for solutions is attractive: The retrieval of microphysical aerosol properties from observations can be done by modeling a prior set of aerosol ensembles and by comparing their optical properties to the observations. Those ensembles that reproduce the observations within their uncertainty ranges are the solutions of the retrieval; they constitute the posterior set of aerosol ensembles. The retrieval techniques developed in this study are based on this approach. It is compatible to Bayesian inference (Mosegaard and Tarantola, 2002; Tarantola, 2006) which uses evidence (here: observations) to update beliefs (here: probabilities that the microphysical properties agree with the observations). A Bayesian approach for the retrieval of physical aerosol properties from lidar data has previously been used only by Herman et al. (2008) (for spherical aerosols).

For the retrieval of microphysical properties from observations, the relationship between microphysical and optical properties has to be known from optical modeling (forward modeling, see Fig. 1.1). Desert dust and volcanic ash aerosols consist of particles with a large variety of microphysical properties, i.e. having different sizes, shapes, and chemical composition (e.g., Kandler et al., 2009; Schumann et al., 2011). This makes forward modeling a challenging task (Kalashnikova and Sokolik, 2004; Nousiainen, 2009) because of the large number of free parameters and the computational requirements; until recently, most retrieval approaches assumed that the particles are spherical, which simplifies the forward modeling considerably. The non-sphericity of the particles is known to have substantial effects for the scattering in side- and backward direction (e.g., Mishchenko et al., 1997); consequently it needs to be considered for accurate interpretation of most remote sensing observations. For example, to investigate the applicability of spheroids for modeling the lidar-relevant optical properties of Saharan dust, Wiegner et al. (2009) used information about the microphysical aerosol properties from SAMUM-1 in-situ measurements and electron microscopy as input for optical modeling. The comparison of modeled optical

properties with SAMUM-1 lidar observations showed that the consideration of the particle non-sphericity improves the agreement with the observations considerably, but the spectral dependence of the lidar-relevant optical properties was not satisfactorily captured. Furthermore, most modeling studies and retrieval approaches assume that all particles of an aerosol ensemble have the same refractive index. An investigation of the relevance of the mineralogical inhomogeneity of dust and ash particles for aerosol retrievals is still lacking. It is known, however, that an adequate treatment of this inhomogeneity is crucial for assessing the radiative effects of mineral dust (Sokolik and Toon, 1999).

1.4. Objectives and outline

The main objective of this thesis is the retrieval of optical and microphysical properties of volcanic ash and desert dust aerosols from lidar and Sun photometer observations, considering the physical particle properties as realistically as possible. The mass concentration of volcanic ash aerosols is a critical parameter for flight safety, thus for the volcanic ash retrievals in this thesis, special emphasis is on the mass concentration. For the retrieval of desert dust aerosol properties, in principle, their climate-relevant optical properties are of greatest interest; however, this thesis focuses on the microphysical properties of dust which provide the basis for understanding and quantifying their climate-relevant optical properties.

Basic concepts of treating aerosols in the framework of remote sensing are introduced in Chapter 2. It starts with the definition of microphysical and optical aerosol properties of single particles, and describes concepts for modeling their optical properties. Subsequently, properties of aerosol ensembles (mixtures of different particles) are defined and methods for modeling the radiative transfer in the atmosphere are introduced. As the final point of this chapter, the lidar and the Sun photometer remote sensing techniques are described.

Chapter 3 describes methods for the retrieval of microphysical properties from remote sensing observations. First, the approach of a Bayesian retrieval is described in general. For aerosol retrievals, the optical properties of a large number of different single particles are required. Thus, data sets containing the required optical properties are established and introduced subsequently. To better characterize the capabilities and limitations of the retrievals, as well as the effect of assumptions on the retrievals, the relationship between optical and microphysical properties is subsequently investigated in detail. Finally, depending on the availability of remote sensing platforms and the aerosol situation (vertical structure, complexity of the aerosol microphysical properties) three types of retrievals are developed.

In Chapter 4, the different types of retrievals are applied to remote sensing observations. A retrieval type, which is based on the Bayesian idea using a Monte Carlo sampling approach, is applied to lidar observations of a pure volcanic ash plume from the Eyjafjallajökull volcano over Maisach (Southern Germany) on 17 April 2010; subsequently, an independent retrieval type is applied to observed aureole radiances of the same volcanic ash plume; both retrieval types retrieve the mass concentrations of the ash. Finally, a third

retrieval type is applied to collocated lidar and Sun photometer observations from the SAMUM field campaigns in Morocco (2006, SAMUM-1) and Cape Verde (2008, SAMUM-2) and, in addition, closure studies are performed using size distributions available from independent sources in the framework of SAMUM.

Chapter 5 discusses the results from the three types of retrievals on the basis of the relationship between optical and microphysical properties which was investigated in Chapter 3.

This thesis ends in Chapter 6 with a synopsis of the findings and suggestions for future improvements of the retrievals.

2. Aerosol properties: definitions, modeling, remote sensing

This chapter starts with the definition of microphysical and optical properties of single particles. Then, theories for modeling optical properties of single particles are introduced; they provide the link between microphysical and optical properties. Atmospheric aerosols are mixtures of many different particles, thus, the properties of aerosol ensembles are defined in the next step. Several aerosol remote sensing techniques are affected by multiple scattering effects; radiative transfer modeling, which is introduced subsequently, is required for the interpretation of observations by such techniques. Finally, ground-based aerosol remote sensing techniques are described, that is the lidar technique and Sun photometry.

2.1. Microphysical properties of single particles

The microphysical properties of an aerosol particle are its shape, size, and chemical composition. The chemical composition of a particle determines its complex refractive index m . The shape, size, and the refractive index m of a particle determine its optical properties.

2.1.1. Particle shape

Many types of aerosol particles are liquid and, as a result of surface tension, their shape is spherical. Desert dust and volcanic ash particles, however, are solid particles with non-spherical shapes. These aerosols typically consist of particles having a large variety of different shapes. Samples of such particles are shown in Fig. 2.1.

2.1.1.1. Spheroids

Idealized particle shapes need to be assumed for optical modeling of non-spherical aerosol types. Spheroids are frequently assumed. They originate from rotation of ellipses about one of their axes. Rotation about the minor axis creates an oblate spheroid, whereas rotation about the major axis results in a prolate spheroid. Spheroids allow for the consideration of the particles' non-sphericity while adding only one additional microphysical parameter compared to spherical particles, that is the ratio ϵ between the rotational axis and the axis perpendicular to it (Dubovik et al., 2006). As an alternative parameter, the aspect ratio ϵ' can be used for the full characterization of the shape of an oblate or a prolate spheroid. The aspect ratio ϵ' is the ratio of the major to the minor axis ($\epsilon' \geq 1$). For oblate spheroids $\epsilon' = \epsilon$, and for prolate spheroids $\epsilon' = 1/\epsilon$. Spheroids with $\epsilon = \epsilon' = 1$ are spheres.

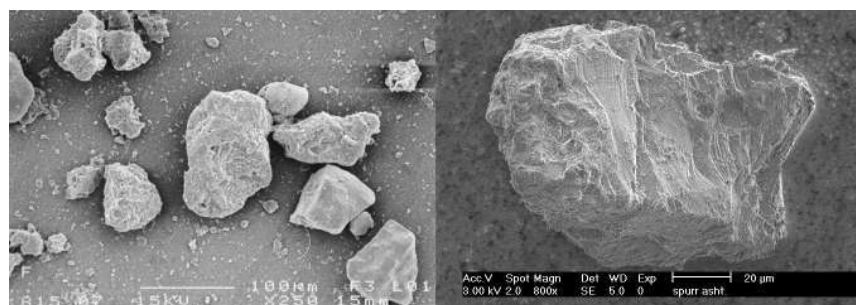


Figure 2.1.: Scanning Electron Microscope images of desert dust particles (left) from the Saharan desert and a volcanic ash particle (right) from Spurr Ashton (provided by *The Amsterdam-Granada Light Scattering Database*, <http://www.iaa.es/scattering>).

2.1.1.2. Irregular shapes

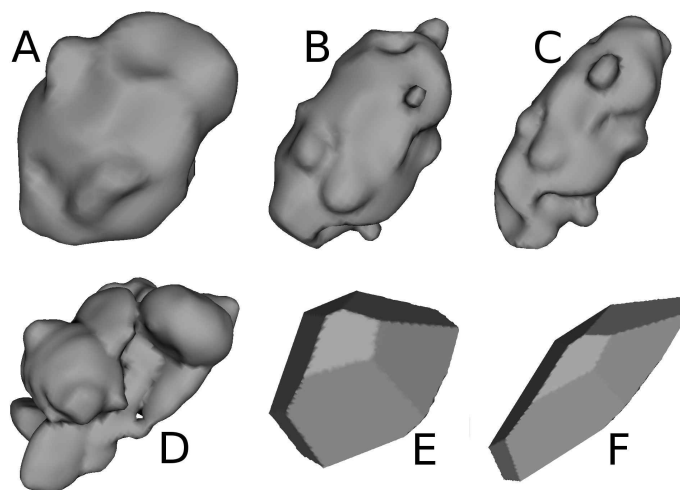


Figure 2.2.: Irregularly-shaped particles for optical modeling.

Potential optical effects of shape irregularities like surface deformations, aggregation, or edges, can not be modeled using spheroids. Irregularities, however, are present in desert dust and volcanic ash particles as shown in Fig. 2.1 and by Kandler et al. (2009); Kandler et al. (2011); Schumann et al. (2011). The six irregular shapes shown in Fig. 2.2 were created to consider shape irregularities for the optical modeling in this thesis. Shapes A, B, and C are prolate spheroids with surface deformations according to the Gardner series (Gardner, 1984). The aspect ratios ϵ' of the original spheroids of shapes A, B, and C are 1.4, 1.8, and 2.4, respectively. Shape D is an aggregate particle, consisting of overlapping ellipsoids, again with surface deformations according to the Gardner series. The spheroid

equivalent of shape D is a prolate spheroid with $\epsilon' \approx 1.8$. Shapes E and F have flat surfaces and edges. The spheroid equivalent of shape E is an oblate spheroid with $\epsilon' \approx 1.3$; the deviation of shape E from spherical shape is smaller than for the other shapes in Fig. 2.2. Shape F is derived from shape E by stretching the particle by a factor of 2 in one dimension, and it may be approximated by a prolate spheroid with $\epsilon' \approx 2.3$. More details about the particle creation are given in Appendix B.

2.1.2. Particle size

The specification of the size of a spherical particle is straightforward; typically, its radius r or its diameter D is used for this. For a non-spherical particle, the definition of its size is not as straightforward; the size of an equivalent sphere is often used. The volume-equivalent radius of a particle with volume V is given as

$$r_v = \sqrt[3]{\frac{3V}{4\pi}}, \quad (2.1)$$

whereas the cross-section-equivalent radius of a particle with the orientation-averaged geometric cross sectional area C_{geo} is

$$r_c = \sqrt{\frac{C_{\text{geo}}}{\pi}}. \quad (2.2)$$

For the conversion between r_v and r_c , the radius conversion factor

$$\xi_{\text{vc}}^3 = \left(\frac{r_v}{r_c}\right)^3 = \frac{3\sqrt{\pi}}{4} \frac{V}{C_{\text{geo}}^{3/2}} \quad (2.3)$$

is used. ξ_{vc}^3 is equal to 1 in case of spheres because for spheres r_v is equal to r_c . ξ_{vc}^3 decreases with increasing deviation from spherical shape because the spherical shape is the most compact shape. The radius conversion factor ξ_{vc}^3 depends only on the shape of a particle, which means that isotropic scaling of a particle does not change ξ_{vc}^3 . For spheroids, analytical equations for ξ_{vc}^3 are available, e.g., in the code described by Mishchenko and Travis (1998).

In this study, the cross-section-equivalent radius r_c is used for the specification of the particle size because C_{geo} is the primary parameter for extinction of light by particles larger than the wavelength (Hansen and Travis, 1974).

2.1.3. Refractive index

The refractive index m depends on the chemical composition of the particle and on the wavelength λ of the light. m is a complex number:

$$m = m_r + m_i i \quad (2.4)$$

The real part m_r determines the phase velocity c of the light inside the particle:

$$c = c_0/m_r, \quad (2.5)$$

where c_0 is the speed of light in vacuum. m_r is larger than unity for aerosol particles at solar wavelengths, thus light inside the particles is slower than c_0 .

The imaginary part m_i is responsible for the absorption of the light of (vacuum-)wavelength λ inside the particle. α_{abs} describes the absorption per unit length. It can be calculated from m_i by

$$\alpha_{\text{abs}} = \frac{4\pi m_i}{\lambda}. \quad (2.6)$$

The absorbed light is primarily transformed into heat, or it may be re-emitted at other wavelengths (Raman scattering). Eq. 2.6 is only applicable inside a homogeneous particle or medium.

2.2. Optical properties of single particles

The optical properties of a particle describe the interaction of light with the particle. In the following, it is assumed that the particles are randomly-oriented.

2.2.1. Light as an electromagnetic wave

The basis for describing light is the classical electromagnetic theory. An oscillating electric field together with the corresponding magnetic field form an electromagnetic wave. The electric and magnetic fields are linked to each other by the Maxwell's equations. The electric field of a plane electromagnetic wave with wavelength λ , propagating along the z -axis of a cartesian reference system, is given by

$$\begin{aligned} E_x(z, t) &= E_{x,0} \exp[-i(kz - \omega t + \delta_x)] \\ E_y(z, t) &= E_{y,0} \exp[-i(kz - \omega t + \delta_y)]. \end{aligned} \quad (2.7)$$

E_x is the x -component of the electric field and $E_{x,0}$ is the amplitude of the x -component. $k = 2\pi/\lambda$ is the wave number, $\omega = 2\pi c/\lambda$ the circular frequency, and δ_x the phase of the x -component. Subscripts y indicate the corresponding properties of the y -components. c is the phase velocity. The power of an electromagnetic wave is proportional to the square of its amplitude.

Stokes parameters I , Q , U and V describe the power and the polarization state of a wave (van de Hulst, 1981):

$$\begin{aligned} I &= E_{x,0}^2 + E_{y,0}^2 \\ Q &= E_{x,0}^2 - E_{y,0}^2 \\ U &= 2E_{x,0}E_{y,0} \cos \delta \\ V &= 2E_{x,0}E_{y,0} \sin \delta, \end{aligned} \quad (2.8)$$

where $\delta = \delta_x - \delta_y$ is the phase difference between both components. Based on these parameters the Stokes vector \mathbf{I} is defined as

$$\mathbf{I} = \begin{bmatrix} I \\ Q \\ U \\ V \end{bmatrix}. \quad (2.9)$$

Physically, I is proportional to the total power, whereas Q , U , and V contain the information about the polarization state. Polarization states of waves with different Stokes

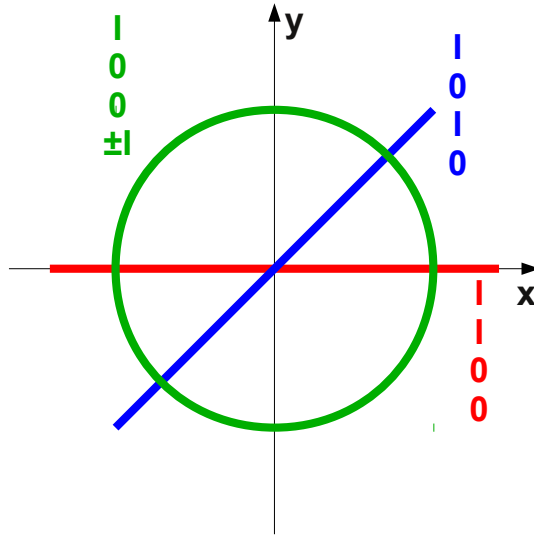


Figure 2.3.: Electric fields of different Stokes vectors \mathbf{I} (different colors) in x - y plane; the direction of propagation is perpendicular to this plane.

vectors are illustrated in Figure 2.3. The field shown in red is oscillating along the x -axis, thus $E_{y,0} = 0$, and $Q = I$, $U = 0$, and $V = 0$. The field shown in blue is rotated by 45° compared to the field shown in red; the x - and the y -component of this field is always equal and the phase difference δ is zero; thus $Q = 0$, $U = I$, and $V = 0$. Finally, the field shown in green is rotating along a circle, which means that $E_{x,0} = E_{y,0}$ and $\delta = \pm 90^\circ$; thus $Q = 0$, $U = 0$, and $V = \pm I$. Q can be interpreted as the dominance of the x -component over the y -component, U as the dominance of the 45° -direction over the 135° -direction, and V as the dominance of the right-handed circular polarization over the left-handed circular polarization. Three quantities of the Stokes parameters do not change, if the x - y -plane is rotated about the z -axis: I , $Q^2 + U^2$, and V . The term $\sqrt{Q^2 + U^2}/I$ is the degree of linear polarization, and $|V|/I$ is the degree of circular polarization. As waves are always polarized, $I^2 = Q^2 + U^2 + V^2$, and the field of each wave can be described by a superposition of the fields shown in red, blue, green, and the fields perpendicular to them.

Typically, light is a superposition of many plane electromagnetic waves; as a consequence, superpositions of waves and 'effective' Stokes vectors are observed by remote sensing instruments. For example, sunlight is unpolarized light which means that it is a superposition of a large number of electromagnetic waves with random polarization. This implies the average $E_{x,0}$ to be equal to the average $E_{y,0}$, and the average values of $\cos \delta$ and $\sin \delta$ to be zero; the Stokes vector \mathbf{I} for unpolarized light is

$$\mathbf{I} = \begin{bmatrix} I \\ 0 \\ 0 \\ 0 \end{bmatrix}. \quad (2.10)$$

Lidar systems (see below) emit linearly-polarized light, which means that all emitted waves are linearly polarized and their fields oscillate in the same plane. If the x - y -plane is rotated such that the fields oscillate in x -direction, the Stokes vector of the emitted waves is

$$\mathbf{I} = \begin{bmatrix} I \\ I \\ 0 \\ 0 \end{bmatrix}. \quad (2.11)$$

2.2.2. Extinction, scattering, absorption

The optical properties of a randomly-oriented particle at wavelength λ are fully described by the extinction cross section C_{ext} , the scattering cross section C_{sca} , and the scattering matrix $\mathbf{F}(\theta)$, which depends on the scattering angle θ . These parameters are discussed in the following. From C_{ext} and C_{sca} , the absorption cross section C_{abs} of a particle can be calculated by $C_{\text{abs}} = C_{\text{ext}} - C_{\text{sca}}$ because the extinguished light is either scattered or absorbed by the particle.

The units of C_{ext} , C_{sca} , and C_{abs} are areas; the power P_{ext} removed from incident parallel light of irradiance I_r (defined as power per area perpendicular to propagation direction) is $P_{\text{ext}} = I_r \cdot C_{\text{ext}}$; the power $P_{\text{sca}} = I_r \cdot C_{\text{sca}}$ is scattered without a change of wavelength (elastic scattering), and $P_{\text{abs}} = I_r \cdot C_{\text{abs}}$ is absorbed by the particle. The cross sections are related to the geometrical cross section C_{geo} of the particle by the extinction efficiency q_{ext} , the scattering efficiency q_{sca} , and the absorption efficiency q_{abs} :

$$q_{\text{ext/sca/abs}} = \frac{C_{\text{ext/sca/abs}}}{C_{\text{geo}}} \quad (2.12)$$

The single scattering albedo ω_0 is defined as the ratio between scattering and extinction by a particle:

$$\omega_0 = \frac{C_{\text{sca}}}{C_{\text{ext}}} = \frac{q_{\text{sca}}}{q_{\text{ext}}}. \quad (2.13)$$

As a consequence, $(1 - \omega_0)$ is the ratio between absorption and extinction, which is relevant for the heating of particles by incident light.

2.2.3. Angular-dependent scattering

The scattering matrix $\mathbf{F}(\theta)$, also called Müller matrix, contains the angular-dependent and polarization-dependent information about the light scattered by a particle. θ is defined as the angle between the scattered and the incident direction of the light. As randomly-oriented particles are assumed, the scattered light does not depend on the azimuth direction ϕ of scattering. $\mathbf{F}(\theta)$ transforms the incident Stokes vector \mathbf{I}^{inc} to the scattered Stokes vectors $\mathbf{I}^{\text{sca}}(\theta)$:

$$\mathbf{I}^{\text{sca}}(\theta) = \frac{C_{\text{sca}}}{4\pi R^2} \mathbf{F}(\theta) \mathbf{I}^{\text{inc}} \quad (2.14)$$

Here, R is the distance from the scattering particle. The reference systems (Sect. 2.2.1) of \mathbf{I}^{inc} and \mathbf{I}^{sca} are selected such that the x - and z -axes of both systems are in a single plane, the *scattering plane*. Equation 2.14 is valid in the far-field of the particle (radius $r \ll R$). For randomly-oriented particles, the scattering matrix contains six independent elements (van de Hulst, 1981):

$$\mathbf{F}(\theta) = \begin{bmatrix} F_{11}(\theta) & F_{12}(\theta) & 0 & 0 \\ F_{12}(\theta) & F_{22}(\theta) & 0 & 0 \\ 0 & 0 & F_{33}(\theta) & F_{34}(\theta) \\ 0 & 0 & -F_{34}(\theta) & F_{44}(\theta) \end{bmatrix} \quad (2.15)$$

The scattering matrix fulfills the following conditions in exact forward ($\theta = 0^\circ$) and backward ($\theta = 180^\circ$) direction:

$$\begin{aligned} F_{33}(0^\circ) &= F_{22}(0^\circ), \\ F_{33}(180^\circ) &= -F_{22}(180^\circ), \\ F_{12}(0^\circ) &= F_{34}(0^\circ) = F_{12}(180^\circ) = F_{34}(180^\circ) = 0, \\ F_{44}(180^\circ) &= F_{11}(180^\circ) - 2 \cdot F_{22}(180^\circ). \end{aligned} \quad (2.16)$$

In case of spherical particles, the scattering matrix fulfills the following additional conditions at any scattering angle θ :

$$\begin{aligned} F_{22}(\theta) &= F_{11}(\theta), \\ F_{44}(\theta) &= F_{33}(\theta). \end{aligned} \quad (2.17)$$

Thus, only four independent scattering matrix elements exist in case of spherical particles. The element $F_{11}(\theta)$ is also known as the phase function. It is a measure for the angular distribution of the scattered light. The phase function is normalized such that the integral over all scattering angles is

$$\int_{0^\circ}^{180^\circ} \int_{0^\circ}^{360^\circ} F_{11}(\theta) \cdot \sin \theta \cdot d\phi \cdot d\theta = 4\pi. \quad (2.18)$$

Thus, the phase function of an isotropic scatterer is $F_{11}(\theta) = 1$. The differential scattering cross section $C_{\text{diffsca}}(\theta)$ is

$$C_{\text{diffsca}}(\theta) = \frac{1}{4\pi} \cdot C_{\text{sca}} \cdot F_{11}(\theta), \quad (2.19)$$

and the power per solid angle scattered by the particle to angle θ is $P_{\text{diffsca}}(\theta) = I_r \cdot C_{\text{diffsca}}(\theta)$. The integral of $C_{\text{diffsca}}(\theta)$ over all scattering angles is

$$\int_{0^\circ}^{180^\circ} \int_{0^\circ}^{360^\circ} C_{\text{diffsca}}(\theta) \cdot \sin \theta \cdot d\phi \cdot d\theta = C_{\text{sca}}. \quad (2.20)$$

The differential scattering efficiency $q_{\text{diffsca}}(\theta)$ is given by

$$q_{\text{diffsca}}(\theta) = \frac{C_{\text{diffsca}}(\theta)}{C_{\text{geo}}} = \frac{1}{4\pi} \cdot q_{\text{sca}} \cdot F_{11}(\theta). \quad (2.21)$$

A commonly-used parameter, derived from the phase function $F_{11}(\theta)$, is the asymmetry parameter

$$g = \frac{1}{2} \int_{0^\circ}^{180^\circ} \cos \theta \cdot F_{11}(\theta) \cdot \sin \theta \cdot d\theta. \quad (2.22)$$

The asymmetry parameter g is the average cosine of the scattering angle of the scattered light. With increasing g , the main scattering direction moves into the forward scattering direction. Together with the extinction and the single scattering albedo, the asymmetry parameter g is an important integrated parameter for the radiative transfer in aerosol layers.

2.2.4. Backscattering

For lidar applications, the extinction and the scattering properties in the backward direction are relevant. The scattering matrix \mathbf{F} of randomly-oriented particles has, as a consequence of Eq. 2.16 only two independent parameters in the backward direction:

$$\mathbf{F}(180^\circ) = \begin{bmatrix} F_{11}(180^\circ) & 0 & 0 & 0 \\ 0 & F_{22}(180^\circ) & 0 & 0 \\ 0 & 0 & -F_{22}(180^\circ) & 0 \\ 0 & 0 & 0 & F_{11}(180^\circ) - 2F_{22}(180^\circ) \end{bmatrix} \quad (2.23)$$

While the phase function $F_{11}(180^\circ)$ is relevant for the power, a second parameter (e.g., described by $F_{22}(180^\circ)/F_{11}(180^\circ)$) is relevant for the polarization state of the backscattered light. In case of spherical particles, as a result of Eq. 2.17, $\mathbf{F}(180^\circ)$ is described by only one independent parameter, the phase function $F_{11}(180^\circ)$.

The lidar ratio, defined as

$$S = \frac{q_{\text{ext}}}{q_{\text{diffsca}}(180^\circ)} = \frac{4\pi}{\omega_0 \cdot F_{11}(180^\circ)} \quad (2.24)$$

for a single particle, is an important parameter for lidar applications because it relates the extinction (relevant for the radiative transfer) to the backscattering (primary parameter observed by lidar).

The depolarization parameter is defined as

$$d = 1 - \frac{F_{22}(180^\circ)}{F_{11}(180^\circ)}. \quad (2.25)$$

Polarization lidars measure the ratio between the y -component and the x -component of the backscatter power, given that the emitted laser light is linearly polarized in the x -direction. This ratio is known as the linear depolarization ratio δ_1 (Freudenthaler et al., 2009). The depolarization parameter d is an atmospheric parameter, which is linear in the quantity of interest, whereas δ_1 is a lidar-specific parameter (Gimmestad, 2008). There is a unique relation between d and δ_1 :

$$\delta_1 = \frac{d}{2 - d}. \quad (2.26)$$

In case of spherical particles, d and δ_1 are equal to zero (as a result of Eq. 2.17).

2.3. Modeling optical properties of single particles

The extinction efficiency q_{ext} , the scattering efficiency q_{sca} , and the scattering matrix $\mathbf{F}(\theta)$ of a randomly-oriented aerosol particle at wavelength λ depend on the shape and the refractive index m of the particle, and on the ratio between particle size and wavelength λ . This ratio is beneficial for optical modeling because it combines two parameters (particle size and wavelength λ) of the modeling problem into a single parameter. The ratio between size and wavelength is described by the size parameter

$$x = \frac{2\pi r}{\lambda}. \quad (2.27)$$

This means, for example, that if particle size and wavelength λ are doubled (keeping x constant), but shape and m of the particle are unchanged, also the efficiencies q_{ext} , q_{sca} , and $\mathbf{F}(\theta)$ are unchanged; only the cross sections, e.g., C_{geo} , C_{ext} , C_{sca} , are four times larger. As $r = r_c$ is used as default in this thesis, the size parameter x is also given in terms of cross-section equivalence, unless otherwise stated.

The physics of the light-particle interaction are described by Maxwell's equations. For some classes of particles, solutions for Maxwell's equations are known and codes are available to perform numerical computations. For other particles, approximate approaches are required. Nousiainen (2009) published a review of numerical approaches for optical modeling. This section provides an overview of the most relevant methods for aerosols, including the well-known Mie theory, which is applicable to homogeneous spherical particles, the T-matrix method (TMM), which is efficient for rotationally-symmetric particles, the geometric optics method (GOM), which is an approximation for large particles, and the discrete dipole approximation (DDA), which is applicable to arbitrarily-shaped particles with not-too-large size parameters x .

2.3.1. Mie theory

The Mie theory provides a solution of Maxwell's equations for scattering and absorption of light by spherical particles (Mie, 1908). The solution is valid for any size parameter x and refractive index m . Mie (1908) expands the incident plane wave as well as the scattered wave into spherical vector wave functions. The internal field is expanded into regular spherical vector wave functions. By enforcing the boundary conditions on the particle surface, expansion coefficients of the scattered field are calculated. Using these expansion coefficients, all optical properties of the particle can be calculated. For a detailed review of the Mie theory, see, e.g., Liou (2002).

The Mie code from Mishchenko et al. (2002) is used for optical modeling of spherical particles in this study.

2.3.2. T-matrix method (TMM)

The T-matrix method (TMM) provides a solution of Maxwell's equations for the interaction of light with arbitrarily-shaped particles. In principle, solutions are possible for any shape, refractive index m , and size parameter x . The TMM was introduced by Waterman (1971), and proved to be an efficient method for rotationally-symmetric particles. Like in the Mie theory, the incident and the scattered field are expanded into certain spherical vector wave functions. The transition matrix (*T-matrix*) relates the coefficients of the incident field to the coefficients of the scattered field. Thus, if the T-matrix is known, all optical properties can be calculated, including those for random particle orientation. The calculation of the T-matrix of a particle is based on the extended boundary condition method. According to this method, the T-matrix is the product of two matrices, which are calculated by integrals over the particle surface. One of these matrices has to be inverted; this matrix inversion is numerically unstable for particles with high asphericity, large m , or large x . Thus the spectrum of applicable particles is limited. For more details about the TMM see, e.g., Mishchenko and Travis (1998) or Waterman (1971).

In this study, the TMM is used as the default method for modeling the optical properties of spheroids because the TMM is a numerically exact method. For these calculations, the state-of-the-art T-matrix code from Mishchenko and Travis (1998) is used (for technical details see Appendix B). Because of the limited range of applicable particles, in particular large size parameters x can not be modeled by the TMM, the geometric optics method (GOM) is used as a supplementary method for large x to cover the complete aerosol-relevant range of x .

2.3.3. Geometric optics method (GOM)

The geometric optics method (GOM) is applicable, if the particle and its structures are large compared to the wavelength (Liou, 2002). The GOM assumes that the particle surface is flat in spatial dimensions comparable to the wavelength. The incident light is divided into a large number of independent parallel waves ("rays"), evenly distributed on the cross

section of the particle (in fixed orientation). With these assumptions, the law of refraction and Fresnel equations can be employed to trace the path of the rays. Absorption of wave energy inside the particle is considered. The scattered rays are collected in small angular bins and are supplemented by diffracted rays, which are calculated following Fraunhofer diffraction on a circular aperture with the same cross section as the particle. The ray tracing and diffraction calculations are repeated for many different particle orientations to get the orientation-averaged properties. As a result of this procedure, the extinction cross section C_{ext} is fixed to twice the geometric cross section C_{geo} , i.e. $q_{\text{ext}} = 2$ for GOM simulations. Interference effects are not considered by the ray tracing. At very small and very large scattering angles (θ near 0° and 180°) the solid angle covered by the angle bins are very small. This means, in particular for the angle bin in the backward direction, that only very few rays are collected. Hereafter the described approach is denoted as the conventional geometric optics method (CGOM) because extensions to this approach are available. An implementation of CGOM was developed by Macke et al. (1995).

Extensions of CGOM were, for example, developed by Yang and Liou (1996); Yang et al. (2007); their improved geometric optics method (IGOM) is based on the electromagnetic equivalence theorem (Schelkunoff, 1936). This theorem states that the far-field of a particle can be computed if the field on the particle surface is known. The field on the surface is calculated using conventional ray-tracing techniques. For the calculation of the extinction efficiency q_{ext} the so-called edge effect (van de Hulst, 1981) is considered by IGOM, as well as the above- and below-edge effect for the absorption efficiency q_{abs} .

In this study, the geometric optics method (GOM) is used as a supplementary method for spheroids for which the TMM is not applicable, that is for large size parameters. Figure 2.4 illustrates the range of particle sizes and wavelengths for which the T-matrix method is applicable. Within the green area ($x < 25$), the T-matrix method is applicable to all spheroids with aspect ratios $\epsilon' \leq 3.0$, whereas in the orange area, the upper limit of the applicable ϵ' is smaller than 3.0, and in the red area ($x > 118$), the TMM is not applicable for any ϵ' . Thus, GOM calculations are required for large ϵ' in the orange area, and for all ϵ' in the red area.

The parameters of the CGOM and IGOM code that are used in this study are given in Appendix B. Due to its assumptions and simplifications, GOM needs to be validated against exact methods, for example, the TMM. The accuracy of GOM for particles that can not be modeled by TMM is of interest because GOM is used as a supplementary method for the TMM. Comparisons between GOM and the exact TMM, however, are only possible for particles on which both methods can be applied (the 'overlap region'). Comparisons in the overlap region indicate the accuracy of GOM for the particles of interest. Figure 2.5 provides such a comparison. This figure compares optical properties of single particles over size parameter x calculated using the exact TMM and both available GOM implementations (using the code parameters given in Appendix B) for two different prolate shapes ($\epsilon' = 1.6$ and 2.4) and a refractive index $m = 1.52 + 0.0043i$. Properties which are relevant for lidar remote sensing and the forward scattering observed by Sun photometers are shown. Results from the TMM are plotted in black, results from CGOM (Macke et al., 1995) in red, and results from IGOM (Yang et al., 2007) in green. Figure 2.5 illustrates

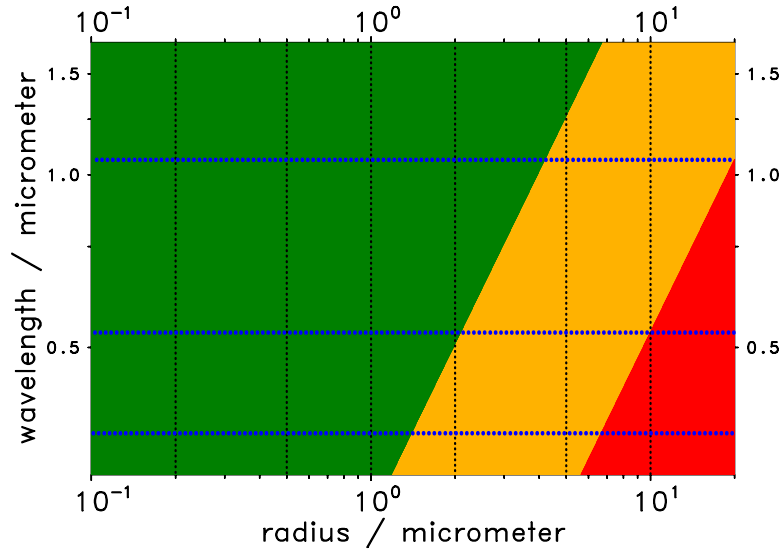


Figure 2.4.: Application of T-matrix method (TMM) and geometric optics method (GOM) for aspect ratios $\epsilon' \leq 3$ depending on particle radius and wavelength; green: TMM for all particles; orange: TMM for small ϵ' and GOM for large ϵ' ; red: GOM for all particles; blue dotted lines: wavelengths of Nd:YAG laser (original: 1064 nm, frequency-doubled: 532 nm, frequency-tripled: 355 nm).

that the extinction efficiency from CGOM is $q_{\text{ext}} = 2$, whereas the IGOM method overestimates the amplitude of the oscillations of $q_{\text{ext}}(x)$; the average $q_{\text{ext}}(x)$ from IGOM, however, is in good agreement with the exact $q_{\text{ext}}(x)$ from TMM. In the second row of Fig. 2.5, the inverse of the lidar ratio $1/S(x)$, which is the ratio between backscattering and extinction, is shown. This comparison shows that the ratios from CGOM better agree with exact TMM results than the ratios from IGOM. The depolarization parameter $d(x)$ from both GOM implementations does not converge to the $d(x)$ from TMM. Due to the comparatively weak backscattering by large particles (see second row of Fig. 2.5), the underestimation of $d(x)$ from GOM only slightly reduces the depolarization parameter d of typical aerosol ensembles (Sect. 2.4). In the forward direction ($q_{\text{diffsca}}(4^\circ)/q_{\text{ext}}$, lower row of Fig. 2.5) the agreement of CGOM and IGOM results with exact results is good.

The comparisons of GOM with exact TMM results suggest slightly better accuracy of CGOM in the backscattering direction, as compared to IGOM, whereas the extinction efficiency from IGOM is more accurate than the same quantity from CGOM.

2.3.4. Discrete dipole approximation (DDA)

The DDA was initially proposed by Purcell and Pennypacker (1973). They model the optical properties of particles using an array of polarizable elements, located on a cubic lattice.

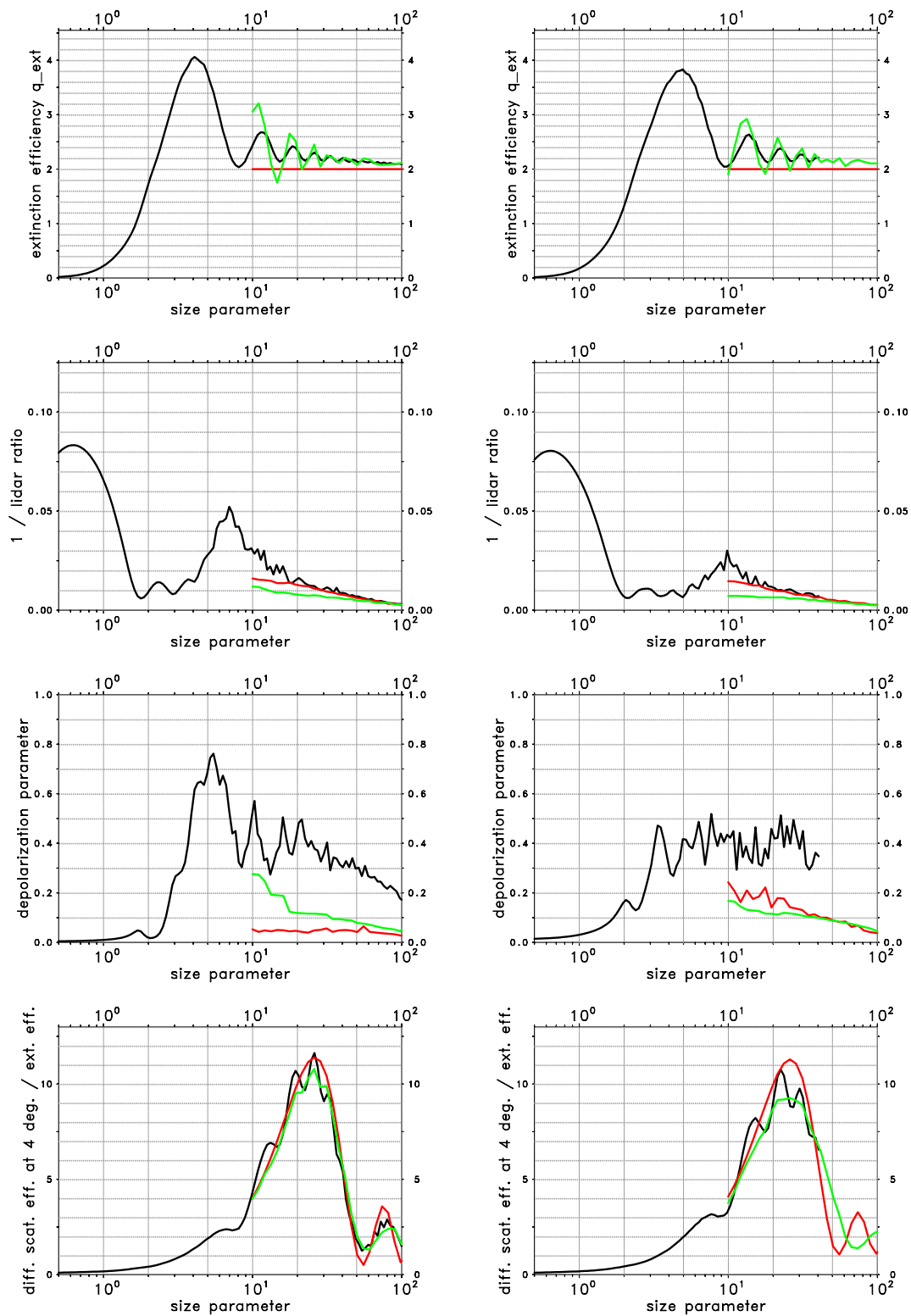


Figure 2.5.: Optical properties from different methods over size parameter x ; $m = 1.52 + 0.0043i$; left: prolate spheroids with $\epsilon' = 1.6$, right: prolate spheroids with $\epsilon' = 2.4$; black: TMM, red: CGOM, green: IGOM.

The spatial distributions and the polarizabilities of the elements are selected to represent the microphysical properties of the particle of interest. The oscillation of each element, which is due to the incident field and the fields from all other elements, is calculated in an iterative procedure until convergence is reached. Finally, the optical properties of the particle in the far-field can be calculated from the oscillations of all elements. A comprehensive overview of different aspects of DDA was recently given by Yurkin and Hoekstra (2007).

In this study, the Amsterdam DDA code (ADDA v.0.78.2, Yurkin and Hoekstra, 2011) is used for the calculation of the optical properties of irregularly-shaped particles (Fig. 2.2). The huge computational demand of DDA calculations for large size parameters x makes it necessary to find optimal code parameters that allow fast and accurate calculations. ADDA allows the following parameters to be adjusted in this sense:

- DDA formulation
- Stopping criterion of the iterative solver
- Number of dipoles per wavelength

Furthermore, an orientation averaging scheme needs to be applied because each DDA calculation considers only a single particle orientation. Inaccuracies of the calculated orientation-averaged optical properties may originate directly from inaccuracies of the ADDA calculations or from the orientation averaging scheme. Since applicable exact methods for the optical modeling of irregularly-shaped particles are not available, the accuracy of the ADDA calculations for such particles needs to be estimated by comparing results to results modeled using more strict calculation parameters.

Accuracy tests are performed for shapes B and C (Fig. 2.2), for 4 size parameters from 10 to 17.3, and for refractive index $m = 1.52 + 0.0043i$, i.e. 8 cases are considered in total. By comparing the different DDA formulations available in ADDA, it was found that the filtered coupled-dipole technique (ADDA command line parameter `"-pol fcd -int fcd"`), as introduced by Piller and Martin (1998) and applied by Yurkin et al. (2010), offers the best compromise between computation speed and accuracy of modeled optical properties. Using a stopping criterion for the iterative solver of 10^{-4} instead of 10^{-3} , has only negligible influence on orientation-averaged optical properties ($< 0.1\%$) but requires approximately 30% more computation time; thus, 10^{-3} is used for the ADDA calculations in this study. The extinction efficiency q_{ext} is found to change by less than 0.3% (relative) if a grid density of 16 dipoles per wavelength is used instead of 11; maximum relative changes of the lidar ratio S , the linear depolarization ratio δ_1 , and the phase function at 3° are 1.7%, 2.3%, and 0.2% respectively; the computation time however is higher by a factor of about 3 to 4. 11 dipoles per wavelength are used in this study because it provides good accuracy while keeping reasonable computation time. As an additional accuracy test of these selected ADDA settings, the reciprocity of light scattering (van de Hulst, 1981) is investigated: The modeled scattering at $\theta = 90^\circ$ in a single azimuth direction for a single particle orientation is compared with the modeled scattering for the reversed path of light. The relative difference between both model setups is smaller than 1.3% for all 8 cases.

ADDA calculations for a large number of orientations are required to get orientation-averaged properties. ADDA provides an optional orientation averaging scheme. Penttilä et al. (2007) showed that this orientation averaging scheme is not optimal in terms of accuracy. Furthermore, in case of large size parameters x , the utilization of the built-in orientation averaging scheme would result in extremely long computation times for a single ADDA run up to several months. For the calculations in this study, a different approach for orientation averaging was selected. The orientation averaging of the optical properties is done by rotating the particle over the three Euler angles (α_e , β_e , γ_e). Definition of the Euler angles is adapted from Yurkin and Hoekstra (2011). The averaging over α_e is done within a single ADDA computation because rotation over α_e is equivalent to the rotation of the scattering plane. The optical properties are averaged over 32 α_e . For averaging over β_e and γ_e individual ADDA computations are necessary. For particles with size parameters $x < 15$ ($x > 15$) averaging over β_e is done with a step width of 9° (15°), and for each β_e up to 40 (24) γ_e are used for averaging. In summary, for a single particle 526 (206) individual ADDA computations are performed and, if the averaging over α_e is considered, 16832 (6592) orientations are evaluated.

To test the accuracy of the selected orientation averaging scheme, for comparison, optical properties using a smaller step width of 5° for β_e and γ_e in the orientation averaging scheme are calculated; these calculations require about 5 to 12 times more computation time than the calculations with the selected orientation averaging scheme. Maximum deviations of 0.5% for the extinction efficiency q_{ext} are found. The relative changes of the lidar ratio S and the linear depolarization ratio δ_1 are smaller than 5% for size parameters $x < 15$, and for $x = 17.3$ the relative changes are smaller than 8%. The maximum deviation for the phase function at 3° is 0.3%.

In addition, Appendix C compares orientation-averaged ADDA results for spheroids, using the selected orientation averaging scheme, with numerically-exact results from the T-matrix method. This comparison reveals larger deviations than found for the irregularly-shaped particles; the larger deviations can be explained by the symmetry of the spheroids, which results in fewer independent ADDA simulations during orientation averaging and diminishing statistics of the averaging.

In summary, these accuracy tests demonstrate that the accuracy of modeling single particle properties of irregularly-shaped particles is on an acceptable level and that orientation averaging introduces larger errors than the calculations of the ADDA code itself. ADDA with the filtered coupled-dipole technique, 11 dipoles per wavelength, and a stopping criterion for the iterative solver of 10^{-3} is used for optical modeling in this study together with the above-described orientation averaging scheme.

2.4. Optical properties of particle ensembles

Aerosol particles typically occur as ensembles of particles with different sizes. In desert dust and volcanic ash aerosols different chemical compositions or refractive indices and shapes are mixed, in addition. The chemical composition can vary within a single particle

(‘internal mixing’) or from particle to particle (‘external mixing’). Homogeneous particles are assumed in this thesis, thus only external mixtures are modeled in the subsequent chapters; internal mixtures are implicitly considered by using effective refractive indices of each particle. To account for the natural variability of particle shapes, mixtures of different model shapes are necessary for realistic optical modeling of mineral dust and volcanic ash aerosols (Mishchenko et al., 1997). The variability of particle sizes in natural aerosols is parameterized by log-normal size distributions. A log-normal distribution is given by

$$n(r) = \frac{dN}{dr} = \frac{N_0}{\sqrt{2\pi} \ln \sigma r} \exp \left[- \left(\frac{\ln r - \ln r_0}{\sqrt{2} \ln \sigma} \right)^2 \right]. \quad (2.28)$$

$n(r) = dN/dr$ is the particle number density per radius interval (unit: $m^{-3}m^{-1}$). Its parameters are the number density of particles N_0 (unit: m^{-3}), the modal radius r_0 , and the width σ of the mode. Mono-modal log-normal size distributions may not be sufficient to describe any atmospheric size distribution adequately; for example, the removal of particles larger than a certain size by sedimentation may require using a maximum particle radius r_{\max} for the parameterization. Alternatively, most size distributions can be well approximated by multi-modal distributions; such size distributions are sums of several log-normal size distributions.

A single bulk parameter of the size distribution relevant for the optical properties is the effective radius r_{eff} . In case of spherical particles, it is

$$r_{\text{eff}} = \frac{\int r^3 n(r) dr}{\int r^2 n(r) dr}. \quad (2.29)$$

For a mono-modal log-normal size distribution, r_{eff} is equal to $r_0 \cdot e^{2.5(\ln \sigma)^2}$. r_{eff} is the cross-section-weighted mean radius of the particles. For particles larger than λ , the extinction efficiency q_{ext} is nearly independent of size and r_{eff} is almost equal to the mean radius for extinction (Hansen and Travis, 1974). In case of non-spherical particles, different definitions of r_{eff} are available; an overview was given by McFarquhar and Heymsfield (1998). r_c is used in this thesis for specifying the size of non-spherical particles; upon this, the r_{eff} of ensembles of non-spherical particles is defined here as

$$r_{\text{eff}} = \frac{\int r_c^3 n(r_c) dr_c}{\int r_c^2 n(r_c) dr_c}. \quad (2.30)$$

This definition of r_{eff} is chosen because, in case of particles larger than the wavelength, the particle cross section is relevant for the extinction ($q_{\text{ext}} \approx 2$) and this r_{eff} is retrievable from aureole observations (see next chapters). This r_{eff} is almost equal to the mean cross-section-equivalent radius for extinction and to r_{eMH} of McFarquhar and Heymsfield (1998). $r_{\text{eff}}^* = \overline{\xi_{\text{vc}}^3} r_{\text{eff}}$ is equal to an alternative definition $3V^*/4A^*$ for the effective radius, where V^* is the volume density and A^* the projected area density; r_{eff}^* is equal to r_{eF} of McFarquhar and Heymsfield (1998). The cube of the shape-dependent radius conversion factor $\overline{\xi_{\text{vc}}^3}$ (Eq. 2.3) is averaged over all particle shapes in the ensemble, assuming that particle shape

is size-independent. r_{eff}^* is, for example, relevant for the ratio of absorption and extinction by large weakly-absorbing particles.

The mass concentration M , that is the mass of aerosol particles per volume in the atmosphere, is calculated by

$$M = \frac{4\pi}{3} \rho \overline{\xi_{\text{vc}}^3} \int r^3 n(r) dr. \quad (2.31)$$

ρ is the mass density of the aerosol particles and, as mentioned, $r = r_c$. M is typically in the order of $\mu\text{g m}^{-3}$.

2.4.1. Extinction, scattering, absorption

The extinction coefficient α_{ext} is a measure for the extinction per unit length of incident light by particles. For known size distribution it can be calculated from the single particle extinction cross sections C_{ext} :

$$\alpha_{\text{ext}} = \int_{r_{\text{min}}}^{r_{\text{max}}} C_{\text{ext}}(r) \cdot n(r) \cdot dr. \quad (2.32)$$

The range from r_{min} to r_{max} (integration limits omitted hereafter) should cover all particle sizes that contribute to extinction. $C_{\text{ext}}(r)$ also depends on particle shape and refractive index m (and on λ). For the calculation of properties of ensembles consisting of particles with different refractive indices m and different shapes, the particles are separated in different types. Each type is characterized by a single fixed refractive index m and a single fixed particle shape. It is assumed that the relative abundance ν_j of each particle type j is independent of r . The relative abundance ν_j of type j is the product of the relative abundance of its shape and the relative abundance of its refractive index m . If J is the number of different particle types, the sum $\sum_J \nu_j$ over all types is equal to 1. The extinction coefficient α_{ext} of such ensembles is calculated as

$$\alpha_{\text{ext}} = \sum_{j=1}^J \left(\nu_j \cdot \int C_{\text{ext},j}(r) \cdot n(r) \cdot dr \right). \quad (2.33)$$

$C_{\text{ext},j}(r)$ is the extinction cross section of particle type j at radius r .

The scattering coefficient α_{sca} and the absorption coefficient α_{abs} are defined analogously to α_{ext} (Eqs. 2.32 and 2.33). Using α_{sca} , the single scattering albedo of an ensemble is calculated as

$$\omega_0 = \frac{\alpha_{\text{sca}}}{\alpha_{\text{ext}}}. \quad (2.34)$$

By integrating the aerosol extinction coefficient α_{ext} in a layer from height z_{min} to z_{max} , the aerosol optical depth τ of this layer is calculated:

$$\tau = \int_{z_{\text{min}}}^{z_{\text{max}}} \alpha_{\text{ext}}(z) \cdot dz. \quad (2.35)$$

If z_{\min} and z_{\max} are not mentioned, τ typically refers to the total aerosol column of the atmosphere (z_{\min} is ground level, z_{\max} is about 10 km to 40 km).

The Ångström exponent κ_{ext} characterizes the spectral variability of the extinction in the wavelength range from λ_1 to λ_2 . For an aerosol ensemble it is defined as

$$\kappa_{\text{ext}} = \frac{\ln \alpha_{\text{ext}}(\lambda_1) - \ln \alpha_{\text{ext}}(\lambda_2)}{\ln \lambda_2 - \ln \lambda_1} \quad (2.36)$$

whereas it is

$$\kappa_{\text{ext}}^* = \frac{\ln \tau(\lambda_1) - \ln \tau(\lambda_2)}{\ln \lambda_2 - \ln \lambda_1} \quad (2.37)$$

for an aerosol layer or the total aerosol column. The spectral variability of the extinction indicates the size of aerosol particles. κ_{ext} is close to zero for particles larger than the wavelengths, and increases if particles become smaller than the wavelengths. κ_{ext} is typically in the range from 0 to 2.5 for aerosols (Dubovik et al., 2002), whereas for air molecules, which are very small compared to solar wavelengths, κ_{ext} is about 4 (Rayleigh limit).

For the conversion of extinction coefficients to mass concentrations the mass-extinction conversion factor η is used:

$$\eta = \frac{M}{\alpha}. \quad (2.38)$$

The unit of η is gm^{-2} ; it is the inverse of the mass extinction coefficient. Using the cross-section-weighted mean extinction efficiency $\overline{q_{\text{ext}}}$, defined by

$$\overline{q_{\text{ext}}} = \frac{\int q_{\text{ext}}(r) \cdot r^2 \cdot n(r) \cdot dr}{\int r^2 \cdot n(r) \cdot dr}, \quad (2.39)$$

a relation between η and r_{eff} is derived:

$$\eta = \frac{4}{3} \frac{\rho \cdot \overline{\xi_{\text{vc}}^3}}{\overline{q_{\text{ext}}}} r_{\text{eff}}. \quad (2.40)$$

2.4.2. Angular-dependent scattering

The amount of light scattered per unit length by an aerosol ensemble to scattering angle θ , neglecting multiple scattering effects, is proportional to the differential scattering coefficient

$$\begin{aligned} \alpha_{\text{diffsca}}(\theta) &= \int C_{\text{diffsca}}(r, \theta) \cdot n(r) \cdot dr \\ &= \int C_{\text{ext}}(r) \cdot \frac{q_{\text{diffsca}}(r, \theta)}{q_{\text{ext}}(r)} \cdot n(r) \cdot dr. \end{aligned} \quad (2.41)$$

α_{diffsca} is analogous to α_{ext} (Eq. 2.32). Consequently, for aerosol ensembles consisting of different particle types (characterized by refractive index and shape), the weighted α_{diffsca} of each type has to be added analogously to Eq. 2.33.

2.4.3. Backscattering

Analogously to the extinction coefficient α_{ext} (Eq. 2.32), the backscatter coefficient β is calculated by

$$\beta = \alpha_{\text{diffsca}}(180^\circ) = \int C_{\text{ext}}(r) \cdot \frac{\omega_0(r) \cdot F_{11}(r, 180^\circ)}{4\pi} \cdot n(r) \cdot dr. \quad (2.42)$$

By using the lidar ratio of single particles, the backscatter coefficient can be expressed by

$$\beta = \int C_{\text{ext}}(r) \cdot \frac{1}{S(r)} \cdot n(r) \cdot dr. \quad (2.43)$$

The lidar ratio S of an aerosol ensemble, which describes the ratio between extinction and backscattering, is calculated from α_{ext} and β by

$$S = \frac{\alpha_{\text{ext}}}{\beta}. \quad (2.44)$$

Analogously to κ_{ext} (Eq. 2.36), the Ångström exponent for backscatter κ_{bsc} characterizes the spectral variability of the backscatter coefficient β in the wavelength range from λ_1 to λ_2

$$\kappa_{\text{bsc}} = \frac{\ln \beta(\lambda_1) - \ln \beta(\lambda_2)}{\ln \lambda_2 - \ln \lambda_1}. \quad (2.45)$$

The depolarization parameter d of an aerosol ensemble is calculated by

$$d = \frac{\int C_{\text{ext}}(r) \cdot \frac{1}{S(r)} \cdot d_s(r) \cdot n(r) \cdot dr}{\int C_{\text{ext}}(r) \cdot \frac{1}{S(r)} \cdot n(r) \cdot dr}. \quad (2.46)$$

d of the ensemble is the backscatter-weighted average depolarization parameter $d_s(r)$ of the particles in the ensemble ($d_s(r)$ is used instead of $d(r)$ in Eq. 2.46 to avoid confusion with d of the ensemble). In case of mixtures of particles of different refractive indices m and different shapes, the calculation of β and d (Eqs. 2.43, 2.46) is analogous to Eq. 2.33.

2.5. Radiative transfer modeling

In the previous sections, methods for modeling of single scattering properties were introduced. But for many remote sensing techniques, multiple scattering effects are relevant, e.g., for sky radiances measured by Sun photometers which are considered in this study (see below). This requires solving the radiative transfer equation

$$\frac{dL}{ds} = -\alpha_{\text{ext}}L + \frac{\alpha_{\text{ext}}\omega_0}{4\pi} \int_{4\pi} p(\Omega', \Omega)L(\Omega')d\Omega', \quad (2.47)$$

where L is the monochromatic radiance (unit: power per area and solid angle), Ω the direction of L , $p(\Omega', \Omega)$ the probability that a photon is scattered from direction Ω' to Ω ,

and $L(\Omega')$ the radiance from direction Ω' ; $p(\Omega', \Omega)$ is equal to the phase function $F_{11}(\theta)$ (Eq. 2.15) if θ is the angle between Ω and Ω' . Equation 2.47 shows that the radiance L is attenuated by extinction and enhanced by light that is scattered from other directions to the direction of L . Thermal emission, which is not relevant at solar wavelengths, is neglected here. It is assumed that atmospheric particles are sufficiently far from each other so that each scattering event occurs independently from other particles (van de Hulst, 1981). Two frequently-used methods for solving Eq. 2.47 are the Discrete Ordinates Radiative Transfer method (DISORT, Stamnes et al., 1988) and the Monte Carlo method (Marchuk, 1980; Mayer, 2009).

DISORT is an efficient method for plane-parallel model atmospheres. It allows one to calculate radiances for a number of so-called streams, for which scattering phase functions have to be provided in terms of Legendre coefficients. If large particles are present in the atmosphere, a large number of streams is needed due to strongly-peaked phase functions, making the original DISORT inefficient for accurate modeling of such atmospheres. By application of intensity correction methods (Nakajima and Tanaka, 1988; Buras et al., 2011), the accuracy of DISORT calculations for large particles is significantly increased without needing to calculate a large number of streams.

Monte Carlo methods rely on repeated random sampling of models. To simulate the radiative transfer, the paths of a large number of photons are traced through the model atmosphere. This approach allows one to calculate the radiative transfer for nearly arbitrarily-complex atmospheric scenarios. The Monte Carlo method, in general, is slower than DISORT, though variance-reduction methods can improve the computational speed of the Monte Carlo method such that it is comparable to DISORT for some applications (Buras and Mayer, 2011).

2.6. Remote sensing techniques

This study covers ground-based remote sensing of aerosols. The most widely-used techniques for this task are the lidar technique and Sun photometry; they are introduced in this section.

2.6.1. Lidar

A lidar (Light Detection and Ranging) is an active remote sensing instrument which measures range-resolved parameters of the atmosphere. Figure 2.6 illustrates the basic principle of lidar remote sensing: A laser emits very short linearly-polarized laser pulses (typically in the order of several nanoseconds), a telescope collects the backscattered laser light, and electronics is used to sample the collected light in high temporal resolution (typically 10 to 20 MHz). From the travel time of the light t and the speed of light c_0 , the distance R to the location of scattering is calculated ($R = c_0 \cdot t/2$).

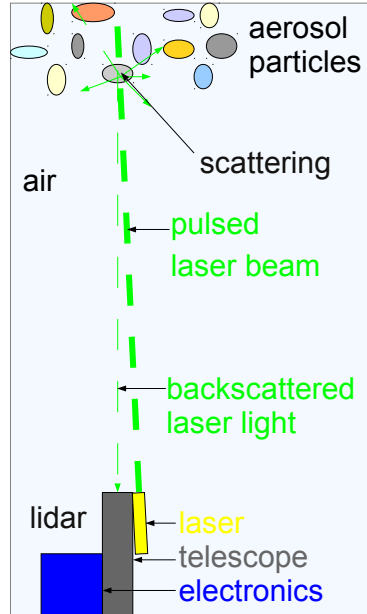


Figure 2.6.: Basic principle of lidar remote sensing of aerosols.

2.6.1.1. Elastic backscatter lidar

The simplest type of lidar is an elastic backscatter lidar. The wavelengths of the laser and the detector are the same. The lidar signal $P(R)$ is described by the lidar equation (Wandinger, 2005)

$$P(R) = K \cdot O(R) \cdot R^{-2} \cdot (\beta(R) + \beta_m(R)) \cdot T(R), \quad (2.48)$$

where R is the distance to the scattering object, K the system constant, $O(R)$ the overlap function, $\beta(R)$ and $\beta_m(R)$ the backscatter coefficients of particles and molecules, and $T(R)$ the transmission term. $T(R)$ is calculated from the extinction profiles of particles and molecules by

$$T(R) = \exp \left(-2 \cdot \int_0^R (\alpha_{\text{ext}}(r) + \alpha_{\text{ext},m}(r)) dr \right). \quad (2.49)$$

The overlap function $O(R)$ determines which fraction of the laser beam is within the field-of-view of the telescope. Typically, lidar signals are used only for R where $O(R) = 1$ (full overlap). The extinction coefficient $\alpha_{\text{ext}}(R)$ is the quantity of interest for meteorological applications. A backward integration scheme, as proposed by Fernald (1984), can be applied to the lidar profile $P(R)$ to get the height-resolved aerosol extinction coefficient $\alpha_{\text{ext}}(R)$ and backscatter coefficient $\beta(R)$. For this, some additional information is needed:

meteorological data (e.g., from radiosondes) for the calculation of $\beta_m(R)$ and $\alpha_{\text{ext},m}(R)$, an atmospheric layer with known $\beta(R)$, as for example an aerosol-free layer, and the lidar ratio of the particles $S(R) = \alpha_{\text{ext}}(R)/\beta(R)$. The lidar ratio S of the aerosol particles is critical because S varies approximately from 10 sr to 100 sr, depending on the aerosol type.

Additional information about aerosol particles can be obtained by measuring the polarization state of the backscattered light. For example, measurements of the linear depolarization ratio δ_1 provide information about the sphericity of the particles.

2.6.1.2. Raman lidar and High Spectral Resolution Lidar

Advanced lidar techniques were developed, which observe additional parameters that allow one to derive aerosol extinction coefficients α_{ext} without the need to assume a lidar ratio S . Raman lidars and High Spectral Resolution Lidars provide such parameters.

Like a simple backscatter lidar, a Raman lidar measures the signal at the laser wavelength; but, in addition, it detects photons that were backscattered by air molecules at other wavelengths due to Raman effects (Ansmann et al., 1992). Usually, Raman scattering of nitrogen (N_2) or oxygen (O_2) is detected by Raman lidars because their mixing ratio in the air is well-known. Only the vertically-resolved air density is needed as an additional parameter for the derivation of the α_{ext} -profile from Raman measurements. The air density can be derived from radiosonde data or from standard atmospheres. A drawback of the Raman lidar is that the backscattered intensity at the Raman-shifted wavelength is approximately three orders of magnitude lower than at the emitted wavelength. Thus, long measurement times are necessary to retrieve accurate atmospheric profiles; moreover, Raman measurements are typically only possible at night.

Another type of lidar that allow one to derive α_{ext} without the assumption of a lidar ratio S is the "High Spectral Resolution Lidar" (HSRL, Eloranta (2005)). The principle of a HSRL is that it measures the signal from the aerosol particles and the signal from the molecules separately. These signals can be separated because the signal from aerosol particles has a very small spectral width compared to the signal from air molecules. This difference of spectral widths is a result of Doppler effects and differences of the thermal velocities of molecules and aerosol particles: the thermal motion of small air molecules is much faster than the motion of comparatively large aerosol particles. Optical filters or absorption cells with very small bandwidths are used to separate the aerosol signal from the molecular signal. Since both signals are comparatively high, HSRLs can be operated also at daytime.

2.6.1.3. Instrumentation and observed properties

Two lidar systems are available at the Meteorological Institute of the Ludwig-Maximilians-Universität (LMU) in Munich: MULIS (multi-wavelength lidar system, e.g., Freudenthaler et al., 2009) and POLIS (portable lidar system, e.g., Groß et al., 2008). MULIS is a Raman- and depolarization-lidar including channels for elastic backscattering at 355 nm, 532 nm, and 1064 nm, and corresponding Raman channels for the determination of the extinction

coefficient at 355 nm and 532 nm. The linear depolarization ratio of particles is derived at 532 nm. POLIS is a small low-power two-channel lidar for Raman or depolarization measurements at 355 nm. As a consequence, combining the measurements from both lidars provides depolarization ratios at two wavelengths. The optical design of both lidars is optimized for measurements in the troposphere; the full overlap ($O(R) = 1$) of MULIS is reached in about 200 m to 400 m depending on field stop adjustments, and full overlap is reached in approximately 70 m for POLIS (Groß et al., 2008). Vertical profiles of the extinction coefficient α_{ext} and backscatter coefficient β of the aerosol particles at $\lambda = 355$ nm and 532 nm are derived using the Raman approach (Ansmann et al., 1992). Vertical profiles of the other optical parameters, i.e. the linear depolarization ratio δ_1 at $\lambda = 355$ nm and 532 nm, and β at $\lambda = 1064$ nm, are derived using the approaches described by Freudenthaler et al. (2009) and Fernald (1984), respectively.

In addition to MULIS and POLIS observations, observations of desert dust aerosols from two other lidar systems have been used for this work: The BERTHA lidar system of the Leibniz Institute for Tropospheric Research in Leipzig is also a Raman- and depolarization-lidar which provides, among other particle properties, the linear depolarization ratio δ_1 at $\lambda = 710$ nm (Tesche et al., 2009; Tesche et al., 2011). The high spectral resolution lidar (HSRL) of the German Aerospace Center, operated onboard the Falcon aircraft provides the lidar ratio S and the linear depolarization ratio δ_1 at 532 nm, as well as δ_1 at 1064 nm (Esselborn et al., 2009).

2.6.2. Sun photometer

Sun photometers observe the direct irradiance from the Sun and often, in addition, sky radiances from several directions on the sky.

2.6.2.1. Direct Sun observations

Figure 2.7 illustrates direct Sun photometry. The direct irradiance I from the Sun is measured using an optical system with a small field-of-view in the direction of the Sun. The field-of-view is larger than the solar disk, but because of the comparatively weak diffuse radiance, the Sun photometer measures primarily the direct irradiance from the Sun. To measure the irradiance at different wavelengths, filters with small bandwidths are attached to the front of the radiation sensors of the photometer. The measured irradiances at the filter wavelengths λ are, according to Beer-Lambert law,

$$I(\lambda) = I_0(\lambda) \cdot e^{-\tau_{\text{atm}}(\lambda) \cdot m_{\text{rel}}}, \quad (2.50)$$

where I_0 is the extraterrestrial irradiance, τ_{atm} the total optical depth of the atmosphere, and m_{rel} the relative airmass. In a plane-parallel atmosphere, m_{rel} is equal to $1/\cos z_s$ for Sun zenith angle z_s . In the atmosphere of the Earth, which is of nearly spherical geometry, this relation is a good approximation for z_s smaller than about 50° to 70° , but increasingly overestimates m_{rel} for larger z_s . As τ_{atm} is the quantity of interest in Eq. 2.50, this equation

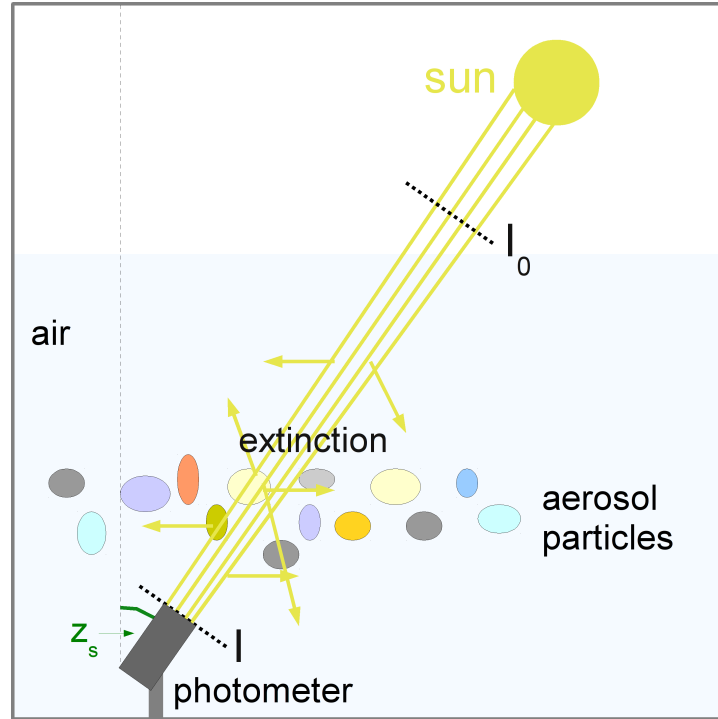


Figure 2.7.: Basic principle of Sun photometer remote sensing.

is rearranged to

$$\tau_{\text{atm}}(\lambda) = -\frac{1}{m_{\text{rel}}} \ln \left(\frac{I(\lambda)}{I_0(\lambda)} \right). \quad (2.51)$$

The extraterrestrial irradiance $I_0(\lambda)$ is not known a-priori, whereas $I(\lambda)$ is available from the photometer, and m_{rel} is calculated from the Sun zenith angle z_s . The extraterrestrial irradiance $I_0(\lambda)$ is determined using the Langley calibration technique (Schmid and Wehrli, 1995), as illustrated in Fig. 2.8. Measured $\ln(I(\lambda))$, from a time span after Sun rise or before Sun set, are plotted against relative airmass m_{rel} (blue crosses). If the optical depth $\tau_{\text{atm}}(\lambda)$ of the atmosphere is constant during this time span, the plotted $\ln(I(\lambda))$ lay on a straight line (green line), as a result of Eq. 2.50. The extraterrestrial intensity $I_0(\lambda)$ (red) is calculated by extending this line to $m_{\text{rel}} = 0$. Good conditions for the Langley calibration, that is stable τ_{atm} , are typically found above the boundary layer of the atmosphere in high-pressure systems. Thus for Langley calibration, Sun photometers are usually installed on mountains. The seasonal variability of the distance between Earth and Sun influences $I_0(\lambda)$, which needs to be considered for the calculation of $\tau_{\text{atm}}(\lambda)$, too. The optical depth

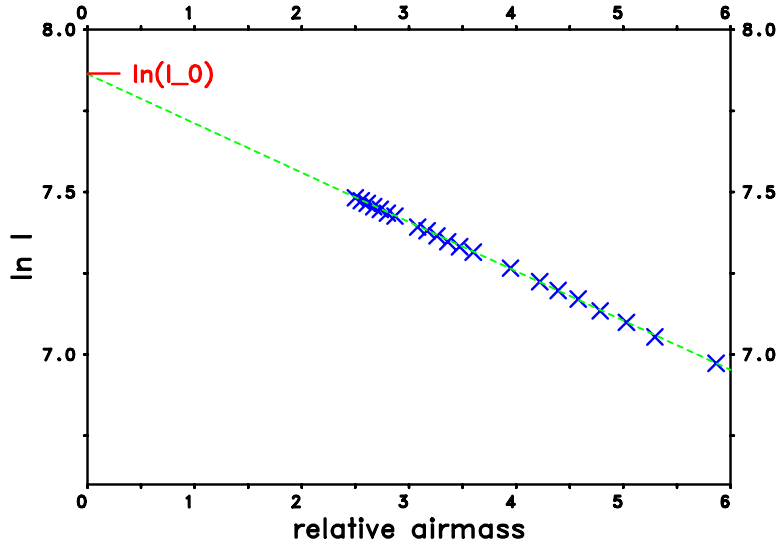


Figure 2.8.: Example for langley calibration of extraterrestrial irradiance I_0 (from SSARA photometer at Zugspitze on afternoon of 30 March 2009 at $\lambda = 500$ nm).

of the atmosphere τ_{atm} is the sum of the optical depths of its constituents:

$$\tau_{\text{atm}} = \tau_{\text{aer}} + \tau_{\text{rayleigh}} + \tau_{\text{O}_3} + \tau_{\text{H}_2\text{O}} + \tau_{\text{others}} \quad (2.52)$$

Thus, for calculating the optical depth of the aerosols τ_{aer} (equal to τ in Eq. 2.35 and elsewhere in this study) from the total optical depth τ_{atm} , the optical depths of all other atmospheric constituents have to be known. The accuracy of aerosol optical depths from Sun photometers is typically better than 0.01 to 0.03 (Holben et al., 1998; Toledano et al., 2011).

2.6.2.2. Sky radiance observations

Sun photometers typically are used, in addition to measurements of direct irradiances, for measuring sky radiances at several wavelengths and directions. Usual measurement scenarios are almucantar scans, where sky radiances are measured on a circle around the local zenith containing the Sun, and principle plane scans for radiances on a line through the local zenith and the Sun. The typical calibration accuracy for sky radiance measurements is in the order of 5%. Measurements up to 6° angular distance from the Sun are referred to as measurements in the aureole of the Sun.

2.6.2.3. Instrumentation and observed properties

The automatic CIMEL CE-318 Sun photometer is the standard photometer of the AErosol RObotic NETwork (AERONET), which is a global network of photometers for the characterization of aerosols (Holben et al., 1998). The photometer measures the direct solar

irradiances at several (5 to 10, depending on configuration) wavelengths from 340 nm to 1020 nm which allows one to determine the spectral optical depth of the atmospheric aerosol column. Diffuse sky radiation is observed in the almucantar and the principle plane at several wavelengths from 440 nm to 1020 nm. Modifications of the photometers exist which measure additional parameters. For example, the CIMEL of the Leibniz Institute for Tropospheric Research in Leipzig, in addition, observes direct and diffuse radiation at 1640 nm. The SSARA Sun photometer, developed and operated by the Meteorological Institute of the LMU Munich, observes direct irradiances at 12 wavelengths in the range from 340 nm to 1550 nm (Toledano et al., 2009).

3. Methods for retrieval of microphysical properties

In the previous chapter, techniques for optical modeling and remote sensing of aerosols were introduced. The present chapter describes methods, developed in this study, for the retrieval of microphysical properties of aerosol particles from the remote sensing observations. First, an overview of the Bayesian retrieval approach is given. Optical properties of single particles are required for retrievals; thus, subsequently, data sets of optical properties of aerosol particles of spheroidal and irregular shapes are established and presented. The sensitivity of observed particle properties to changes of microphysical particle properties determines the potential to retrieve microphysical properties from remote sensing observations; this topic is investigated in the third section of this chapter. In the final section, three retrieval types are developed and described. The different types are applicable depending on the availability of the observation techniques (lidar, photometer) and the observed aerosol type (ash, dust, presence of secondary modes). While the lidar-only retrieval type strictly follows a Bayesian approach, both other types use simplified approaches mainly due to limitations of available computation time. The complete range of solutions, as found by the former retrieval type, is not found by the latter approaches, but rather a set of solutions of the retrieval problem.

3.1. Bayesian formulation of retrieval problems

Forward simulations allow one to predict the set of observed parameters $\mathbf{o} = \{o^1, o^2, \dots\}$ when making observations of a certain physical system (Mosegaard and Tarantola, 1995). Physical systems used in forward simulations are referred to as 'models' in the following. Models are fully described by a set of physical parameters $\mathbf{m} = \{m^1, m^2, \dots\}$. Every model \mathbf{m} can be considered as a point in the model parameter space \mathcal{M} , and every observation \mathbf{o} can be considered as a point in the observation parameter space \mathcal{O} . The parameters can, in general, take continuous values. Forward simulations solve problems in the form

$$\mathbf{o} = f(\mathbf{m}) \tag{3.1}$$

where f maps from the model space \mathcal{M} into the observation space \mathcal{O} . The retrieval problem, in principle, is formulated as

$$\mathbf{m} = f^{-1}(\mathbf{o}). \tag{3.2}$$

That is: Given an observation \mathbf{o} , which are the actual values of the physical parameters of the observed system? This formulation implies that a unique solution \mathbf{m} exists for each observation \mathbf{o} .

The observed parameters \mathbf{o} , however, are typically associated with some uncertainty, thus no unique solution \mathbf{m} exists for the retrieval problem, but rather a range of solutions \mathbf{m} fits the observation \mathbf{o} within the uncertainty of the observation. Due to this ambiguity, the retrieval problem for given observation \mathbf{o} is better expressed in a probabilistic manner. This can be achieved by using probability densities in the model space \mathcal{M} and the formulation (Mosegaard and Tarantola, 1995; Mosegaard and Tarantola, 2002):

$$\rho_{\text{post}}(\mathbf{m}) = k \cdot P_{\text{fit}}(\mathbf{m}) \cdot \rho_{\text{prior}}(\mathbf{m}), \quad (3.3)$$

where $P_{\text{fit}}(\mathbf{m})$ is the likelihood function for the agreement between the models in the space \mathcal{M} and the actual observation \mathbf{o} . $\rho_{\text{prior}}(\mathbf{m})$ and $\rho_{\text{post}}(\mathbf{m})$ describe the probability density distribution of the models in the model space \mathcal{M} before and after considering the observation; probability density distributions describe the relative likelihood of the models in the model space \mathcal{M} ; they are always non-negative and their integrals over the whole space \mathcal{M} are equal to one. k is an appropriate positive normalization constant.

For each \mathbf{m} in \mathcal{M} , Eq. 3.3 is consistent with the Bayes theorem

$$P(\mathbf{m}|\mathbf{o}) = \frac{P(\mathbf{o}|\mathbf{m}) \cdot P(\mathbf{m})}{P(\mathbf{o})}. \quad (3.4)$$

The notation $P(a|b)$ denotes the probability of a given b . In the context of Bayesian retrievals, the probabilities P are probability densities. Comparison with Eq. 3.3 shows that $\rho_{\text{prior}}(\mathbf{m}) = P(\mathbf{m})$, $\rho_{\text{post}}(\mathbf{m}) = P(\mathbf{m}|\mathbf{o})$, and $k \cdot P_{\text{fit}}(\mathbf{m}) = P(\mathbf{o}|\mathbf{m})/P(\mathbf{o})$. Bayesian approaches have been used for the retrieval of aerosol parameters, e.g. for the retrieval of aerosol size distributions from Personal Cascade Impactors by Ramachandran and Kandlikar (1996). As mentioned in the introduction, for the retrieval from lidar observations, Bayesian approaches have been used only by Herman et al. (2008).

3.1.1. Determination of model space and priors

For the application of Eq. 3.3 to a retrieval problem, the model space \mathcal{M} needs to be defined, that is, the set of parameters ('dimensions' of \mathcal{M}) and their physical meaning. To determine upon the number of dimensions of \mathcal{M} , a trade-off between the complexity of the observed system and the information content of the observed parameters is required. On the one hand, a certain number of dimensions of \mathcal{M} is necessary to explain the observations by models; on the other hand, if models have a too large degree of freedom (i.e., \mathcal{M} has too many dimensions), very diverse models may explain the observations, so that a successful retrieval of microphysical properties is not possible. In this respect, care needs to be taken when assumptions are made because assumptions may bias the retrieval results. After the definition of \mathcal{M} , a prior probability density distribution $\rho_{\text{prior}}(\mathbf{m})$ needs to be specified. $\rho_{\text{prior}}(\mathbf{m})$ contains all information available about the system without considering

the observation \mathbf{o} . In general, the distribution $\rho_{\text{prior}}(\mathbf{m})$ can be quite complex, but if no information about the system is available, uniform distributions are used. In any case, for practical reasons, the physical parameters of the model space \mathcal{M} are assumed to be within certain ranges, such that extremely unrealistic parameter values are excluded. In this thesis, it is assumed that all models within predefined parameter ranges have equal probability, that is, $\rho_{\text{prior}}(\mathbf{m})$ is positive and constant within these ranges, but equal to zero outside these ranges (see Sect. 3.4.1).

The distribution $P_{\text{fit}}(\mathbf{m})$ in the model space \mathcal{M} not only depends on \mathbf{m} , but also on the actual observation \mathbf{o} and its uncertainty. For example, if the observation uncertainties are uncorrelated and normally distributed, $P_{\text{fit}}(\mathbf{m})$ is

$$P_{\text{fit}}(\mathbf{m}) = \exp \left[-\frac{1}{2} \sum_i \left(\frac{f^i(\mathbf{m}) - o^i}{\delta^i} \right)^2 \right], \quad (3.5)$$

where δ^i is the standard deviation of the i -th observed parameter o^i . $f^i(\mathbf{m})$ is the i -th forward-modeled observed parameter of model \mathbf{m} . In this thesis, Eq. 3.5 is not used for $P_{\text{fit}}(\mathbf{m})$; instead it is assumed that only models \mathbf{m} that fit the observation \mathbf{o} within their relative uncertainties Δ are acceptable as solutions of the retrieval problem; this means that $P_{\text{fit}}(\mathbf{m})$ for given observation \mathbf{o} is

$$P_{\text{fit}}(\mathbf{m}) = \begin{cases} 1 & \text{for } \max\left(\frac{f^1(\mathbf{m})-o^1}{o^1 \cdot \Delta^1}, \frac{f^2(\mathbf{m})-o^2}{o^2 \cdot \Delta^2}, \dots\right) \leq 1 \\ 0 & \text{any other } \mathbf{m} \end{cases}, \quad (3.6)$$

where Δ^i is the relative uncertainty of the i -th observed parameter o^i .

The retrieval result is the posterior probability density distribution $\rho_{\text{post}}(\mathbf{m})$ in the model space \mathcal{M} , which is, according to Eq. 3.3, the product of $\rho_{\text{prior}}(\mathbf{m})$ and $P_{\text{fit}}(\mathbf{m})$. The constant factor k in Eq. 3.3 is selected such that the integral of $\rho_{\text{post}}(\mathbf{m})$ over \mathcal{M} is equal to one. In this thesis, $P_{\text{fit}}(\mathbf{m})$ according to Eq. 3.6 and a uniform $\rho_{\text{prior}}(\mathbf{m})$ were selected, thus $\rho_{\text{post}}(\mathbf{m})$ is positive and constant within a certain volume in \mathcal{M} , whereas it is equal to zero anywhere else in \mathcal{M} . All models described by the points within this volume agree with the observation \mathbf{o} , whereas the \mathbf{m} outside this volume disagree with \mathbf{o} .

The retrieval result for any model parameter χ (be it a physical or any derived parameter) combines the posterior probability density distribution $\rho_{\text{post}}(\mathbf{m})$ with the distribution of this parameter $\chi(\mathbf{m})$ in the model space \mathcal{M} . For example, the probability that parameter χ is within χ_{min} and χ_{max} is the integral of $\rho_{\text{post}}(\mathbf{m})$ over the volume in space \mathcal{M} , where the condition $\chi_{\text{min}} < \chi < \chi_{\text{max}}$ is fulfilled.

3.1.2. Monte Carlo sampling

For the numerical evaluation of the probabilities, the model parameters, and their integrals over volumes in \mathcal{M} , Monte Carlo sampling is suitable. The basic idea of this sampling approach is that a large number of models \mathbf{m} are randomly selected according to the prior probability density $\rho_{\text{prior}}(\mathbf{m})$. For each sampled model \mathbf{m} , $P_{\text{fit}}(\mathbf{m})$ and $\rho_{\text{post}}(\mathbf{m})$ are

calculated together with the parameter of interest $\chi(\mathbf{m})$. From $\rho_{\text{post}}(\mathbf{m})$ and $\chi(\mathbf{m})$ of the sampled models \mathbf{m} it is possible to approximate, for example, the probability that parameter χ is within χ_{min} and χ_{max} .

The efficiency of this simple Monte Carlo approach depends on the relative amount of acceptable models. For example in geophysics, where probabilistic approaches are frequently applied for the retrieval of features of the Earth's interior from seismographic data (Mosegaard and Tarantola, 1995), this simple Monte Carlo approach is not sufficient because only a very small ratio of models fits the observations. To solve such problems more efficiently, the simple Monte Carlo approach is modified such that acceptable models are sampled more frequently ('importance sampling'). This can be done by using Markov chain approaches like the Metropolis algorithm (Metropolis et al., 1953). For the purpose of the present study, however, the described simple Monte Carlo approach provides sufficient efficiency.

3.2. Prerequisite: Optical data sets

For modeling the optical properties of any realistic aerosol ensemble \mathbf{m} , the optical properties of a large number of different particles are required. But yet the calculation of optical properties of single particles is computationally expensive, in particular, in case of non-spherical particles. As a consequence, for calculating aerosol ensemble properties in the context of a retrieval, it is impractical to calculate the properties of each single particle when needed. Instead, it is necessary to establish data sets that contain modeled optical properties of single particles, which are then used for calculating ensemble properties. Using such pre-calculated data sets, the speed of a retrieval may increase by several orders of magnitude. For the retrievals of this study, data sets for spheroids and irregularly-shaped particles were established.

3.2.1. Data set for spheroids

For modeling of optical properties of spheroids as introduced in Sect. 2.3, a code based on the exact T-matrix method (TMM) is available from Mishchenko and Travis (1998). Because of the limited range of particles that can be modeled by TMM, extensions for large particles are required. For this extension, the geometric optics method (GOM) is suitable. Codes based on GOM are available from Macke et al. (1995) (CGOM) and from Yang et al. (2007) (IGOM). These codes were used for modeling the optical properties of the spheroids in the data set. For spheres, that is for spheroids with aspect ratio $\epsilon' = 1$, the Mie code from Mishchenko et al. (2002) was used.

3.2.1.1. Approach for GOM calculations

The investigation of the accuracy of the two available GOM implementations in Sect. 2.3.3 allows one to find an optimum combination of CGOM and IGOM, which provides the most

property	angular resolution	method
q_{ext}	-	IGOM
q_{sca}	-	IGOM
\mathbf{F} from 0° to 1°	0.01°	Mie
\mathbf{F} from 1° to 2°	0.02°	CGOM
\mathbf{F} from 2° to 10°	0.1°	CGOM
\mathbf{F} from 10° to 180°	0.5°	CGOM

Table 3.1.: Angular resolution of scattering matrix \mathbf{F} and numerical methods of GOM calculation for spheroid data sets.

accurate modeling for lidar and photometer applications. Most critical in this respect is the backscattering. In Sect. 2.3.3 it was shown that the accuracy of backscattering from CGOM is slightly better than the accuracy from IGOM, thus \mathbf{F} from CGOM was selected for the spheroid data set. The angular resolution of the scattering matrix $\mathbf{F}(\theta)$ from CGOM was selected for accurate sampling of \mathbf{F} as a function of the scattering angle θ and for accurate optical modeling of the backward direction; only very few rays are collected in the backward angle bin if the angular resolution in backward direction is too high, thus an angular resolution of less than 0.5° in backward direction does not increase the accuracy of CGOM compared to the selected resolution. The efficiencies q_{ext} and q_{sca} from IGOM were used for the data set because of their better accuracy compared to the accuracy of these parameters from CGOM. The combination of methods and angular resolutions used for establishing the data set is summarized in Tab. 3.1.

3.2.1.2. Content and structure

parameter	range	steps
shapes	prolate and oblate spheroids	-
aspect ratio ϵ'	1.0 - 3.0 3.0 - 5.0	+ 0.2 + 0.4
real refr. index m_r	1.28 - 1.68 1.68 - 2.00	+ 0.04 + 0.08
imag. refr. index m_i	0.0 and 0.0005375 0.001075 - 0.1376	$\times \sqrt{2}$
size parameter x of Mie	0.001 - 2000	$\times 1.01$
size parameter x of TMM	0.001 - (10...118) upper limit depends on ϵ' and m	$\times 1.05$
size parameter x of GOM	10 - 2000	$\times 1.10$

Table 3.2.: Grid points of microphysical parameters in spheroid optical data set.

The microphysical parameters of a single spheroid in the data set are described by the cross-section-equivalent size parameter x , the real and imaginary part of the refractive index m , the aspect ratio ϵ' , and whether the spheroid is oblate or prolate. The sampling points for each microphysical parameter are given in Tab. 3.2. The ranges of the microphysical parameters cover the aerosol spectrum that is relevant for atmospheric aerosol at solar wavelengths. The data set contains properties of about 2.7 million spheroids modeled using TMM, and of about 0.44 million spheroids modeled using GOM.

The data is stored in *netcdf*-files. For the creation of these files a Fortran 90 code was developed, which uses the Mie-, TMM-, CGOM-, and IGOM-codes as subroutines for modeling the optical properties of single particles. Each file contains the optical properties as a function of the size parameter in the range given in Tab. 3.2. For each combination of particle shape, aspect ratio ϵ' , refractive index $m = m_r + m_i i$, and modeling method, one *netcdf*-file was created. For example, the file *spheroid_0.625_1.5200_0.004300.nc* contains the properties of prolate spheroids with aspect ratio $\epsilon' = 1.6$ and $m = 1.52 + 0.0043i$, calculated by the T-matrix method. In case of prolate spheroids, $1/\epsilon'$ is used in the filenames, whereas ϵ' is used for oblate spheroids. File *impr_geom_sph_0.625_1.5200_0.004300.nc* contains properties for same particle shape and refractive index m , however, calculated using the method combination given in Tab. 3.1 and the size parameter range from $x = 10$ to $x = 2000$ (Tab. 3.2). Each file contains all relevant microphysical and optical properties of the modeled particles, e.g., it contains the radius conversion factor ξ_{vc} as well as an array of cross-section-equivalent size parameters x together with arrays of the extinction efficiencies q_{ext} and the scattering efficiencies q_{sca} at these x . The T-matrix method calculates expansion coefficients of the scattering matrix \mathbf{F} (Mishchenko and Travis, 1998), which allow one to calculate \mathbf{F} at any scattering angle θ . For particles modeled using TMM, these expansion coefficients are stored for each size parameter. For particles modeled using GOM, the six relevant elements of the scattering matrix at each size parameter are stored at 571 scattering angles, as given in Tab. 3.1.

3.2.2. Data set for irregularly-shaped particles

A data set with optical properties of single randomly-oriented irregularly-shaped particles, shown in Fig. 2.2, was established. The optical properties were calculated using the ADDA code and the approach described in Sect. 2.3.4.

The data set contains the complete set of optical particle properties (q_{ext} , q_{sca} , $\mathbf{F}(\theta)$) for 4 real parts of the refractive index m_r (1.48, 1.52, 1.56, and 1.60), for 6 imaginary parts m_i (0, 0.00215, 0.0043, 0.0086, 0.0172, and 0.0344), for 37 volume-equivalent size parameters x_v up to 20.8 (step width +0.2 for $x_v \leq 2.0$, and logarithmically-equidistant steps of factor ≈ 1.1 for $x_v \geq 2.0$), and for the six irregular shapes that are shown in Fig. 2.2. An upper limit of the size parameter was necessary because the computation time rapidly increases with size parameter. The data set contains modeled optical properties of about 165 000 individual particles.

The data set structure is the same as for the spheroid database, only the first parts of the filenames, which describe the particle shape, are different. The particle shape is indicated

by *shapeNNN_* instead of, e.g., *spheroid_0.625_*, where *NNN* is a number assigned to each shape. For example, *shape018_1.5200_0.004300.nc* contains the properties of particles with shape D (Fig. 2.2) and $m = 1.52 + 0.0043i$.

3.3. Sensitivity of observed parameters

The relationship between microphysical and optical properties, known from optical modeling, provides the basis for retrieving microphysical properties from remote sensing observations. For the feasibility of retrieving microphysical parameters from observations, it is necessary that the relationship between the microphysical parameters of interest and the observed parameters fulfills certain criteria. The most important criterion is that the observed parameters are sensitive to changes of the microphysical parameters of interest: if the observed parameters were independent of the microphysical parameters, ensembles with significantly different microphysical parameters would have the 'same' observed parameters. It would not be possible to retrieve the microphysical parameters because information about these microphysical parameters is missing in the observed parameters. A further criterion to be considered if assumptions about the microphysical properties were made is that the effects of the assumptions has to be smaller than the effects due to the sensitivity to the microphysical parameters.

This section investigates the relationship between microphysical and optical properties for single particles and particle ensembles. The optical properties that are relevant for lidar remote sensing and Sun photometry are covered, which allows for assessing the feasibility of retrieving microphysical properties using these remote sensing techniques.

3.3.1. Optical properties of single particles

As a first step, the optical properties of single particles are investigated. The optical properties are illustrated in Figs. 3.1, 3.5, and 3.6 for particles with different shapes and refractive indices as a function of the cross-section-equivalent size parameter x . In the left panels of these figures, optical properties for different shapes and fixed refractive index $m = 1.52 + 0.0043i$ are plotted. The colors and line types for the different shapes are indicated in Fig. 3.1e. Dotted lines denote undisturbed spheroids with three aspect ratios ϵ' . The same spheroids, but with surface deformations applied (Fig. 2.2, shapes A, B, and C), are plotted using solid lines. The other shapes (D, E, F) are plotted using dashed lines. In the right panels, optical properties for different refractive indices and two different shapes are plotted. The colors and line types for the different m and shapes are indicated in Fig. 3.1d. The red lines denote properties for different real part of the refractive index m_r , whereas the blue lines denote different imaginary parts m_i .

3.3.1.1. Extinction efficiency

The extinction cross section C_{ext} is the most fundamental parameter for the interaction of light with a particle because it is proportional to the amount of light interacting with a

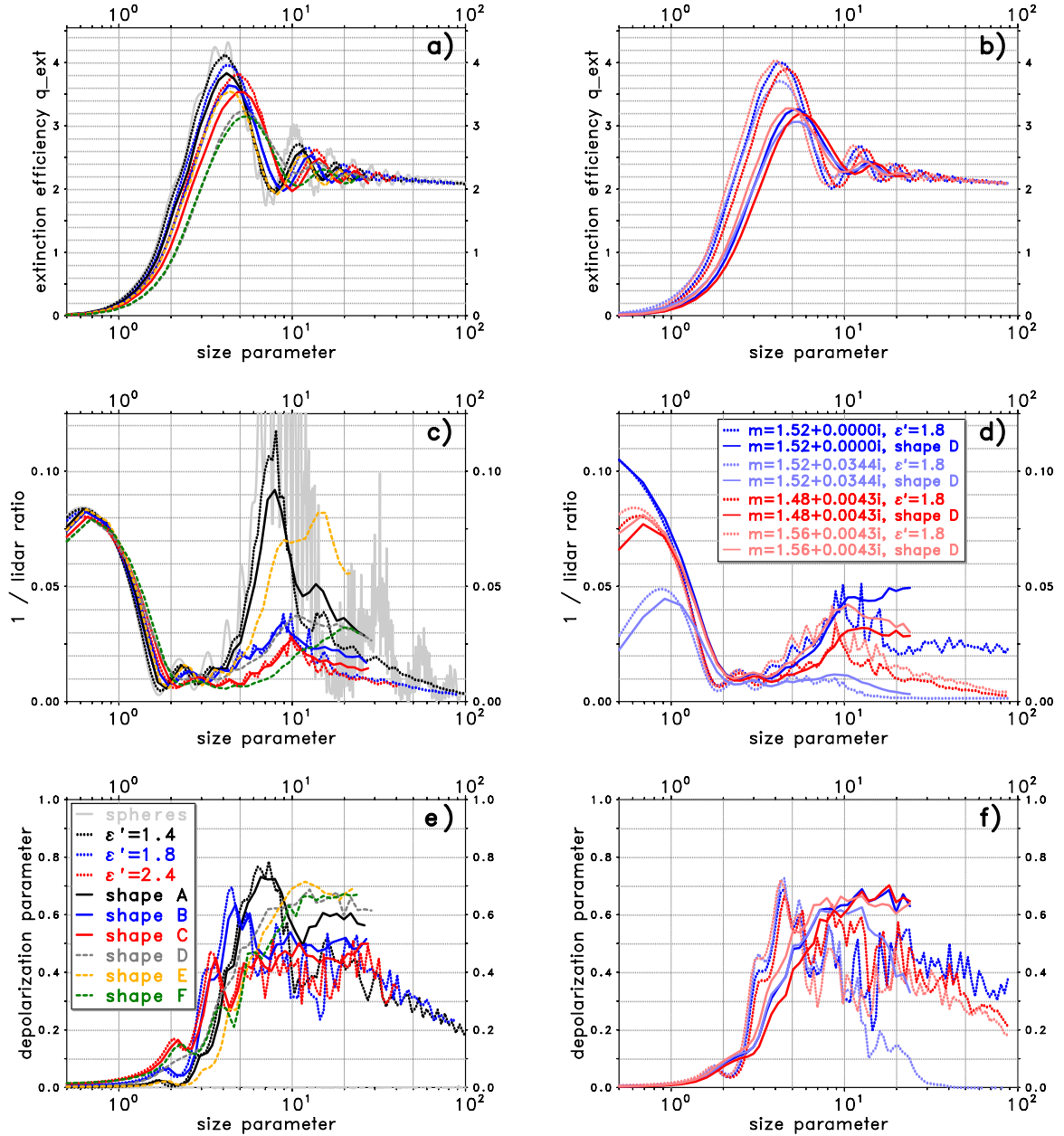


Figure 3.1.: Lidar-relevant optical properties over cross-section-equivalent size parameter x for single particles; left: fixed refractive index $m = 1.52 + 0.0043i$, but different shapes (spheres, prolate spheroids with different ϵ' , and irregularly-shaped particles of Fig. 2.2), see legend in panel e; right: spheroids and irregular shape D for different m , see legend in panel d.

particle (comprising absorption and scattering). As a consequence, C_{ext} is relevant for the calculation of all optical properties of aerosol ensembles (e.g., Eqs. 2.32, 2.41, 2.43, 2.46). The extinction efficiency q_{ext} , which is the ratio of the extinction cross section C_{ext} and the geometrical cross section C_{geo} of a particle, is shown in Figs. 3.1a and 3.1b as a function of the size parameter x .

The extinction efficiency q_{ext} at small size parameters ($x < 5$) is shape-dependent, i.e. extinction for given C_{geo} decreases with increasing non-sphericity (Fig. 3.1a). For example, the extinction by aggregates (shape D) at $x = 2$ is less than 50 % of the extinction by spheres with same C_{geo} . Furthermore, the extinction by small particles decreases with decreasing real part of the refractive index m_r (Fig. 3.1b). Absorption has only limited influence on q_{ext} , mainly reducing the amplitude of the oscillations of $q_{\text{ext}}(x)$. With increasing non-sphericity, the maximum of the extinction efficiency $q_{\text{ext}}(x)$ decreases and is shifted towards larger x . With increasing x , q_{ext} approaches to a value of 2 for all m and shapes (geometric optics limit).

3.3.1.2. Lidar ratio

Figures 3.1c and 3.1d show lidar ratios S as a function of the size parameter x . The inverse of the lidar ratio $1/S = q_{\text{diffsca}}(180^\circ)/q_{\text{ext}}$ is chosen as the vertical coordinate in these figures because the backscattering by a particle is proportional to the term ($C_{\text{ext}} \times 1/S$). Consequently, this term is used for the calculation of the backscatter coefficient β (Eq. 2.43), which is turn is necessary for the calculation of the lidar ratio S of a particle ensemble (Eq. 2.44).

Particles with size parameters $x < 4$ are not effective backscatterers (with reference to their cross section) because the extinction efficiency q_{ext} is small for $x < 2$ and $1/S$ is small for $2 < x < 4$ (Figs. 3.1c and d). For particles with sizes comparable to the wavelength ($4 < x < 10$), the shape dependence of the lidar ratio S is primarily an aspect-ratio dependence: backscattering strongly increases with decreasing aspect ratio ϵ' . Thus, in this size range, spherical particles are effective backscatterers and surface deformations have only minor influence, which can be seen by comparing deformed spheroids (solid lines) with undisturbed spheroids (dotted lines, same colors). Backscattering by aggregate particles (shape D) is also comparable to backscattering by spheroids with comparable aspect ratio ($\epsilon' = 1.8$). Backscattering by edged particles (shapes E and F) in the range $4 < x < 10$ is also strongly ϵ' -dependent: backscattering by a particle of shape E and size parameter $x \approx 8$ is almost 5 times as strong as backscattering by the corresponding particle of shape F (compare green and orange dashed lines in Fig. 3.1c).

For size parameters $x > 10$, backscattering is, in addition, sensitive to the other shape features: Spheroids with surface deformations exhibit slightly stronger backscattering than corresponding spheroids without deformations (Fig. 3.1c). Backscattering by aggregate particles (shape D) is clearly enhanced compared to backscattering by corresponding spheroids ($\epsilon' = 1.8$). This difference increases with size: backscattering by aggregate particles with size parameter $x \approx 20$ is more than twice as strong as backscattering by corresponding spheroids. At this size parameter, backscattering by particles of shape E,

which has the lowest aspect ratio ϵ' of the modeled non-spherical particles, is significantly stronger than backscattering by the other model particle shapes.

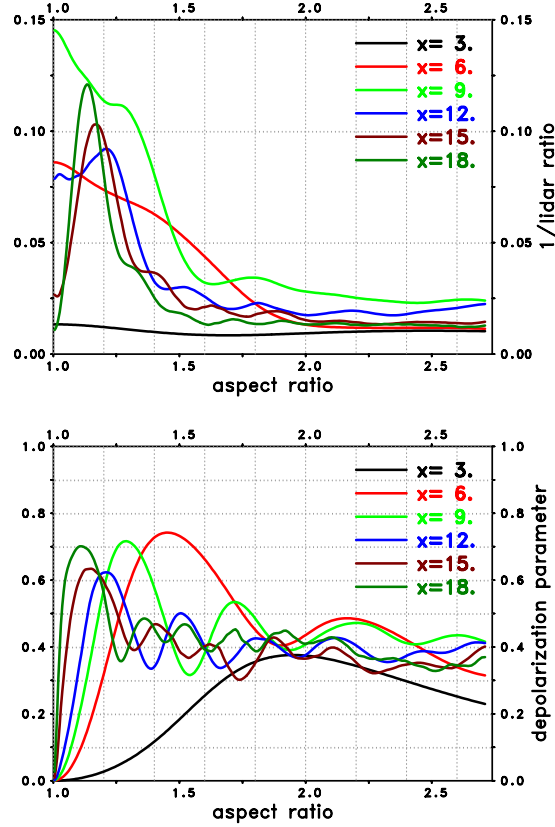


Figure 3.2.: $1/S$ and d over aspect ratio of prolate spheroids with different size parameters x (size-averaged over $\pm 5\%$) and $m = 1.52 + 0.0043i$.

To investigate the ϵ' -dependence of the backscattering in more detail, the inverse of the lidar ratio $1/S$ of spheroids with different size parameters is shown in Fig. 3.2 as a function of their aspect ratios ϵ' . Backscattering by spheroids with $x=3$ is hardly ϵ' -dependent, whereas for larger particles significant ϵ' -dependence of the backscattering is found. Starting at size-dependent aspect ratios ($\epsilon' \approx 2$ for $x=6$ and $\epsilon' \approx 1.6$ for $x=9$) the ϵ' -dependence is weak. The aspect ratio ϵ' of the maximum of $1/S(\epsilon')$ depends on the size parameter x of the particles. For $x=6$ and $x=9$, backscattering is strongest for $\epsilon'=1$ (spheres). For $x > 9$, the ϵ' of the maximum of $1/S(\epsilon')$ is larger than 1, which implies that the backscattering by spheroids within a certain range of aspect ratios ϵ' is stronger than backscattering by spheres. For example, for $x=12$ the maximum is at $\epsilon' \approx 1.21$ and for $x=18$ it is at $\epsilon' \approx 1.13$; interestingly, for $x=18$ backscattering by spheres is weaker than backscattering by spheroids with any $\epsilon' > 1$. In summary, this aspect-ratio dependence of the backscattering for $x > 4$ indicates that the lidar ratio S of an aerosol ensemble is not

only sensitive to the amount of spherical particles, but also to the amount of particles with low aspect ratios ϵ' .

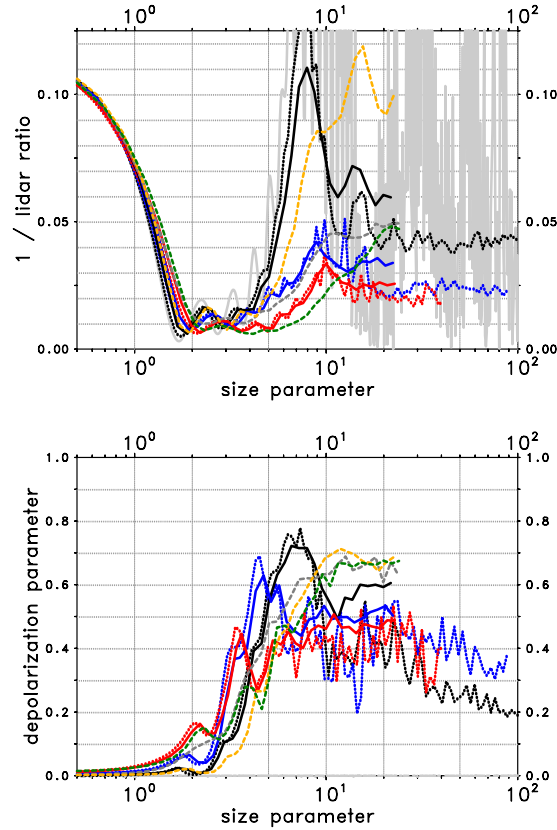


Figure 3.3.: Analogous to Fig. 3.1c and Fig. 3.1e, but $m = 1.52 + 0i$ (non-absorbing).

Figure 3.3 shows the same properties as Figs. 3.1c and 3.1e, but for non-absorbing particles ($m_i = 0$). The size dependence of the backscattering by non-absorbing particles with large size parameters ($x > 15$) is weak. Figure 3.1d shows very high S , i.e. weak backscattering, for strongly absorbing particles ($m_i = 0.0344$, light blue) with large x . Consequently, backscattering by large particles is clearly dominated by non-absorbing particles, if strongly absorbing and non-absorbing particles are mixed in an aerosol ensemble. This means that the size dependence of the lidar ratio S of such mixtures is also small.

For studying radiative effects using lidar observations, the sensitivity of lidar observations to the extinction by the particles is relevant. For this, the inverse of the lidar ratio, i.e., backscattering divided by the extinction is of interest, which was investigated above. For studying flight-safety-relevant effects of volcanic ash using lidar observations, however, the sensitivity of lidar observations to particle volume is relevant. To investigate this, Fig. 3.4 shows the backscattering at $\lambda = 1064$ nm, which is the maximum wavelength of the lidars, normalized by the particle volume. For particles with radii $r > 1 \mu\text{m}$, the

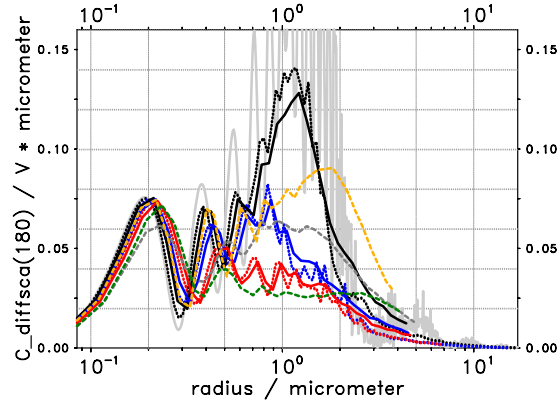


Figure 3.4.: Differential scattering cross section at $\theta = 180^\circ$ per volume ($C_{\text{diffsca}}(180^\circ)/V$) in μm^{-1} at $\lambda = 1064\text{ nm}$ over radius; analogous to Fig. 3.1c, but different normalization (volume vs. q_{ext}) and abscissa (r vs. x).

backscattered intensity per particle volume decreases with size. This is consistent with findings for spherical particles, e.g., from Müller and Quenzel (1985). Note, that the decrease of the plotted quantity in Fig. 3.4 is steeper than in Fig. 3.1c (both figures cover the same size range at $\lambda = 1064\text{ nm}$) because the backscattering is normalized by the volume in the former whereas it is normalized by the extinction (which is almost proportional to the cross section in case of large particles, Fig. 3.1a) in the latter. For particles with $r = 3\ \mu\text{m}$, the backscattered intensity per particle volume is only 15 % to 25 % of the corresponding value for particles with $r = 1\ \mu\text{m}$.

3.3.1.3. Depolarization

Depolarization parameters d of different particles are shown in Figs. 3.1e and 3.1f. The depolarization parameter d is selected as the vertical coordinate here because the product ($C_{\text{ext}} \times 1/S \times d$) is the relevant parameter for the calculation of the depolarization properties of aerosol ensembles (Eq. 2.46). As a simple example, it is mentioned that the depolarization parameter d of an ensemble of two particles with same C_{ext} and S , but different depolarization parameters $d = 0$ (non-depolarizing) and $d = 1$ (fully depolarizing) is $d = 0.5$, whereas the linear depolarization ratio of this ensemble is only $\delta_l = 0.333$. The relation between the depolarization parameter d and the linear depolarization ratio δ_l , which is observed by lidar, is given by Eq. 2.26.

The depolarization parameter d of small particles ($x < 2$) is low and primarily depends on the aspect ratio ϵ' . The depolarization parameter d is hardly sensitive to surface deformations for $x < 10$ (compare solid with dotted lines in Fig. 3.1e). For spheroids with aspect ratio $\epsilon' = 1.4$ and $\epsilon' = 1.8$, d has maxima at $x \approx 5$ and $x \approx 7$, respectively. Opposite to this, d of particles of shapes D, E, and F increase almost monotonically with particle

size up to $x \approx 10$. For comparisons, depolarization parameters d for other model particle shapes are available from other studies: The depolarization parameters d of Gaussian spheres ($\sigma = 0.2$), modeled by Lindqvist et al. (2009) for $x = 3$ to $x = 6$, are comparable to d of shape A. Zubko et al. (2007) investigated the influence of surface roughness on Gaussian spheres. They found that thick-layer roughness reduces d up to $x_{cs} = 12$ (x_{cs} was defined by Zubko et al. (2007) as the size parameter of a circumscribing sphere; the definition of x in the present thesis is estimated to result in 30% to 40% smaller x , i.e. $x \approx 8$). This reduction of d due to roughness is contrary to the insensitivity of the depolarization to surface deformations (shapes A, B, C, for $x < 10$). Note, that the type of particle roughness by Zubko et al. (2007) is substantially different from the surface deformations of model shapes A, B, and C.

Surface deformations are relevant for the depolarization parameter d of large spheroids ($x > 10$): d of spheroids with surface deformations is, on average, about 0.1 higher than d of corresponding spheroids without surface deformations. For size parameters $x > 10$, the depolarization parameter d of particles of shapes D, E, and F is in the range of 0.6 to 0.7, which corresponds to linear depolarization ratios δ_l close to 0.5. For the other particle shapes, d is smaller with values in the range of 0.3 to 0.6, corresponding to δ_l between 0.2 and 0.4. Ishimoto et al. (2010) modeled particles on which the so-called "spatial Poisson-Voronoi tessellation" was applied. They modeled the depolarization parameter d for two volume-equivalent size parameters x_v , and found $d \approx 0.74$ for $x_v = 14.8$ and $d \approx 0.62$ for $x_v = 24.7$. These values are comparable to the d of shapes D, E, and F. Figure 3.3 shows that the size dependence of the depolarization parameter of large non-absorbing particles is small.

The depolarization parameter of shapes E and F are comparable for size parameters $x > 4$, though their aspect ratios ϵ' and lidar ratios S are quite different. The depolarization parameters d of large spheroids ($x > 10$) are comparable for different aspect ratios ($\epsilon' = 1.4, 1.8, \text{ and } 2.4$). To illustrate the ϵ' -dependence of the depolarization in more detail, Fig. 3.2 shows d over the aspect ratio ϵ' of spheroids with size parameters from $x = 3$ to $x = 18$. For spherical particles ($\epsilon' = 1$) d is zero and strongly increases with increasing aspect ratio up to an size-dependent aspect ratio. For $x = 3$ the maximum d is reached for $\epsilon' \approx 1.95$, whereas for $x = 18$ the maximum d is found at $\epsilon' \approx 1.11$. For larger ϵ' there is no systematic ϵ' -dependence of the depolarization. This suggests that the aspect ratios ϵ' of large dust particles are not the primarily-relevant parameters for their depolarization properties. Edges, surface roughness, concave structures, and probably the overall shape, also influence the depolarization by large particles.

3.3.1.4. Forward scattering

Figure 3.5 shows the ratio $q_{\text{diffsca}}(\theta)/q_{\text{ext}}$ of different particles as a function of the size parameter x at scattering angles $\theta = 3^\circ$, $\theta = 4^\circ$, and $\theta = 6^\circ$. This ratio is selected because the product ($C_{\text{ext}} \times q_{\text{diffsca}}(\theta)/q_{\text{ext}}$) is relevant for the calculation of the scattering by aerosol ensembles (Eq. 2.41).

The ratio $q_{\text{diffsca}}(\theta)/q_{\text{ext}}$ at these θ strongly increases with increasing size parameter x , up

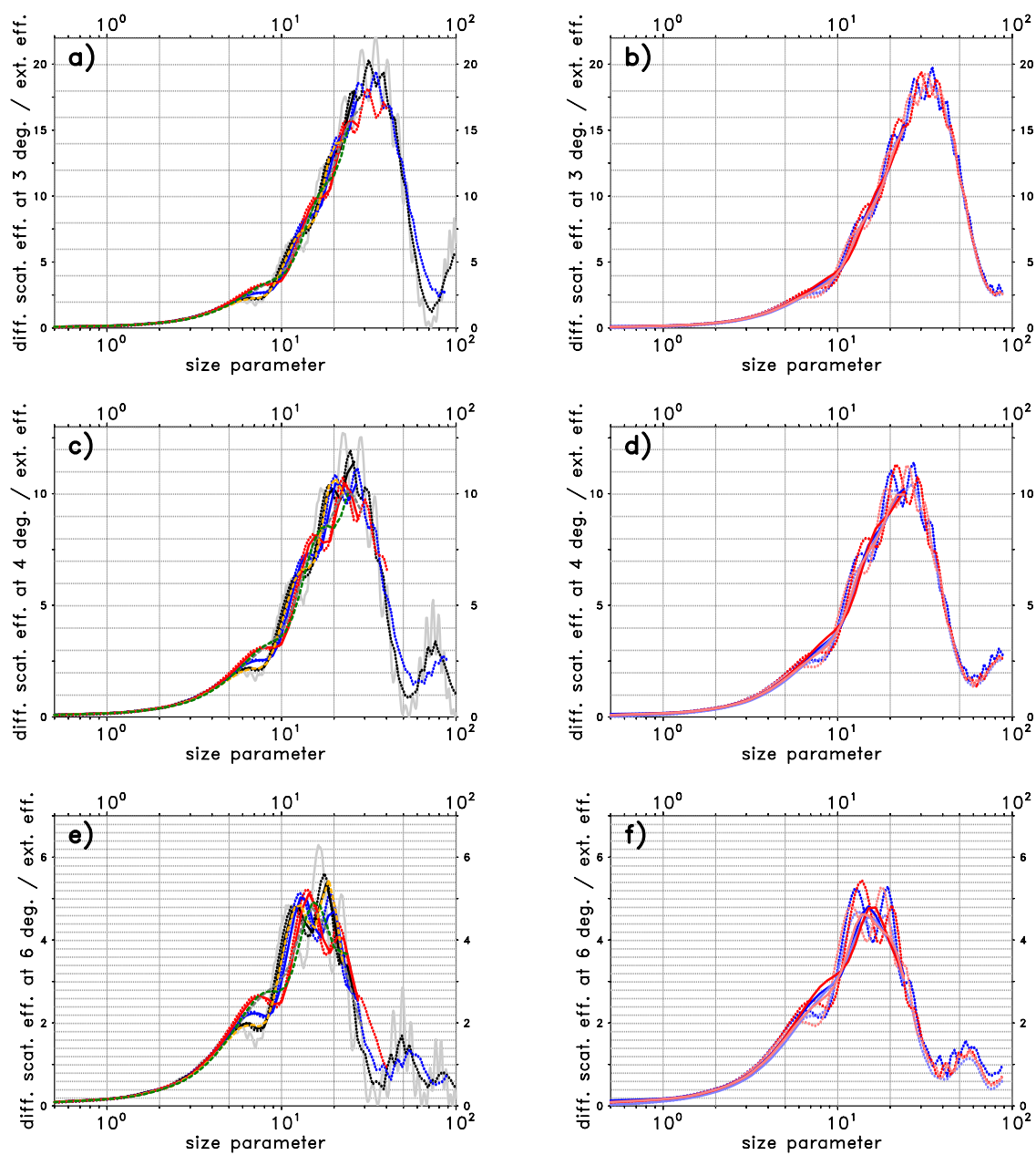


Figure 3.5.: Forward scattering properties over cross-section-equivalent size parameter x for single particles; same particles as in Fig. 3.1.

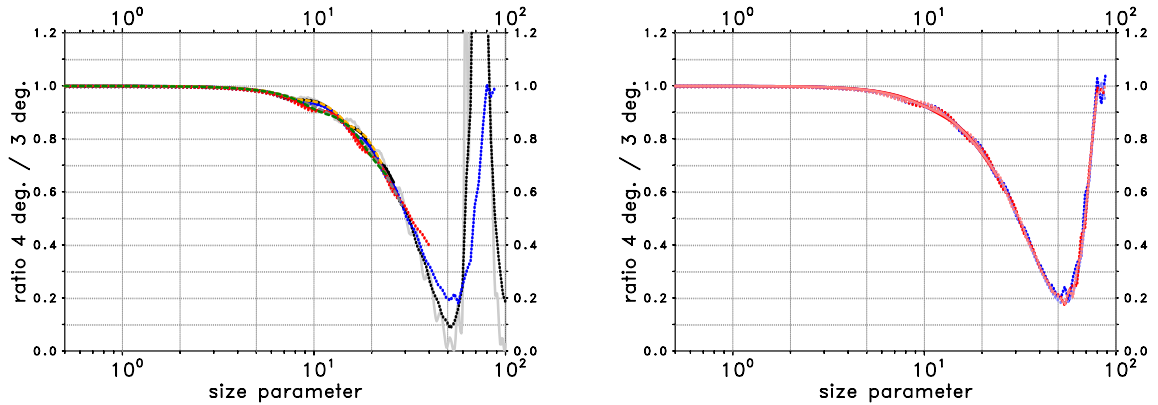


Figure 3.6.: Forward scattering properties over cross-section-equivalent size parameter x for single particles; same particles as in Fig. 3.1.

to a θ -dependent maximum; the maximum is at about $x = 35$ at $\theta = 3^\circ$, $x = 25$ at $\theta = 4^\circ$, and $x = 17$ at $\theta = 6^\circ$. The dependence of $q_{\text{diffsca}}(3^\circ)/q_{\text{ext}}$ on the particle shape and the refractive index is weak. At size parameters x larger than the x of the maxima of $q_{\text{diffsca}}(\theta)/q_{\text{ext}}$, the aspect ratio ϵ' has some systematic influence on $q_{\text{diffsca}}(\theta)/q_{\text{ext}}$; with increasing ϵ' , $q_{\text{diffsca}}(\theta)/q_{\text{ext}}$ as a function of x becomes smoother. With increasing scattering angle θ , the refractive index becomes increasingly relevant; e.g. for large particles ($x > 30$), m_i influences $q_{\text{diffsca}}(6^\circ)/q_{\text{ext}}$ (Fig. 3.5f, compare blue lines).

Figure 3.6 shows the ratio $q_{\text{diffsca}}(4^\circ)/q_{\text{diffsca}}(3^\circ)$ of different particles as a function of the size parameter x . These ratios are derived from the $q_{\text{diffsca}}(\theta)/q_{\text{ext}}$ plotted in Figures 3.5. The ratio $q_{\text{diffsca}}(4^\circ)/q_{\text{diffsca}}(3^\circ)$ primarily is a function of the size parameter x , and does hardly depend on the refractive index m . The ϵ' -dependence of $q_{\text{diffsca}}(4^\circ)/q_{\text{diffsca}}(3^\circ)$ for $x > 40$ is notably stronger than its m -dependence. At these size parameters x , however, the intensity of light scattered to 4° is comparatively weak (Fig. 3.5c) such that this ϵ' -dependence is, in general, of minor relevance for ensemble properties (which are calculated using Eq. 2.41).

Figure 3.7 shows scattering cross sections at 3° at the maximum wavelength of the standard CIMEL photometer, normalized by the particle volume. As mentioned above, normalization by the volume is useful for investigating the sensitivity of observations to the presence of particle volume. This figure corresponds to Fig. 3.5a where scattering at 3° is normalized by the extinction. The sensitivity of forward scattering to the shape of large particles is stronger in Fig. 3.7 than in Fig. 3.5a mainly because the shape dependence of the ratio between volume and cross section (see Eq. 2.3).

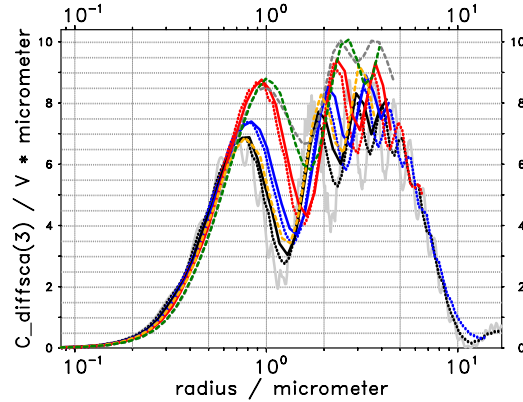


Figure 3.7.: Differential scattering cross section at $\theta = 3^\circ$ per volume ($C_{\text{diffsca}}(3^\circ)/V$) in μm^{-1} at $\lambda = 1020 \text{ nm}$ over radius; analogous to Fig. 3.5a, but different normalization (volume vs. q_{ext}) and abscissa (r vs. x).

3.3.2. Optical properties of particle ensembles

The sensitivity of optical properties of aerosol ensembles to changes of microphysical properties is studied in this section. The considered optical properties are the Ångström exponents κ_{ext} and κ_{bsc} for extinction and backscatter, the lidar ratio S , the depolarization of backscattered light and the scattering in the forward scattering direction. Table 3.3 to Table 3.6 contain the information about the microphysical properties of the considered ensembles.

Table 3.7 shows lidar-relevant optical properties of selected modeled aerosol ensembles. Table 3.8 shows, for the same aerosol ensembles, those optical properties that are relevant for Sun photometry. Columns in Tabs. 3.7 and 3.8 denote different aerosol ensembles, starting with a reference ensemble (see below), followed by modifications of this reference ensemble (labeled with the modified microphysical parameter, see Tab. 3.3).

3.3.2.1. Description of aerosol ensembles

Desert dust aerosols typically are mixtures of mineral dust particles and small ammonium particles (Kandler et al., 2009; Weinzierl et al., 2009). The ammonium particles are relevant for the optical properties at short wavelengths. The model ensembles described here are mixtures of one water-soluble component and three mineral dust components, as proposed by Hess et al. (1998) for the OPAC desert aerosol type. The microphysical properties of the ensembles are described by combining the parameters given in Tab. 3.3. For each microphysical parameter (labeled as \mathcal{A} to \mathcal{G}) two or more cases are considered. For this study, only the relative amount of particles in each of the four components is relevant because only intensive optical properties are modeled (except the sky radiances, where the number of particles is scaled according to the τ from the photometer observations, see

parameter	label	cases
shape of dust	\mathcal{A}	1: ABCDEF, 2: <u>BCDF</u> , 3: DF, 4: spheroids Dubovik, 5: spheroids Kandler, 6: spheres
real refr. index m_r of dust	\mathcal{B}	1: 1.48, 2: <u>1.53</u> , 3: 1.58
imag. refr. index m_i of dust	\mathcal{C}	1: λ -dep. m_i from OPAC, 2: λ -indep. $m_i = 0.004$ (Tab. 3.6)
m_i -distribution of dust	\mathcal{D}	1: homogeneous, 2: 1/3 non-absorbing, 3: <u>1/2 non-absorbing</u>
size distribution of dust	\mathcal{E}	changed according to Tabs. 3.4, 3.5
number of WASO particles	\mathcal{F}	1: 0, 2: 5, 3: <u>10</u>
rel. hum. (relevant f. WASO)	\mathcal{G}	1: 0%, 2: <u>50%</u>

Table 3.3.: Microphysical properties of model aerosol ensembles for sensitivity study; properties of reference ensemble (Sect. 3.3.2.2) are underlined; see text for details.

	WASO	MINM	MIAM	MICM
r_0 [μm]	0.0212 (0% r.h.) 0.0262 (50% r.h.)	0.07	0.39	1.90
σ	2.24	1.95	2.00	2.15

Table 3.4.: Modal radii r_0 and width σ of log-normal size distributions of components; adapted from Hess et al. (1998).

label	MINM	MIAM	MICM
$\mathcal{E}1$	0.933	0.0671	0.000108
$\mathcal{E}2$	0.917	0.0827	0.000226
$\mathcal{E}3$	<u>0.898</u>	<u>0.1016</u>	<u>0.000473</u>
$\mathcal{E}4$	0.875	0.1242	0.000987
$\mathcal{E}5$	0.847	0.1508	0.002045

Table 3.5.: Number N_0 of particles in dust components; properties of reference aerosol ensemble (Sect. 3.3.2.2) are underlined; $\sum N_0 = 1$.

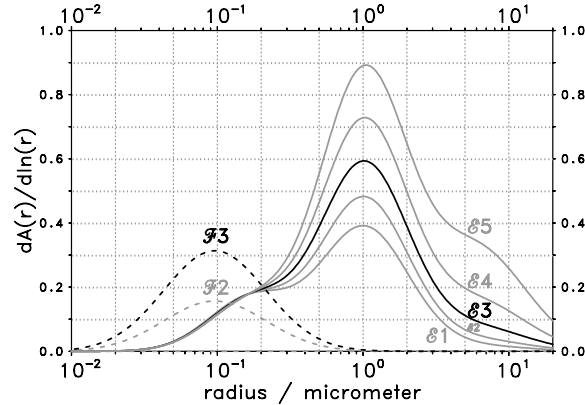


Figure 3.8.: Cross section area distributions of model ensembles (arbitrary scale) over particle radius; solid lines: sum of dust components (\mathcal{E} , Tab. 3.5); dashed lines: WASO component (\mathcal{F}) at 50 % r.h.

label	355 nm	532 nm	710 nm	1064 nm
$\mathcal{C}1$	<u>0.0166</u>	<u>0.0063</u>	<u>0.0040</u>	<u>0.0043</u>
$\mathcal{C}2$	0.0040	0.0040	0.0040	0.0040

Table 3.6.: Imaginary part of refractive index m_i of particles in dust components at the lidar wavelengths; properties of reference aerosol ensemble (Sect. 3.3.2.2) are underlined.

below). The number of particles is specified in each of the four components such that the total number of particles in the three mineral dust components is always equal to 1.

The first component of the model ensembles is the water-soluble (WASO) component which consists of small moderately-absorbing spherical particles. The size distribution and the refractive index m of the WASO particles depend on the relative humidity, due to their hygroscopicity; their properties are changed in accordance with OPAC. Two cases for the relative humidity are modeled (labeled as \mathcal{G} , Tab. 3.3), i.e. 0 % and 50 %. Three cases for the number of WASO particles (labeled as \mathcal{F}) are considered, namely 0, 5, and 10. As mentioned, the number of dust particles is always equal to 1, thus, the relative number of WASO particles in the ensembles is 0 %, 83.3 %, and 90.9 %, respectively.

The other three components of the aerosol ensembles are mineral dust components in different size ranges, i.e. the nucleation mode (MINM), the accumulation mode (MIAM), and the coarse mode (MICM). The modal radii r_0 and the widths σ of the log-normal size distributions (Eq. 2.28) of the components are given by OPAC and are independent of the relative humidity. For convenience, the numbers are given in Tab. 3.4. The number of particles N_0 in the mineral dust modes (label \mathcal{E}) are changed as given in Tab. 3.5.

The resultant size distributions are plotted in Fig. 3.8 as distributions of particle cross section. The number of large particles increases from $\mathcal{E}1$ to $\mathcal{E}5$, implying an increase of the average size of the dust particles. The N_0 of the modes of ensembles $\mathcal{E}1$ to $\mathcal{E}5$ were derived from transport parameterizations of the global aerosol data set GADS given by Koepke et al. (1997) for particle number densities of 75 cm^{-3} , 150 cm^{-3} , 300 cm^{-3} , 600 cm^{-3} , and 1200 cm^{-3} , respectively. This correlation was successfully applied for the interpretation of aerosol optical thickness measurements by Sun photometers during SAMUM-1 (Toledano et al., 2009).

The refractive index m of mineral dust particles is adapted from OPAC. The imaginary part m_i at the lidar wavelengths is given in Tab. 3.6 and sharply decreases from 355 nm to 532 nm (case $\mathcal{C}1$). The real part m_r is varied by ± 0.05 (labeled as \mathcal{B}), and an additional case with a wavelength-independent imaginary part $m_i = 0.004$ (labeled as $\mathcal{C}2$) is considered. At short wavelengths, the m_i of the wavelength-independent case is significantly smaller than the m_i from OPAC, whereas at long wavelengths, they are almost equal (see Tab. 3.6). All dust particles in an ensemble have the same real part m_r (as given by \mathcal{B}), but distributions of the imaginary part m_i are allowed with an average m_i as given by \mathcal{C} . Three relative distributions of the imaginary part m_i of the dust particles are covered (labeled as \mathcal{D}). Very often in optical modeling, m_i is assumed to be the same for all model particles; this is the first case ($\mathcal{D}1$, homogeneous mixture). In the other cases ($\mathcal{D}2$ and $\mathcal{D}3$, inhomogeneous mixtures), absorbing and non-absorbing dust particles are mixed. The m_i of the absorbing particles is selected such that the average of m_i is the same as for the homogeneous mixture. In case $\mathcal{D}2$, one third of the dust particles are non-absorbing ($m_i = 0$) and two thirds are absorbing particles with a m_i that is 50% higher than given by \mathcal{C} ; for example, m_i of two thirds of the dust particles in case $\mathcal{C}1\mathcal{D}2$ is 0.0249 at $\lambda = 355 \text{ nm}$, whereas $m_i = 0$ for one third of the dust particles. In case $\mathcal{D}3$ one half of the dust particles are non-absorbing and the m_i of the other dust particles is doubled compared to the m_i given by \mathcal{C} . The refractive indices m and the m_i -distributions of the dust particles are size-independent.

The mineral dust particles are non-spherical. For the dust particle shape (labeled as \mathcal{A}) different combinations of irregularly-shaped particles (Fig. 2.2) are considered. In the first case ($\mathcal{A}1$) all 6 particle shapes have equal abundance. In case $\mathcal{A}2$ the particles with low aspect ratio ϵ' (shapes A and E) are removed from the ensembles, and in case $\mathcal{A}3$ only the most "extreme" shapes (D and F) are present in the ensembles. For comparison, also ensembles of spheroids with the ϵ' -distributions from Dubovik et al. (2006) ($\mathcal{A}4$) and Kandler et al. (2009) ($\mathcal{A}5$), and ensembles of spheres ($\mathcal{A}6$) are modeled. On average, the spheroids in case $\mathcal{A}4$ have higher ϵ' than in case $\mathcal{A}5$.

Only volume-equivalent size parameters $x_v \leq 20.8$ are covered by the optical data sets for irregularly-shaped particles, which are used in cases $\mathcal{A}1$, $\mathcal{A}2$, and $\mathcal{A}3$. This x -range, however, does not cover the complete size spectrum of mineral dust aerosols at the wavelengths of the remote sensing instruments. Thus, extensions are required for large particles. In cases $\mathcal{A}1$, $\mathcal{A}2$, and $\mathcal{A}3$, optical properties of prolate spheroids with the ϵ' -distribution from Kandler et al. (2009) are used for $x > 20.8$; this approach is labeled as $\mathcal{X}_{\text{spheroids}}$ in the following. As an alternative approach for the calculation of S and δ_1 of ensembles of irregularly-shaped particles (cases $\mathcal{A}1$, $\mathcal{A}2$, and $\mathcal{A}3$), it is assumed that S and δ_1 are

size-independent for $x \geq 20.8$; this approach is labeled as $\mathcal{X}_{\text{size-indep.}}$. The size dependence of S and δ_1 of non-absorbing particles was investigated in Sect. 3.3.1 and illustrated in Fig. 3.3. It was shown that the assumption about size-independent S and δ_1 for large particles is not unrealistic for mixtures of absorbing and non-absorbing particles because the size dependence of S and δ_1 of such mixtures is weak.

3.3.2.2. Selection of reference ensemble

As reference ensemble for the sensitivity study, an ensemble with optical properties that are consistent with those measured by lidar and Sun photometer during SAMUM-1 on 19 May 2006 in Ouarzazate, Morocco (see Sect. 4.3.1) is selected. On this day, favorable desert aerosol conditions were found and a multitude of measurement platforms were available (e.g., Müller et al., 2010a).

The relative humidity is 50 % in the reference ensemble ($\mathcal{G}2$), and the number of WASO particles is 10; thus 90.9 % of the particles in the reference ensemble are WASO particles ($\mathcal{F}3$). For comparison, 87.0 % of the particles of the OPAC desert mixture are WASO particles (Hess et al., 1998). The average refractive index m ($\mathcal{B}2$ and $\mathcal{C}1$), as well as the number of particles in the mineral dust modes ($\mathcal{E}3$), i.e., the relative size distribution of dust particles, is adapted from the OPAC desert mixture. Absorbing and non-absorbing dust particles are mixed with equal abundance ($\mathcal{D}3$), and a mixture of shapes B, C, D, and F, each having equal abundance, is assumed ($\mathcal{A}2$).

3.3.2.3. Ångström exponent κ_{ext} for extinction

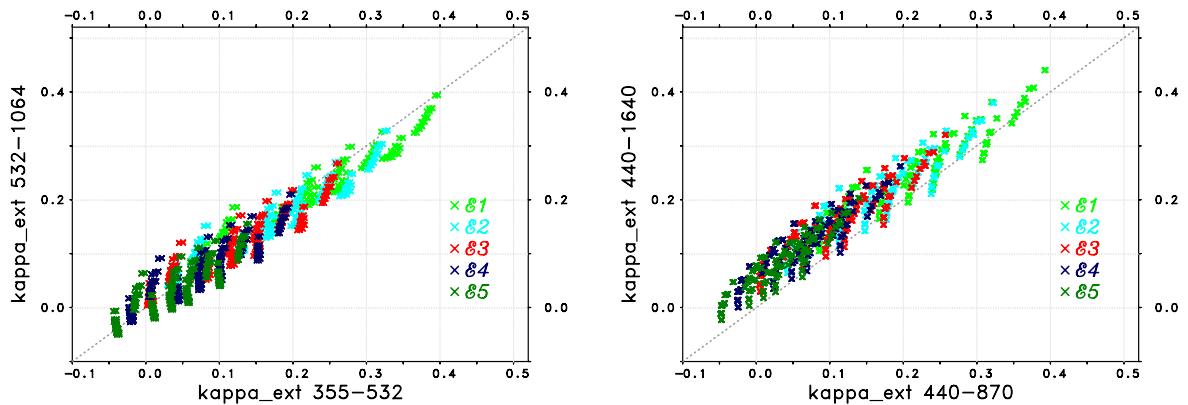


Figure 3.9.: Modeled κ_{ext} of all aerosol ensembles described in Tab. 3.3; different colors denote different dust size distributions (\mathcal{E} , see legend).

Figure 3.9 shows modeled Ångström exponents κ_{ext} for wavelength ranges observed by lidar (left) and Sun photometer (right). The κ_{ext} of all ensemble parameter combinations

ensemble	Ref.	$\mathcal{A}1$	$\mathcal{A}3$	$\mathcal{A}4$	$\mathcal{A}5$	$\mathcal{A}6$	$\mathcal{B}1$	$\mathcal{D}1$	$\mathcal{C}2\mathcal{D}1$	$\mathcal{E}5$	$\mathcal{F}1$	$\mathcal{G}1$
S_{355} [sr]	52	44	50	51	43	24	63	96	55	46	50	48
	54	<i>42</i>	<i>49</i>				<i>62</i>	<i>83</i>	<i>46</i>	<i>52</i>	<i>53</i>	<i>50</i>
S_{532} [sr]	48	38	46	44	36	18	59	60	53	45	47	46
	48	<i>36</i>	<i>44</i>				<i>57</i>	<i>53</i>	<i>47</i>	<i>45</i>	<i>46</i>	<i>46</i>
S_{710} [sr]	47	36	46	42	33	15	59	53	53	45	47	47
	47	<i>35</i>	<i>44</i>				<i>56</i>	<i>49</i>	<i>49</i>	<i>44</i>	<i>46</i>	<i>46</i>
S_{1064} [sr]	53	40	53	46	35	16	66	58	57	50	53	53
	53	<i>39</i>	<i>50</i>				<i>64</i>	<i>55</i>	<i>54</i>	<i>49</i>	<i>53</i>	<i>53</i>
$\delta_{1,355}$	0.194	0.229	0.217	0.203	0.202	0.000	0.193	0.173	0.231	0.185	0.250	0.193
	<i>0.275</i>	<i>0.319</i>	<i>0.327</i>				<i>0.272</i>	<i>0.207</i>	<i>0.294</i>	<i>0.317</i>	<i>0.369</i>	<i>0.275</i>
$\delta_{1,532}$	0.245	0.289	0.279	0.236	0.250	0.000	0.245	0.259	0.264	0.234	0.287	0.250
	<i>0.306</i>	<i>0.349</i>	<i>0.359</i>				<i>0.305</i>	<i>0.295</i>	<i>0.307</i>	<i>0.341</i>	<i>0.362</i>	<i>0.312</i>
$\delta_{1,710}$	0.264	0.308	0.299	0.253	0.272	0.000	0.261	0.275	0.275	0.254	0.296	0.270
	<i>0.311</i>	<i>0.354</i>	<i>0.362</i>				<i>0.309</i>	<i>0.307</i>	<i>0.307</i>	<i>0.344</i>	<i>0.350</i>	<i>0.319</i>
$\delta_{1,1064}$	0.265	0.305	0.293	0.263	0.282	0.000	0.256	0.272	0.272	0.262	0.285	0.271
	<i>0.298</i>	<i>0.337</i>	<i>0.339</i>				<i>0.290</i>	<i>0.294</i>	<i>0.295</i>	<i>0.331</i>	<i>0.321</i>	<i>0.305</i>
$\kappa_{\text{bsc},355-532}$	0.06	-0.13	0.06	-0.17	-0.25	-0.55	0.07	-0.90	0.16	0.03	-0.14	0.11
	<i>-0.06</i>	<i>-0.17</i>	<i>-0.02</i>				<i>0.01</i>	<i>-0.88</i>	<i>0.30</i>	<i>-0.20</i>	<i>-0.29</i>	<i>-0.01</i>
$\kappa_{\text{bsc},532-1064}$	0.36	0.29	0.43	0.22	0.11	0.03	0.39	0.17	0.33	0.27	0.27	0.37
	<i>0.36</i>	<i>0.32</i>	<i>0.45</i>				<i>0.41</i>	<i>0.26</i>	<i>0.41</i>	<i>0.23</i>	<i>0.26</i>	<i>0.36</i>
$\kappa_{\text{ext},355-532}$	0.244	0.243	0.253	0.211	0.210	0.210	0.248	0.244	0.248	0.126	0.033	0.184
	0.216	0.207	0.242	0.171	0.155	0.146	0.237	0.216	0.217	0.109	0.070	0.167

Table 3.7.: Modeled lidar-relevant optical properties of selected dust aerosol ensembles; reference ensemble ("Ref.", i.e. combination $\mathcal{A}2\mathcal{B}2\mathcal{C}1\mathcal{D}3\mathcal{E}3\mathcal{F}3\mathcal{G}2$), and variations of reference ensemble (denoted with the varied parameter); italic numbers: results for assumption of size-independent S and δ_1 for $x \geq 20.8$ ($\mathcal{X}_{\text{size-indep.}}$).

ensemble	Ref.	$\mathcal{A}1$	$\mathcal{A}3$	$\mathcal{A}4$	$\mathcal{A}5$	$\mathcal{A}6$	$\mathcal{B}1$	$\mathcal{D}1$	$\mathcal{C}2\mathcal{D}1$	$\mathcal{E}5$	$\mathcal{F}1$	$\mathcal{G}1$
$K_{\text{ext},440-870}$	0.222	0.217	0.241	0.182	0.175	0.173	0.234	0.222	0.223	0.107	0.046	0.166
$K_{\text{ext},440-1640}$	0.258	0.243	0.289	0.208	0.184	0.166	0.286	0.258	0.258	0.150	0.128	0.214
$[F_{11}(4^\circ)/F_{11}(3^\circ)]_{440}$	0.679	0.682	0.678	0.689	0.689	0.688	0.681	0.678	0.680	0.642	0.669	0.674
$[F_{11}(6^\circ)/F_{11}(3^\circ)]_{440}$	0.362	0.365	0.360	0.376	0.375	0.370	0.365	0.360	0.363	0.323	0.343	0.352
$[F_{11}(4^\circ)/F_{11}(3^\circ)]_{500}$	0.697	0.699	0.696	0.707	0.707	0.706	0.699	0.696	0.697	0.653	0.689	0.693
$[F_{11}(6^\circ)/F_{11}(3^\circ)]_{500}$	0.386	0.389	0.384	0.401	0.399	0.396	0.390	0.384	0.387	0.340	0.371	0.378
$[F_{11}(4^\circ)/F_{11}(3^\circ)]_{1020}$	0.769	0.770	0.766	0.781	0.779	0.778	0.771	0.768	0.768	0.683	0.767	0.768
$[F_{11}(6^\circ)/F_{11}(3^\circ)]_{1020}$	0.518	0.520	0.513	0.536	0.533	0.530	0.522	0.517	0.517	0.405	0.513	0.515
$[F_{11}(4^\circ)/F_{11}(3^\circ)]_{1640}$	0.788	0.790	0.785	0.803	0.802	0.799	0.790	0.788	0.789	0.700	0.788	0.788
$[F_{11}(6^\circ)/F_{11}(3^\circ)]_{1640}$	0.564	0.567	0.556	0.587	0.586	0.582	0.566	0.564	0.565	0.425	0.563	0.563

Table 3.8.: Modeled Sun-photometer-relevant extinction and single scattering properties of same ensembles as in Table 3.7.

described in Tab. 3.3 are plotted in this figure; the colors of the crosses depend on the dust size distribution (parameter \mathcal{E}).

κ_{ext} does not strongly depend on the wavelength range of the lidars (crosses are close to diagonal in the left panel); specifically for the photometer wavelengths it is found that $\kappa_{\text{ext},440-1640}$ of most ensembles is higher than $\kappa_{\text{ext},440-870}$ by up to 0.1 (right). For the reference ensemble $\kappa_{\text{ext},355-532}$ is 0.244, $\kappa_{\text{ext},532-1064} = 0.216$, $\kappa_{\text{ext},440-870} = 0.222$, and $\kappa_{\text{ext},440-1640} = 0.258$ (Tabs. 3.7 and 3.8). The Ångström exponent κ_{ext} mainly depends on the size distribution of dust and WASO particle (\mathcal{E} , \mathcal{F} , \mathcal{G}). With decreasing contribution of small particles (MINM or WASO), κ_{ext} decreases. For example, $\kappa_{\text{ext},355-532}$ decreases from 0.244 to 0.033 and $\kappa_{\text{ext},440-1640}$ from 0.258 to 0.128, if WASO particles are removed from the reference ensemble. The shape of the dust particles is also relevant, particularly at long wavelengths. $\kappa_{\text{ext},440-1640}$ of dust spheroids and spheres ($\mathcal{A}4$, $\mathcal{A}5$, $\mathcal{A}6$) is lower by 0.050 to 0.092 than the $\kappa_{\text{ext},440-1640}$ of the reference ensemble which consists of irregularly-shaped particles.

3.3.2.4. Lidar ratio and Ångström exponent κ_{bsc} for backscatter

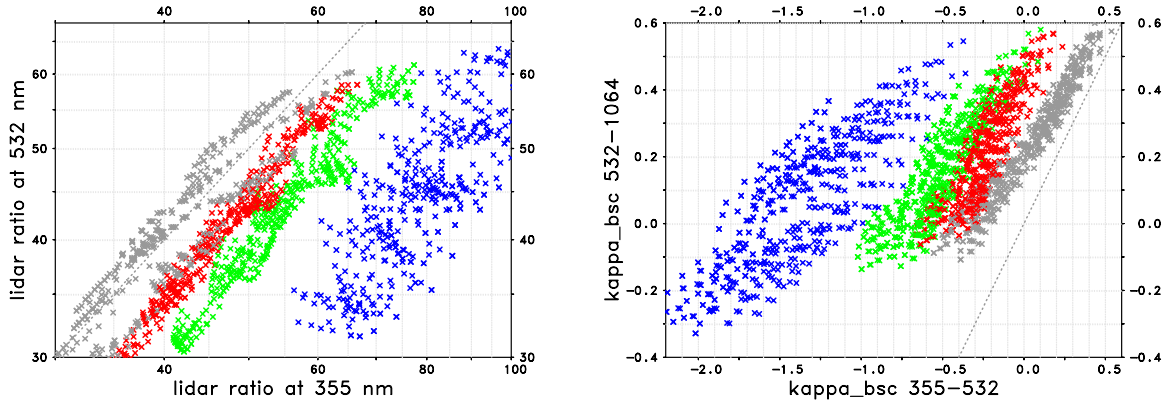


Figure 3.10.: Modeled lidar ratios S at 355 nm and 532 nm and Ångström exponent κ_{bsc} for backscatter of all aerosol ensembles described in Tab. 3.3, except combinations $\mathcal{C}2\mathcal{D}2$ and $\mathcal{C}2\mathcal{D}3$; blue crosses: homogeneous ensembles with m_i from OPAC ($\mathcal{C}1\mathcal{D}1$); green and red crosses: ensembles of absorbing and non-absorbing particles with average m_i from OPAC (green: $\mathcal{C}1\mathcal{D}2$; red: $\mathcal{C}1\mathcal{D}3$); grey crosses: homogeneous ensembles with λ -independent m_i ($\mathcal{C}2\mathcal{D}1$); grey dashed lines: λ -independent optical properties.

Modeled lidar ratios S at 532 nm over S at 355 nm for all ensembles described in Tab. 3.3, except combinations $\mathcal{C}2\mathcal{D}2$ and $\mathcal{C}2\mathcal{D}3$, are plotted in the left panel of Fig. 3.10; the S of irregularly-shaped particles (cases $\mathcal{A}1$, $\mathcal{A}2$, and $\mathcal{A}3$) were calculated with assumption $\mathcal{X}_{\text{size-indep.}}$. Blue crosses mark results for homogeneous mixtures with m_i from OPAC

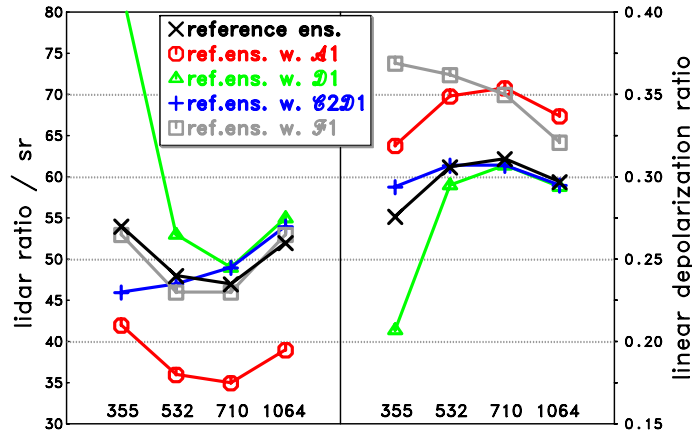


Figure 3.11.: Modeled lidar ratios S and linear depolarization ratios δ_l at different wavelengths in nm of selected aerosol ensembles described in Tab. 3.3: reference ensemble and modifications of the reference ensemble, labeled by the modified parameter; numbers are given in Tab. 3.7.

($\mathcal{C1D1}$), whereas green ($\mathcal{C1D2}$) and red ($\mathcal{C1D3}$) crosses denote mixtures of absorbing and non-absorbing particles. Results for homogeneous mixtures with wavelength-independent m_i ($\mathcal{C2D1}$) are marked as grey crosses. For each color, all combinations of the other parameters (\mathcal{A} , \mathcal{B} , \mathcal{E} , \mathcal{F} , \mathcal{G}) as given in Tab. 3.3 are plotted. Figure 3.11 illustrates the lidar-relevant optical properties of selected aerosol ensembles, i.e. the reference ensemble and selected modifications of the reference ensemble. These modifications are an ensemble with shapes A and E included ($\mathcal{A1}$), an ensemble where all dust particles have same m from OPAC ($\mathcal{D1}$), an ensemble where all dust particles have same wavelength-independent $m = 1.53 + 0.004i$ ($\mathcal{C2D1}$), and an ensemble without WASO particles ($\mathcal{F1}$).

The lidar ratio S of the reference ensemble is 54 sr at 355 nm, 48 sr at 532 nm, 47 sr at 710 nm, and 53 sr at 1064 nm, having a minimum at 710 nm. From Fig. 3.10 it is immediately clear that the imaginary part of the refractive index m_i and its distribution within the ensembles is relevant for the lidar ratio S at short wavelengths (compare different colors). E.g., S of the reference ensemble at 355 nm increases from 54 sr to 83 sr, if the mixture of absorbing and non-absorbing particles ($\mathcal{D3}$, red) is replaced by the corresponding homogeneous mixture ($\mathcal{D1}$, blue) with the same average refractive index m . Interestingly, lidar ratios S of homogeneous ensembles with wavelength-independent $m_i = 0.004$ (grey) do not significantly deviate from S of the much more realistic mixture of absorbing and non-absorbing particles with wavelength-dependent m_i from OPAC (red). This suggests that effects due to assuming unrealistic homogeneous absorption properties are partly compensated by assuming unrealistic wavelength independence of the refractive index m .

Furthermore, Tab. 3.7 and Fig. 3.11 illustrate that the lidar ratio S at all wavelengths is

also quite sensitive to the particle shape (\mathcal{A} , red) and to the real part of the refractive index m_r (\mathcal{B}). These sensitivities are the main reasons for the wide spread of crosses of same color in Fig. 3.10 and are consistent with findings from Wiegner et al. (2009). A decrease of m_r by 0.05 ($\mathcal{B}1$) increases S by about 10 sr. Spherical dust particles ($\mathcal{A}6$) reduce S by about 55 % to 70 % compared to the reference ensemble. A significant size dependence of S was found by Wiegner et al. (2009) for homogeneous ensembles, whereas the size dependence is only in the order of 2 sr to 4 sr for mixtures of absorbing and non-absorbing particles (compare $\mathcal{E}5$ to Ref.).

In the previous section it was found that backscattering by particles with low aspect ratios ($\epsilon' < \approx 1.4$) is significantly stronger than backscattering by particles with larger ϵ' . The presence of particles with small ϵ' also affects lidar ratios S of ensembles, which can be seen by comparing the reference ensemble with an ensemble in which particles with low ϵ' are included: S decreases by about 10 sr, if shapes A and E are included (ensemble $\mathcal{A}1$, Fig. 3.11). Similar differences are found between spheroids with the ϵ' -distribution from Dubovik ($\mathcal{A}4$, only few particles with $\epsilon' \leq 1.4$) and the ϵ' -distribution from Kandler ($\mathcal{A}5$, many particles with $\epsilon' \leq 1.4$).

In the right panel of Fig. 3.10, modeled backscatter-related Ångström exponents κ_{bsc} are shown for the lidar-relevant λ -ranges. Basically, this figure combines information from Figs. 3.9 (left) and 3.10 (left) because κ_{bsc} is a function of κ_{ext} and wavelength dependence of the lidar ratio S (Eqs. 2.36, 2.44, 2.45). $\kappa_{\text{bsc},355-532}$ of the reference ensemble is -0.06, which implies that the backscatter coefficient is virtually the same at 355 nm and 532 nm. If the mixture of absorbing and non-absorbing particles ($\mathcal{D}3$, red) is replaced by a homogeneous mixture ($\mathcal{D}1$, blue), κ_{bsc} is only -0.88, implying 43 % more backscattering at 532 nm than at 355 nm, which is in contradiction to typical mineral dust lidar measurements (e.g., Tesche et al., 2009). Thus, homogeneous mixtures result in an unrealistic wavelength dependence of backscattering, which is consistent with their above-mentioned unrealistic lidar ratio at 355 nm. For spheroids and spheres ($\mathcal{A}4$, $\mathcal{A}5$, $\mathcal{A}6$), κ_{bsc} is also lower (-0.17 to -0.55) than for the reference ensemble. For the wavelength range from 532 nm to 1064 nm, κ_{bsc} of the reference ensemble is 0.36, thus the backscatter coefficient decreases from 532 nm to 1064 nm by about 22 %.

3.3.2.5. Depolarization

Modeled linear depolarization ratios δ_1 are plotted in Fig. 3.12 for the same wavelength combination as the lidar ratio S in Fig. 3.10. Again, size-independent S and δ_1 for large irregularly-shaped particles is assumed in this figure ($\mathcal{X}_{\text{size-indep.}}$). The linear depolarization ratio δ_1 of the reference ensemble at 355 nm is 0.275. If spheroids are assumed for the large particles ($\mathcal{X}_{\text{spheroids}}$), δ_1 is notably lower ($\delta_1 = 0.194$), demonstrating the relevance of large particles ($x > 20.8$) for δ_1 of the ensemble at this wavelength. Though the assumption of size-independence for large particles ($\mathcal{X}_{\text{size-indep.}}$) might be not unrealistic, this fact highlights the need for accurate numerical methods for optical modeling of irregularly-shaped particles with large size parameters x . In most cases, δ_1 at 355 nm is lower than δ_1 at 532 nm (Fig. 3.12), except in cases without WASO particles ($\mathcal{F}1$). The linear depolarization

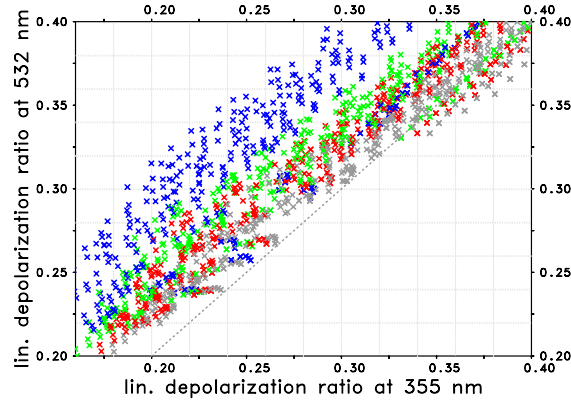


Figure 3.12.: Modeled linear depolarization ratios δ_1 at 355 nm and 532 nm for same aerosol ensembles as in Fig. 3.10.

ratio δ_1 of the reference ensemble is 0.306 at 532 nm, 0.311 at 710 nm, and 0.298 at 1064 nm. Thus, δ_1 of the reference ensemble has a maximum at 710 nm. Two counteracting effects, i.e., the low depolarization at small size parameters ($x < 3$, see Fig. 3.1) and the presence of WASO particles, give rise to this maximum. If spheroids are assumed at large size parameters ($\mathcal{X}_{\text{spheroids}}$), the maximum of δ_1 is shifted to larger λ , i.e., δ_1 does not decrease from 710 nm to 1064 nm.

The linear depolarization ratio δ_1 is sensitive to most of the microphysical aerosol parameters. First, δ_1 is sensitive to the particle shape (\mathcal{A}). Spheroid ensembles ($\mathcal{A}4$, $\mathcal{A}5$) have lower δ_1 than ensembles of irregularly-shaped particles (for assumption $\mathcal{X}_{\text{size-indep.}}$). Sphere ensembles ($\mathcal{A}6$) do not depolarize. Only minor dependence of δ_1 on the real part of the refractive index m_r (\mathcal{B}) is found for irregularly-shaped particles. In contrast to that, δ_1 of spheroids ($\mathcal{A}4$, $\mathcal{A}5$) is m_r -dependent; e.g., for $\mathcal{A}5$, δ_1 at 532 nm increases from 0.250 to 0.280, if m_r is reduced from 1.53 to 1.48 ($\mathcal{A}5 \mathcal{B}1$, not shown). This is consistent with findings from Wiegner et al. (2009), and indicates that the m_r -dependence of δ_1 is a specific feature of spheroids. Homogeneous mixtures with m_i from OPAC ($\mathcal{C}1 \mathcal{D}1$, blue) exhibit reduced δ_1 at 355 nm compared to the other ensembles (see Fig. 3.12). Furthermore, the linear depolarization ratio δ_1 is sensitive to the dust size distribution (\mathcal{E}), as δ_1 increases with increasing amount of large particles. For example, if $\mathcal{E}5$ is applied on the reference ensemble, δ_1 at 532 nm increases from 0.306 to 0.341. The number of WASO particles (\mathcal{F}) is also relevant for δ_1 , particularly at short wavelengths. δ_1 increases with decreasing number of WASO particles (which are spherical). For example, by removing the WASO particles from the reference ensemble, δ_1 at 355 nm increases from 0.275 to 0.369. The reduction of the relative humidity from 50 % to 0 % ($\mathcal{G}1$) results in a weak increase of δ_1 at long wavelengths (by 0.007 at 1064 nm).

3.3.2.6. Forward scattering

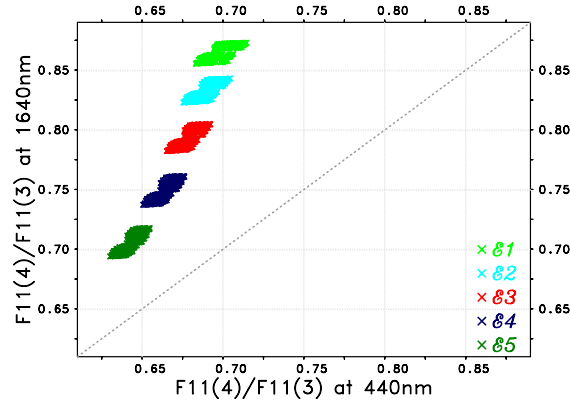


Figure 3.13.: Modeled ratio of phase functions for same aerosol ensembles as in Fig. 3.9; different colors denote different dust size distributions (\mathcal{E} , see legend).

Table 3.8 shows ratios of phase functions at different angles and wavelengths for selected ensembles (same ensembles as in Tab. 3.7). These ratios primarily depend on the size distribution and to a significantly lesser extent on the particle shape; they are almost independent of the refractive index and the WASO particles. These dependencies are also shown in Fig. 3.13, where ratios between scattering at 4° and 3° are plotted for all ensembles described in Tab. 3.3. The different colors denote different dust size distributions (\mathcal{E}). The ratios are grouped by the size distribution (different colors are separated). There are two sub-groups for each color. The upper-right sub-groups are for spheroids and spheres ($\mathcal{A4}$ to $\mathcal{A6}$), whereas the lower-left are of irregularly-shaped particles ($\mathcal{A1}$ to $\mathcal{A3}$).

3.3.3. Summary of sensitivity studies

As the first step of the sensitivity study, optical properties of single aerosol particles were investigated. It was found that backscattering by particles with low aspect ratios ($\epsilon' \leq 1.4$) is significantly stronger than backscattering by particles with high aspect ratios. Surface deformations do hardly affect backscattering or depolarization at size parameters $x < 10$. For larger particles, surface deformations on prolate spheroids moderately strengthen backscattering and depolarization. Large aggregate particles and edged particles result in stronger backscattering and depolarization than corresponding spheroids. In general, the size dependence of backscattering and depolarization of large non-absorbing particles is small. The forward scattering within the main diffraction peak of particles larger than the wavelength primarily depends on the particle size and only to a much lesser extent on particle shape and refractive index. Outside the main diffraction peak, where in general the scattering is significantly weaker than in the main peak, the particle shape and refractive index become relevant.

As the next step, optical properties were modeled for ensembles in which absorbing and non-absorbing irregularly-shaped dust particles are mixed. The wavelength-dependent refractive indices of dust from the aerosol database OPAC were considered. A sensitivity study revealed that non-absorbing dust components strongly affect the lidar ratio at short wavelengths. Interestingly, the lidar ratios of a homogeneous ensemble with wavelength-independent refractive index are similar to the lidar ratios of realistic dust ensembles; this indicates that effects due to common assumptions (homogeneity of m and wavelength independence of m) partly compensate each other. Consequently, it can be expected that no agreement with lidar observations is possible for models that only consider the wavelength dependence of m_i but not the inhomogeneity of the absorption properties. For typical dust refractive indices, ensembles of irregularly-shaped dust particles, in general, have higher linear depolarization ratios than ensembles of spheroids. The forward scattering (up to $\theta \sim 6^\circ$) by aerosol ensembles at solar wavelengths primarily depends on the coarse mode size distribution. This suggests that observations of forward scattering are well-suited for the retrieval of coarse mode size distributions of dust and ash aerosols.

3.4. Types of retrievals

Three types of retrievals were developed in this study. They are applicable depending on the availability of the remote sensing techniques and the observed aerosol type. These retrievals assume different complexity of the microphysical properties of the aerosol ensembles. Only one type of retrieval strictly follows the Bayesian approach (introduced in Sect. 3.1), whereas both other types are simplified retrievals which sample only a limited number of models due to limitations of available computation time.

The first retrieval type is applicable to observations of advanced lidar systems if the observed aerosol consists only of a single type of particles; the parameters are rigorously sampled using a Monte Carlo approach. The second retrieval type was developed for application to radiance observations in the solar aureole, in case the observed aerosol is dominated by particles with sizes comparable or larger than solar wavelengths and the vertical distribution of the aerosol layers is known, e.g. from lidar. The third type applies to collocated lidar and Sun photometer observations; this retrieval considers a limited number of rather complex aerosol models and may be regarded as a first attempt towards a rigorous and synergistic Bayesian retrieval from lidar and photometer observations.

3.4.1. Bayesian retrieval from lidar observations

The retrieval approach, described in this section, was applied to optical data from the MULIS and POLIS lidar observations of a volcanic ash layer (see Sect. 4.1). The retrieval considers extinction coefficients α_{ext} and linear depolarization ratios δ_1 at 355 nm and 532 nm, as well as the backscatter coefficients β at 355 nm, 532 nm, and 1064 nm. To investigate the information content of these optical parameters about microphysical parameters, this retrieval approach was also applied to synthetic lidar data (see Sect. 3.4.1.3).

parameter	lower boundary	upper boundary
r_0 (log. sampling)	0.01 μm	10 μm
σ	1.2	4.0
m_r	1.28	2.00
m_i	0.0	0.1
ζ	0	1
μ_p, μ_o	-0.6	0.6
σ_p, σ_o	0.5	1.5

Table 3.9.: Ranges of microphysical parameters for lidar inversion.

3.4.1.1. Model setup

The size distributions $n(r)$ of the ensembles of this retrieval type are mono-modal log-normal distributions, as given by Eq. 2.28. They are specified by the modal radius r_0 and the width σ of the mode. As only intensive properties are retrieved in the first step, N_0 becomes only relevant in the second step, where extensive properties are provided (see below). The particles sizes are specified by cross-section-equivalent radii r_c . The model aerosol ensembles cover a range from $r_{\min} = 20 \text{ nm}$ to $r_{\max} = 20 \mu\text{m}$. The wavelength-independent refractive index is given by a real part m_r and an imaginary part m_i . All particles of an ensemble have the same m . The ensembles consist of spheroids, and the shape distribution is specified by five parameters: Parameter ζ describes the relative frequency of prolate spheroids; this implies the frequency of oblate spheroids to be $(1-\zeta)$. μ_p and σ_p specify the aspect ratio distribution $f_p(\epsilon')$ (adapted from Kandler et al., 2007) of prolate spheroids:

$$f_p(\epsilon') = \frac{1}{\sqrt{2\pi}\sigma_p(\epsilon' - 1)} \exp \left[-\frac{1}{2} \left(\frac{\ln(\epsilon' - 1) - \mu_p}{\sigma_p} \right)^2 \right] \quad (3.7)$$

μ_o and σ_o are the corresponding parameters for the aspect ratio distribution $f_o(\epsilon')$ of oblate spheroids, which is independent of $f_p(\epsilon')$. Narrow aspect ratio distributions ($\sigma_{p/o} < 0.5$) are not allowed because wide aspect ratio distributions are necessary for realistic simulations of optical properties (see e.g., Mishchenko et al., 1997). The refractive index and the particle shape are size-independent. The ranges of the microphysical ensemble parameters for this retrieval type are summarized in Table 3.9.

3.4.1.2. Retrieval approach

Microphysical aerosol properties are retrieved by repeated forward calculations of model aerosol ensembles with varying microphysical properties within the ranges given in Table 3.9 and by comparison of their optical properties with the optical properties from the lidar measurements (here $\alpha_{\text{ext},355}$, $\alpha_{\text{ext},532}$, β_{355} , β_{532} , β_{1064} , $\delta_{1,355}$, $\delta_{1,532}$). Figure 3.14 shows a flow chart of this retrieval. In the first step, only intensive properties are retrieved, thus an aerosol ensemble is considered compatible with the lidar measurements, if all simulated (superscript s) linear depolarization ratios and ratios between extensive properties

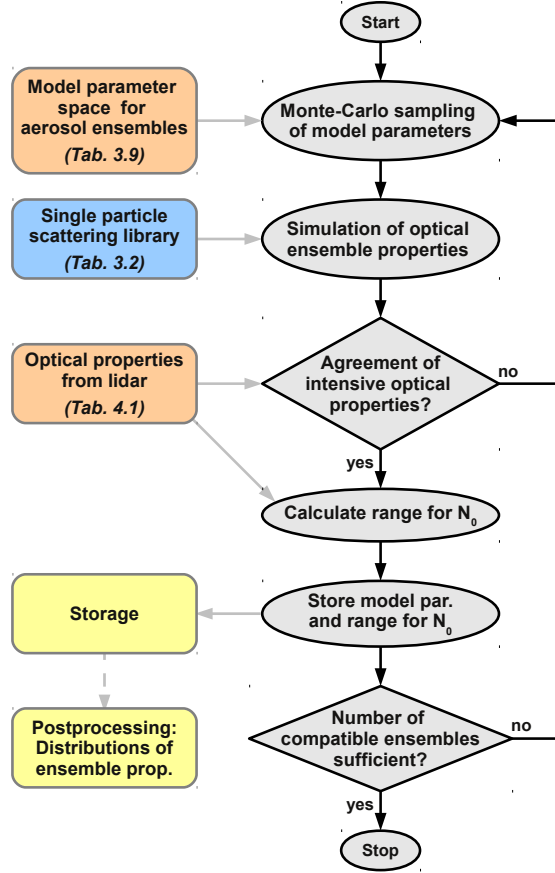


Figure 3.14.: Flow chart of rigorous retrieval from lidar measurements; colored boxes and grey arrows denote input and output.

are within the uncertainty ranges from the lidar measurements (superscript m), i.e.,

$$y^m(1 - \Delta_y) < y^s < y^m(1 + \Delta_y) \quad (3.8)$$

for $y \in \{\delta_{1,355}, \delta_{1,532}\}$, and

$$\frac{y_1^m(1 - \Delta_{y1})}{y_2^m(1 + \Delta_{y2})} < \frac{y_1^s}{y_2^s} < \frac{y_1^m(1 + \Delta_{y1})}{y_2^m(1 - \Delta_{y2})} \quad (3.9)$$

for $y_1, y_2 \in \{\alpha_{\text{ext},355}, \alpha_{\text{ext},532}, \beta_{355}, \beta_{532}, \beta_{1064}\}$. Δ_y denote the relative uncertainties of the measured parameters y . Eqs. 3.8 and 3.9 are equivalent to the condition given in Eq. 3.6. In the second step, for each compatible aerosol ensemble, the range of particle number densities $N_0 = \int n(r)dr$ from $N_{0,\text{min}}$ to $N_{0,\text{max}}$ is calculated, for which simulated extensive properties are within the uncertainty ranges from lidar, i.e.,

$$y^m(1 - \Delta_y) < y^s < y^m(1 + \Delta_y) \quad (3.10)$$

for $y \in \{\alpha_{\text{ext},355}, \alpha_{\text{ext},532}, \beta_{355}, \beta_{532}, \beta_{1064}\}$. For statistical analyses, N_0 in the range from $N_{0,\text{min}}$ to $N_{0,\text{max}}$ is assumed to be equiprobable. The result of the inversion is a distribution of compatible aerosol ensembles together with their compatible ranges for N_0 . Any property of interest, for example the mass-extinction conversion factor η , can be derived from this distribution of ensembles. As a consequence, the solution for the property of interest is also a distribution. In this thesis, the medians of the distributions, i.e. the values separating the distributions into two equiprobable parts, are given. Ranges including 95% of the solutions are denoted as (min ·· max).

The parameters of the model aerosol ensembles are randomly sampled within wide ranges (see Tab. 3.9) using a Monte Carlo approach with a Mersenne Twister pseudo random number generator (MT19937). The sampling is continued until a sufficient number of compatible aerosol ensembles is found. Whereas for a first estimate of the microphysical properties 100 ensembles may be sufficient, for smooth distributions of retrieved parameters significantly more ensembles are necessary. On one core of an Intel Xeon 5130 processor, about 5000 ensembles per second are modeled, but the computational speed of the retrieval also depends on the probability to find compatible ensembles. For the wide ranges given in Table 3.9 and the application presented in the subsequent chapter, the ratio of compatible ensembles to all ensembles was only about 1:200 000. As a consequence, if all four cores of the processor are used, about 360 compatible ensembles per hour were found.

This retrieval type was applied to lidar measurements of volcanic ash in Maisach on 17 April 2010, as described in Sect. 4.1. In addition, it was applied to simulated lidar measurements to investigate the information content of lidar data, as described in the following.

3.4.1.3. Information content of lidar data

The information content of lidar data was explored by applying the described retrieval to simulated lidar measurements. To demonstrate the benefit of measurements of the linear depolarization ratio δ_1 , two sets of lidar data were used: one set included the linear depolarization ratio δ_1 , whereas δ_1 was removed in the other set.

a) Lidar data including depolarization

For the exemplary exploration of the information content of lidar measurements of non-spherical aerosols, the lidar configuration of the lidar system of the Meteorological Institute Munich (see Sect. 2.6.1.3) including seven parameters was selected, that is α_{ext} and δ_1 at two wavelengths, and β at three wavelengths. The aerosols observed by the model lidar consisted of prolate spheroids with the ϵ' -distribution from Kandler et al. (2009), a m typical for dust, and a size distribution with an effective radius close to $1 \mu\text{m}$. For the purpose of this simulated measurement this ensemble is referred to as the ‘truth’. Fig. 3.15 illustrates the properties of ensembles found using the inversion approach and aerosol model described above. Three cases for the relative measurement uncertainty (0.5 %, 2 %, 8 %) were considered; in each case, all seven lidar parameters had the same relative uncertainty (Δ_y of Eqs. 3.8 and 3.9). The true properties are marked by the black crosses and the cross

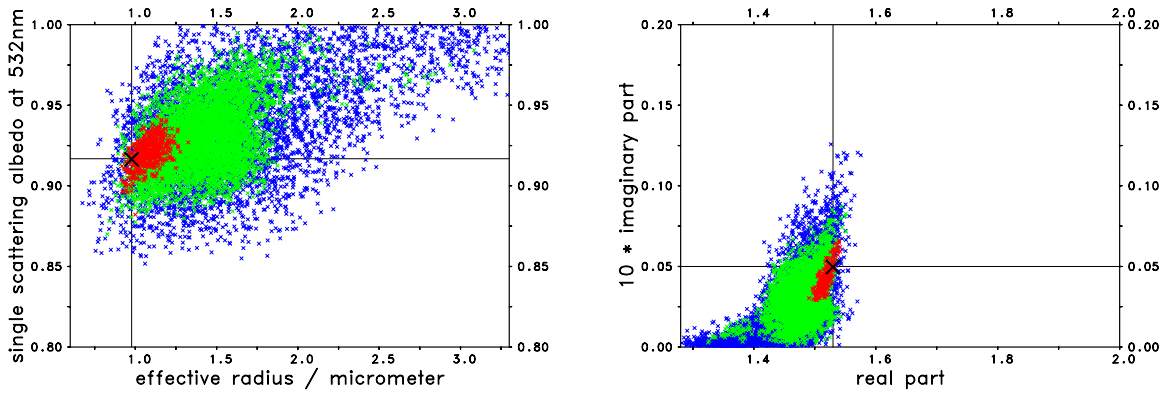


Figure 3.15.: Parameters of compatible aerosol ensembles for simulated measurements of α_{355} , α_{532} , β_{355} , β_{532} , β_{1064} , $\delta_{1,355}$, $\delta_{1,532}$; different relative measurement errors: 0.5 % (500 ensembles, red), 2 % (10000 ens., green), 8 % (10000 ens., blue); prolate spheroids with $\sigma_p=0.6$, $\mu_p=-0.45$, $m = 1.53 + 0.005i$, $r_{\text{mod}} = 0.1 \mu\text{m}$, $\sigma = 2.6$ in the simulated measurements; inversion using spheroids (Tab. 3.9).

hairs. The left panel shows that the single scattering albedo ω_0 and the effective radius r_{eff} were well reconstructed (± 0.02 for ω_0 and $\pm 20\%$ for r_{eff}) from the measurements if the measurement uncertainties were small (0.5 %, red). For an measurement uncertainty of 8 %, ensembles with ω_0 from 0.85 to 1.00 agreed with the measurement. The upper limit of r_{eff} of the compatible ensembles considerably increased with increasing measurement uncertainty; for example, ensembles with more than three times larger r_{eff} than the true r_{eff} agreed with the measurement if its uncertainty was 8 %. From the right panel of Fig. 3.15 it becomes clear that also the uncertainty of the refractive index m strongly depended on the measurement uncertainty. For the smallest uncertainty, the m of all ensembles was close to the true m , whereas for 2 % and 8 %, most of the compatible ensembles had an m_r smaller than the true m .

b) Lidar data without depolarization

To demonstrate the importance of the linear depolarization ratio δ_1 in the retrieval of properties of non-spherical aerosols, the above-described example was modified by removing δ_1 from the lidar setup. Figure 3.16 shows the retrieval results for this new setup. The comparison with Fig. 3.15 shows that the uncertainties of the retrieved parameters increased significantly if δ_1 was not considered. If δ_1 was considered, there were only very few ensembles with an m_r larger than the true m (Fig. 3.15). By contrast, without considering δ_1 , most compatible ensembles had a higher m_r , even when the measurement uncertainty was low. This comparison indicates that δ_1 contains important information about the real part of the refractive index m_r , which is consistent with the m_r -dependence of δ_1 of spheroids found by Wiegner et al. (2009). As m_r and r_{eff} of the retrieved ensembles were

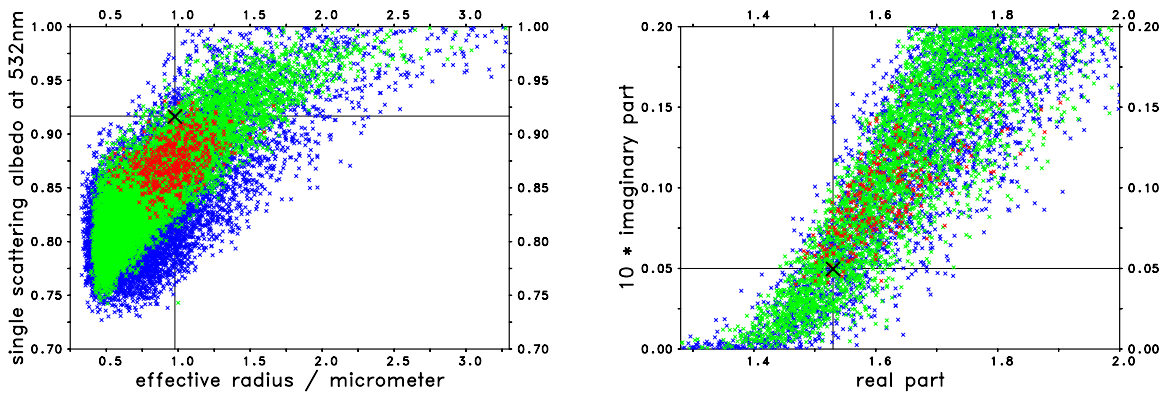


Figure 3.16.: Same as Fig. 3.15, but without consideration of $\delta_{1,355}$ and $\delta_{1,532}$.

correlated (not shown), there were also much more ensembles with r_{eff} smaller than the true r_{eff} if δ_1 was not considered.

3.4.2. Retrieval from photometer observations

The retrieval described here was applied to principle-plane aureole radiance observations of a CIMEL photometer (see Sect. 4.2). Using the ratio of sky radiances L at two scattering angles and one wavelength, it retrieves the effective radius r_{eff} and the conversion factor η between the mass concentration and the extinction coefficient of particles in a volcanic ash layer. Collocated lidar and ceilometer observations were used to identify the vertical structure and the types of the aerosols.

3.4.2.1. Model setup

This retrieval type was developed for a situation where an elevated layer of volcanic ash particles was observed above a boundary layer containing small spherical aerosol particles. For both aerosol layers different sets of properties are considered; they are summarized in Table 3.10.

For the boundary layer aerosol, spherical particles are assumed because low linear depolarization ratios δ_1 were observed by lidar (see next chapter). The values for the refractive index and the width of the size distributions cover the range of typical tropospheric aerosols. The effective radius r_{eff} of the boundary layer aerosol particles was estimated from the wavelength-dependence of the α_{ext} -profiles of the aerosols (shown in Sect. 4.2).

For the particles in the volcanic ash layer, different shapes are modeled, that are spheres as the most simple case and irregular shapes as shown in Fig. 2.2 (shapes B, D, and F). The irregular shapes include a prolate spheroid with surface deformations according to the Gardner series (Gardner, 1984) and aspect ratio $\epsilon' = 1.8$ (shape B), an aggregate

parameter	bound. layer aerosol	volcanic ash
shape	spheres	shapes B, D, F from Fig. 2.2; spheres (for comparison)
real refr. index m_r	1.35, 1.65	1.5, 1.6
imag. refr. index m_i	0.0, 0.05	0, 0.01
effective radius r_{eff}	0.11, 0.26 μm	0.8, 1.0, 1.2, 1.5, 2.0, 3.0 μm
form of size distr. (SD)	mono-modal: $\sigma = 1.6$ mono-modal: $\sigma = 2.4$	#1 mono-modal: $\sigma = 1.8$ #2 mono-modal: $\sigma = 2.4$ #3 bi-modal: $\sigma_{1/2} = 1.8$, $r_{0,1}/r_{0,2} = 0.25$, $N_{0,1}/N_{0,2} = 16$ #4 bi-modal: $\sigma_{1/2} = 1.8$, $r_{0,1}/r_{0,2} = 0.10$, $N_{0,1}/N_{0,2} = 100$
vertical extent	0.0–1.7 km	1.7–2.7 km
optical depth	0.056, 0.084	0.324, 0.216

Table 3.10.: Aerosol parameters considered for retrieval of volcanic ash properties from aureole observations at $\lambda = 1020$ nm; no aerosol in heights > 2.7 km; size distributions are mono-modal and bi-modal log-normal distributions.

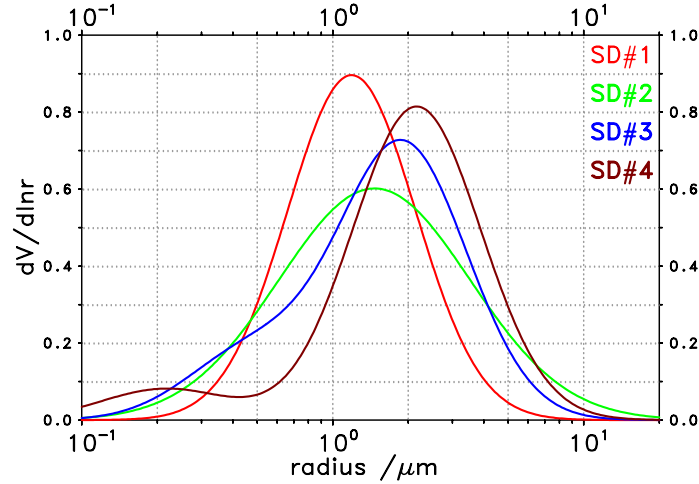


Figure 3.17.: Different forms of size distributions used for the aureole retrieval (SD, Table 3.10); shown is the volume distribution for $r_{\text{eff}} = 1 \mu\text{m}$.

particle (shape D), and a sharp-edged particle (shape F). As computation time significantly increases with the size parameter x , only $x \leq 20.8$ are available which corresponds to $r \leq 3.4 \mu\text{m}$ at $\lambda = 1020 \text{ nm}$. Particles with $r > 3.4 \mu\text{m}$ are spheroids with aspect ratios according to Dubovik et al. (2006). For the refractive index a wide range is modeled, i.e. a real part m_r between 1.5 and 1.6 and an imaginary part m_i between 0 and 0.01. These values are expected to cover the uncertainty about the refractive index of ash at $\lambda = 1020 \text{ nm}$ (e.g., Patterson et al., 1983). The size distributions of the ash layer particles are defined by their effective radius and their form. To cover the uncertainty, they include six cross-section-equivalent effective radii r_{eff} and four forms (SD#1–SD#4); they are shown for $r_{\text{eff}} = 1 \mu\text{m}$ as volume distributions $dV(r)/d\ln r$ in Fig. 3.17. The forms include a narrow mono-modal distribution ($\sigma = 1.8$; SD#1), a wide mono-modal case ($\sigma = 2.4$; SD#2), and two bi-modal distributions (SD#3 and SD#4). Both modes in the bi-modal size distributions have equal cross-sectional area, but different volume. The modal radii r_0 of the size distributions follow from given effective radii and the forms of the size distribution. In total, 24 size distributions for the ash are considered by the retrieval. These quite different forms of size distributions and r_{eff} are expected to cover the range of realistic size distributions for ash particles. SD#1 is considered as the lower limit with respect to the width of the size distribution because volcanic ash particles typically have a wide range of sizes (e.g., Mather et al., 2003; Schumann et al., 2011). In all simulations, particles up to $r = 40 \mu\text{m}$ are accounted for.

Finally, the vertical profile of the extinction coefficient α_{ext} of the aerosols has to be defined for the radiative transfer calculations. The high-resolution profiles from the lidar measurements of 17 April 2010 (shown in Sect. 4.2) are not applied, but height-independent extinction coefficients α_{ext} in each of the two aerosol layers are assumed. The α_{ext} were calculated from the optical depths and the vertical extents of the layers, as known from the

lidar measurements at 1064 nm. 0.07 was found for the optical depth of the lower layer and 0.27 for the ash layer. An uncertainty of 20% was assumed, thus one case with an optical depth of 0.056 for the lower layer and 0.324 for the ash layer and another case with 0.084 for the lower layer and 0.216 for the ash layer is considered. As a result, radiative transfer calculations with a total of 12 288 parameter-combinations are performed. For modeling sky radiances, the Monte Carlo code MYSTIC (Mayer, 2009; Buras and Mayer, 2011) of the software package libRadtran (Mayer and Kylling, 2005) is used.

3.4.2.2. Retrieval approach

A ratio of radiances at two scattering angles and $\lambda = 1020$ nm is used for the retrieval. The largest wavelength of the CIMEL is best suited for this retrieval because it is less affected by the boundary layer aerosol than shorter wavelengths. The basic idea is to calculate the ratio of sky radiances for the different aerosol setups which cover the uncertainties about aerosol properties; the modeled ratios are compared to the ratio from the measurements. If they agree, a solution for r_{eff} and η of the ash particles that is consistent with the photometer data is found. Because of the coarse sampling of the r_{eff} , linear interpolation between sampled r_{eff} is applied for the retrieval of the compatible ranges of r_{eff} and η .

3.4.3. Combined retrieval from lidar and photometer observations

The approach described here was applied to collocated lidar and Sun photometer observations of desert dust aerosols during the SAMUM field campaigns (Heintzenberg, 2009; Ansmann et al., 2011a). Measurements of the HSRL of the German Aerospace Center (S at 532 nm, δ_1 at 532 nm and 1064 nm), measurements of BERTHA (δ_1 at 710 nm), and measurements of MULIS and POLIS (S and δ_1 at 355 nm and 532 nm) were considered. Also, the spectral variabilities of the extinction coefficient α_{ext} and the backscatter coefficient β , expressed by the Ångström exponents κ_{ext} and κ_{bsc} , were considered. Sky radiances in the solar aureole and κ_{ext} from CIMEL observations (CIMEL of Leibniz Institute for Tropospheric Research, Leipzig in SAMUM-1 and CIMEL of NASA in SAMUM-2) (Holben et al., 1998; Müller et al., 2010a), as well as κ_{ext} of the Sun photometer SSARA of the Meteorological Institute of the LMU Munich (Toledano et al., 2009; Toledano et al., 2011) served as additional input parameters for this retrieval. The results from the application of this retrieval to SAMUM observations from three days are presented in Sect. 4.3.

3.4.3.1. Model setup

The aerosol ensembles of the sensitivity study, described in Sect. 3.3.2.1, are used for this retrieval type. For modeling sky radiances, the radiative transfer code *c.disort* (Buras et al., 2011), which is included in the libRadtran software package (Mayer and Kylling, 2005), is employed. For each measurement case, the geometrical setup of the CIMEL measurement (sun zenith angle, pointing directions) is adapted. The aerosol ensembles, as

given in Tab. 3.3, are in a single layer; their aerosol optical depths are set to the values from the AERONET retrievals which use the CIMEL observations as input.

3.4.3.2. Retrieval approach

The modeled properties of each aerosol ensemble are compared to the backscatter observations, as well as to extinction and aureole observations. The ensembles that agree with all observed optical properties are the solutions of the retrieval. Due to the limited number of modeled aerosol ensembles (Tab. 3.3) and an the comparatively large number of observed parameters (compared to the retrievals for lidar or photometer alone), in some cases linear interpolation of model parameters is required for agreement. For a rigorous retrieval, random sampling of model parameters is required, which however would be beyond the current capabilities because of high computational requirements of radiative transfer calculations.

4. Results

This chapter shows the results from the different retrievals (described in Sect. 3.4) that were applied to remote sensing observations of transported volcanic ash from Iceland over Southern Germany and to observations of Saharan dust aerosols at different distances from the source regions.

From the lidar observations of ash, in principle, all microphysical properties were retrieved using the approach described in Sect. 3.4.1, but the focus in this study is on the mass concentration M of the ash particles because of its relevance for flight safety. From aureole observations, the size and the mass-extinction conversion factor η (Eq. 2.38) of the ash particles were retrieved using the approach described in Sect. 3.4.2; using the retrieved η and the extinction coefficients α_{ext} from lidar, the ash mass concentration M was calculated. Finally, microphysical properties of Saharan dust aerosols were retrieved from collocated lidar and photometer observations using the approach described in Sect. 3.4.3.

4.1. Ash properties from lidar retrieval

An eruption of the Eyjafjallajökull volcano (63.63° N, 19.61° W) started on 20 March 2010 (Gertisser, 2010). The first phase was characterized by an effusive eruption that produced lava flows on the ground and only minor emissions into the atmosphere. On 14 April an explosive eruption of the volcano started. It started beneath a glacier, which intensified its explosivity because water vapor was produced by the interaction of hot volcanic material with ice. The ash plumes reached heights of about 8 km, thus mainly stayed within the troposphere. The explosive eruption continued with varying intensity for over one month.

The wind field advected volcanic ash to parts of Central Europe. Volcanic ash reached northern Germany in the night from 15 to 16 April (Flentje et al., 2010; Ansmann et al., 2010) and first traces of ash over Maisach (southern Germany, 48.21° N, 11.26° E, 515 m a.s.l.) were detected by MULIS at about 17:00 UTC on 16 April between 5 km and 7 km above ground. The temporal development of the range-corrected lidar signal of MULIS, within a timeframe of 24 h starting with the arrival of the ash, is shown in Fig. 4.1. After its arrival over Maisach, the ash layer descended, and was in about 2.0 km to 2.4 km between 06:00 UTC and 09:00 UTC on 17 April, when the maximum of the ash layer over Maisach, in terms of backscatter coefficient, was observed. The ash layer was separated from the boundary layer aerosols until the afternoon of 17 April, when mixing of both aerosol types was observed. The temporal development of the volcanic ash plumes over Maisach is discussed in detail by Groß et al. (2010).

Backward trajectories (Draxler and Rolph, 2010) for the ash plume over Maisach in the

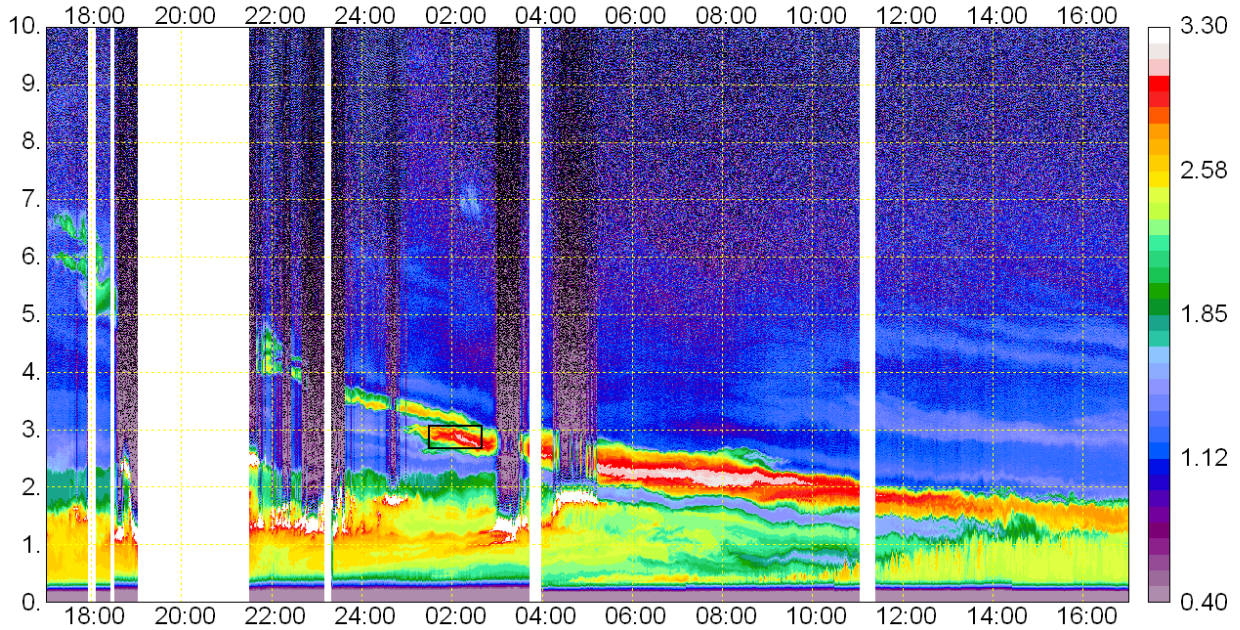


Figure 4.1.: Logarithm of range-corrected signal of MULIS at $\lambda = 1064 \text{ nm}$ over Maisach from 16 April 2010 17:00 UTC to 17 April 2010 17:00 UTC and from 0 to 10 km above ground; white areas denote periods without measurements; black rectangle shows portion of ash plume used for the retrieval.

morning of 17 April (not shown) indicated that the transport of the ash from the volcano to the measurement site took approximately 45 to 50 h. Radiosondes of the German Weather Service (DWD) measured relative humidities in the ash layer in the range from 16 % to 41 % at 00:00 UTC and 12:00 UTC over Oberschleißheim (approx. 22 km east of Maisach), indicating that the particles in the observed layer were dry.

Range-resolved measurements of aerosol properties were performed at Maisach with two lidar systems: MULIS and POLIS (Sect. 2.6.1.3). The retrieval was applied to observations around 2 UTC on 17 April 2010. To increase the signal-to-noise ratio, temporal averages from 1:30 UTC to 2:40 UTC were considered (black rectangle in Fig. 4.1). Observations around 2 UTC were selected for the retrieval because Raman observations of the dense ash layer were only possible at this time; starting at about 4 UTC, no Raman observations were possible because of disturbances of Raman signals due to sunlight. As input for the retrieval, optical parameters of the ash particles averaged over a layer of 400 m vertical extent were used, centered at the maximum of the backscatter coefficient β at 2.88 km above ground. The characterization of the optical properties of the ash particles is discussed by Groß et al. (2010).

The optical data of the ash layer at about 02:00 UTC and their uncertainties are summarized in Tab. 4.1. As it was assumed that the true optical properties of the aerosol particles can be anywhere within the uncertainty ranges, the total uncertainty was assumed to be

parameter	value	relative uncertainty
α_{355}	0.348 km^{-1}	$\pm 7.4\%$
α_{532}	0.371 km^{-1}	$\pm 11.1\%$
β_{355}	$0.00604 \text{ km}^{-1} \text{ sr}^{-1}$	$\pm 5.3\%$
β_{532}	$0.00755 \text{ km}^{-1} \text{ sr}^{-1}$	$\pm 4.1\%$
β_{1064}	$0.00583 \text{ km}^{-1} \text{ sr}^{-1}$	$\pm 16\%$
$\delta_{1,355}$	0.355	$\pm 4.4\%$
$\delta_{1,532}$	0.373	$\pm 2.0\%$

Table 4.1.: Lidar-derived optical properties of volcanic ash plume at about 02:00 UTC on 17 April 2010 (black rectangle in Fig. 4.1); uncertainty (Δ_y of Sect. 3.4.1) is the sum of systematic and stochastic uncertainty (see text).

the sum of stochastic and systematic uncertainty (Groß et al., 2010). Table 3.9 shows the ranges of microphysical parameters of the aerosol ensembles that were considered for the Monte Carlo sampling of the model parameters. Thus, the data in Tabs. 3.9 (ranges of model parameters) and 4.1 (optical parameters from lidar) served as input for the retrieval. It was assumed that the density of volcanic ash and mineral dust particles are equal because both aerosol types consist of solid material from the Earth. Thus, for the mass density ρ of the ash particles, 2.6 g cm^{-3} was assumed, which is given in the OPAC database (Hess et al., 1998) for mineral dust aerosols.

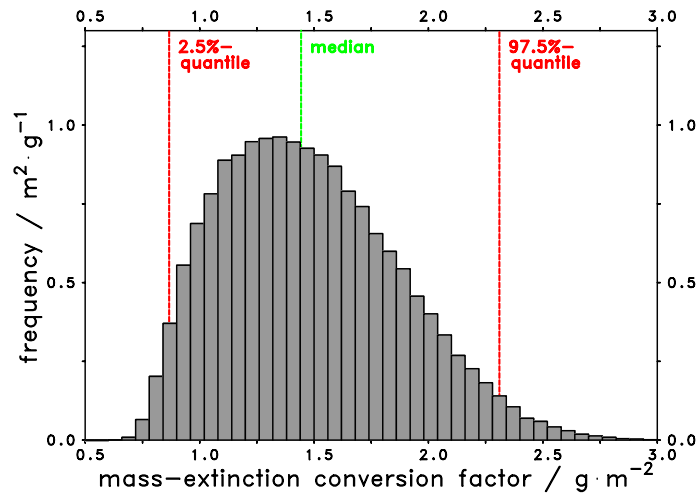


Figure 4.2.: Frequency distribution of solutions of retrieval from lidar measurements for mass-extinction conversion factor η at $\lambda = 532 \text{ nm}$ of volcanic ash over Maisach on 17 April 2010 at 02:00 UTC.

The most relevant result of the retrieval for the intensive ash properties with regard to flight safety was the mass-extinction conversion factor η . The result for the frequency

distribution of η of the ash particles at $\lambda = 532$ nm is shown in Fig. 4.2. 100 000 aerosol ensembles that agree with the observations were evaluated. A median mass-extinction conversion factor $\eta = 1.45$ g m⁻² (green line) was found. 95 % of the compatible ensembles were in the range (0.87 · 2.32 g m⁻²) (red lines). Using these η and the observed extinction coefficient α_{ext} , a mass concentration $M = 0.54$ mg m⁻³ (0.33 · 0.87 mg m⁻³) was found for around 2:00 UTC, when α_{ext} at $\lambda = 532$ nm was 0.371 km⁻¹.

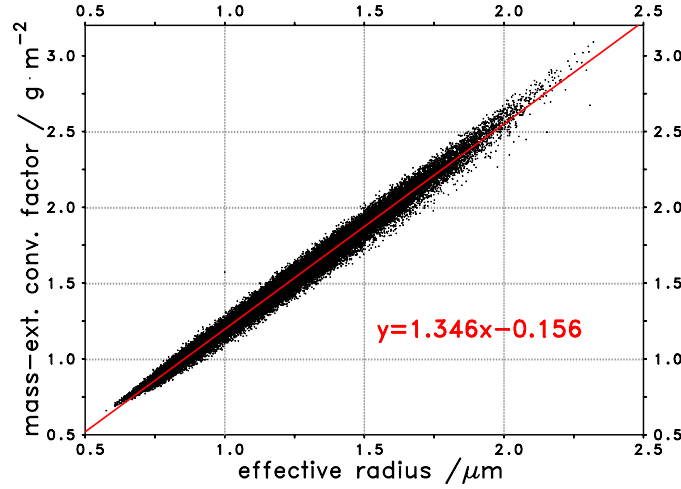


Figure 4.3.: Solutions of retrieval from lidar measurements for mass-extinction conversion factor η at $\lambda = 532$ nm and cross-section-equivalent effective radius r_{eff} ; red: least squares fit of a straight line.

According to Eq. 2.40, the mass-extinction conversion factor η depends on the cross-section-equivalent effective radius r_{eff} of the ash particles. To illustrate this relationship, Fig. 4.3 shows a scatter plot of η over r_{eff} of the solutions of the retrieval. η and r_{eff} are correlated, demonstrating that the uncertainty of η is determined by the uncertainty of r_{eff} . The relationship between η at $\lambda = 532$ nm and r_{eff} is well approximated by the linear regression $\eta = 1.346$ g m⁻² μm^{-1} $r_{\text{eff}} - 0.156$ g m⁻² (standard deviation 0.042 g m⁻²). From the lidar retrieval, a cross-section-equivalent effective radius $r_{\text{eff}} = 1.19$ μm (0.76 · 1.83 μm), a radius conversion factor $\overline{\xi_{\text{vc}}^3} = 0.87$ (0.82 · 0.91), and an ensemble-averaged extinction efficiency $\overline{q_{\text{ext}}} = 2.48$ (2.37 · 2.68) at $\lambda = 532$ nm was found.

The lidar measurements suggest that there was no change of intensive properties of the ash particles from 02:00 to 08:00 UTC (Groß et al., 2011). The intensive properties found for 02:00 UTC were also applied at 08:00 UTC, when no Raman measurements were available. At that time, the maximum of the ash-related extinction coefficient α_{ext} with values around 0.75 km⁻¹ (Fig. 4.4) was observed in about 2.2 km, averaged over one hour and 80 m in the vertical. This corresponds to a maximum mass concentration M of 1.1 mg m⁻³ (0.65 · 1.8 mg m⁻³) for the ash plume over Maisach. If the optical depth of the ash layer $\tau = 0.34$ at $\lambda = 532$ nm (vertical integral of α_{ext} from 1.7 km to 2.7 km above ground) is considered, the ash load, i.e. the vertical integral of M , over Maisach was

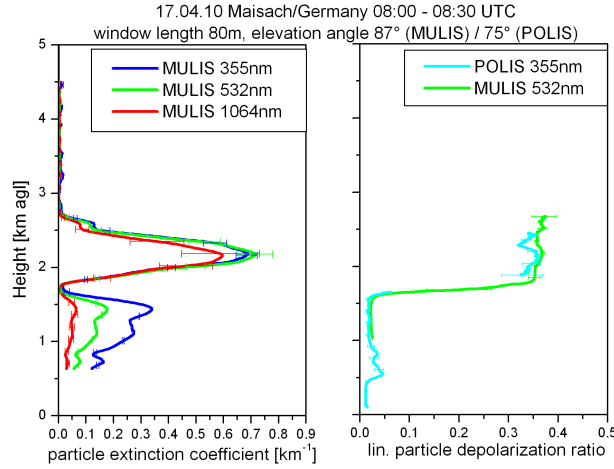


Figure 4.4.: Vertical profile of aerosol extinction coefficients α_{ext} and linear depolarization ratios δ_1 averaged from 8:00 UTC to 8:30 UTC on 17 April 2010; boundary layer aerosols from ground to 1.7 km, volcanic ash from 1.7 km to 2.7 km; error bars indicate systematic error.

0.5 g m^{-2} ($0.3 \dots 0.8 \text{ g m}^{-2}$).

4.2. Ash properties from photometer retrieval

An automatic CIMEL CE-318 Sun photometer is installed on the roof of the Meteorological Institute of the Ludwig-Maximilians-Universität in downtown Munich (48.15° N , 11.57° E , 539 m a.s.l.); the horizontal distance from the lidars in Maisach is 25 km . The approach described in Sect. 3.4.2 was applied on principle-plane observations of this photometer from 17 April 2010 at 08:22 UTC to retrieve properties of the particles in the elevated ash layer. The ratio of sky radiances L at scattering angles of 4° and 3° and $\lambda = 1020 \text{ nm}$ was considered. Henceforward the ratio $L(4^\circ)/L(3^\circ)$ is referred to as Λ . The solar zenith angle was 51.8° . From the CIMEL measurements $\Lambda = L(4^\circ)/L(3^\circ) = 0.856$ at $\lambda = 1020 \text{ nm}$ was found. An uncertainty of ± 0.007 was assumed for Λ which corresponds to an uncertainty of $\pm 0.05^\circ$ for the angular distance between the $L(3^\circ)$ - and the $L(4^\circ)$ -measurement. 0.05° is given by Holben et al. (1998) as the pointing precision of the photometer. For the retrieval, the pronounced two layer structure with the planetary boundary layer (below 1.7 km) and the elevated ash layer (from 1.7 km to 2.7 km) as known from MULIS measurements in Maisach around 8:00 UTC (Fig. 4.4) was considered.

Next to the CIMEL, a JenOptik CHM15kx ceilometer is continuously monitoring the vertical aerosol distribution at $\lambda = 1064 \text{ nm}$ over Munich (Wiegner, 2010). Measurements of the ceilometer (Wiegner, 2010) and MULIS in Maisach (Fig. 4.1) revealed very similar vertical and temporal distributions of the aerosol layers over both sites in the morning of 17 April 2010. Thus, it was assumed that the same ash type, in terms of intensive properties (e.g., η or r_{eff}), was present over both sites, so that it is justified to compare

retrieval results from the photometer in Munich to results from lidar in Maisach.

In Fig. 4.5 simulated Λ are plotted over the effective radius r_{eff} of the ash. The results of all radiative transfer simulations in comparison to the measurement (horizontal lines) are shown. The colors are explained in the figure caption and indicate the different size distributions (SD#1 to SD#4) as defined in Tab. 3.10 and Fig. 3.17. Grey points denote spherical particles, for comparison. For each of the four SD, the r_{eff} -dependent averages of Λ over all combinations of the other model parameters (m_r , m_i , shape, α , boundary layer properties) are connected by dashed lines of same colors. Black dotted lines show the resulting uncertainty range from all simulations with non-spherical ash particles.

The upper panel of Fig. 4.5 shows that Λ decreases with r_{eff} of the ash particles. For SD#1 (red color), e.g., $0.932 \leq \Lambda \leq 0.944$ with an average of $\Lambda = 0.937$ was found, when $r_{\text{eff}} = 0.8 \mu\text{m}$, but only $0.680 \leq \Lambda \leq 0.711$ for $r_{\text{eff}} = 3.0 \mu\text{m}$. For the other SDs, Λ was smaller for same r_{eff} , in particular, if bi-modal size distributions were considered (blue and brown color). The sensitivity of Λ to changes of the form of the particle size distribution was typically of the order of 0.1 (compare SD#1 to SD#4). For a given size distribution of the ash particles, the sensitivity of Λ to changes of the other aerosol properties was quite low. In the hypothetical case of spherical ash particles (grey color), Λ was only slightly larger than in the cases with non-spherical ash. Agreement of the modeled and measured Λ was found for $0.75 \mu\text{m} \leq r_{\text{eff}} \leq 1.7 \mu\text{m}$. These findings are in good agreement with the results from the retrieval based on the lidar measurements, as shown in Fig. 4.3.

The same simulations as shown in the upper panel are shown in the lower panel of Fig. 4.5, however, plotted over $r_{\text{eff}}^* = \overline{\xi_{\text{vc}}^3} r_{\text{eff}}$ (Sect. 2.4). As a consequence, each bar from the upper panel of Fig. 4.5 splits into four bars according to spheres, shape B, shape D, and shape F. In case of spherical particles, $\overline{\xi_{\text{vc}}^3}$ is 1 and $r_{\text{eff}}^* = r_{\text{eff}}$. In case of non-spherical particles, $\overline{\xi_{\text{vc}}^3}$ is smaller than 1 and $r_{\text{eff}}^* < r_{\text{eff}}$. For example, in case of shape D and $r_{\text{eff}} = 1 \mu\text{m}$, r_{eff}^* is only $0.66 \mu\text{m}$.

In Fig. 4.6, Λ is plotted as a function of the mass-extinction conversion factor η at $\lambda = 532 \text{ nm}$. As a consequence of Eq. 2.40, compared to the lower panel of Fig. 4.5 also the extinction efficiency $\overline{q_{\text{ext}}}$ becomes relevant. However, $\overline{q_{\text{ext}}}$ introduces weaker variability on η than the particle shape. For example, $r_{\text{eff}} = 2.0 \mu\text{m}$ and SD#1 ($\Lambda \approx 0.80$, red bar in Fig. 4.5) η was 2.52 g m^{-2} , $\eta = 2.16 \text{ g m}^{-2}$, or $\eta = 2.19 \text{ g m}^{-2}$, depending on whether particle shape B, D, or F was assumed; in case of spherical ash, the conversion factor was considerably larger with $\eta = 3.02 \text{ g m}^{-2}$ (grey bar). For mass-extinction conversion factors η between 0.9 g m^{-2} and 2.0 g m^{-2} agreement between simulated and measured Λ was found, as can be seen from the black dotted lines in Fig. 4.6. This range is in good agreement with the values retrieved from the lidar data for the same ash plume. For comparison, if spherical ash particles were assumed, the range of η was found to be from 1.2 g m^{-2} to 2.5 g m^{-2} (derived from the envelope of all results for spherical particles, grey bars).

Table 4.2 shows the effective radii r_{eff} that were consistent with the CIMEL measurement for the different size distributions (SD#1 to SD#4). The r_{eff} were derived from the upper panel of Fig. 4.5 as the intercepts of the dotted lines with the measured Λ -value (horizontal line). It can be seen that the effective radii r_{eff} that were in agreement with the radiance measurements depended on the size distribution SD; larger r_{eff} were necessary for narrow

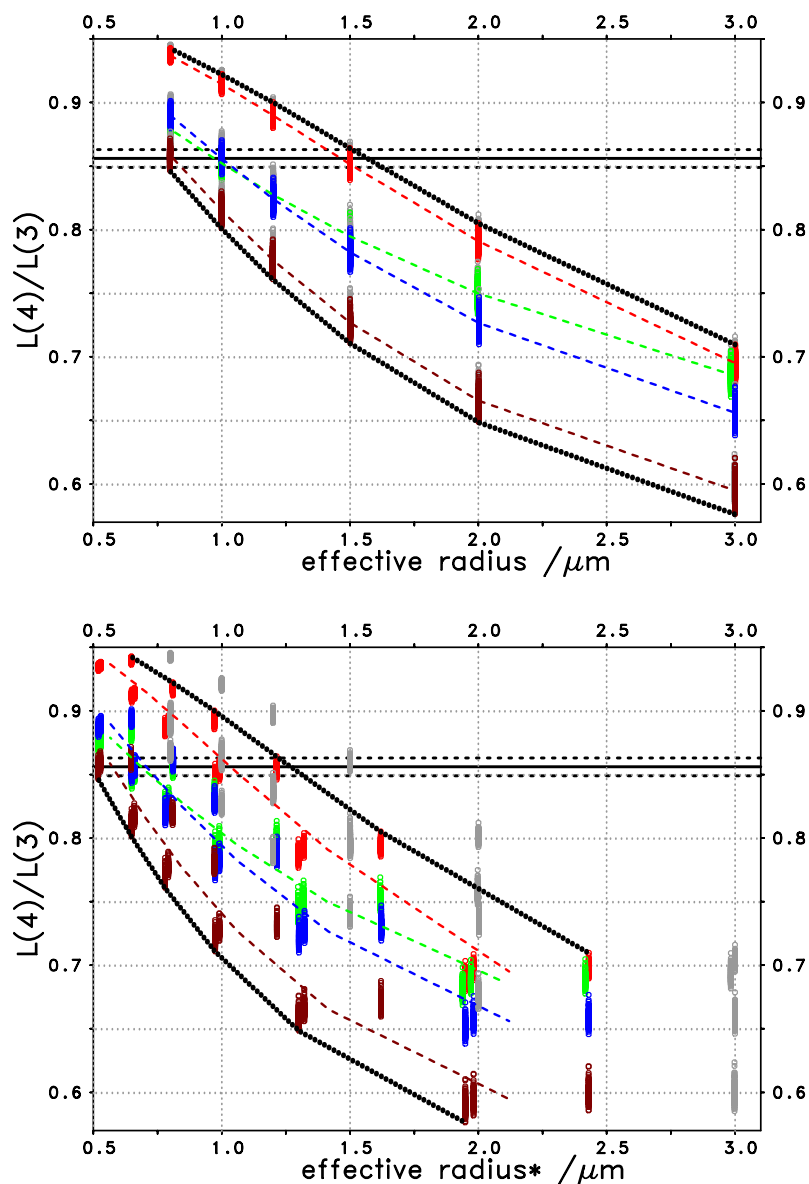


Figure 4.5.: Simulated ratios of aureole radiances $\Lambda = L(4^\circ)/L(3^\circ)$ at $\lambda = 1020$ nm over effective radius r_{eff} of ash particles; averages for different r_{eff} , but same SD are connected by dashed lines; red, green, blue, brown: non-spherical ash with SD#1 to SD#4; grey: spherical ash; black dotted: uncertainty range from simulations with non-spherical ash; horizontal lines: CIMEL measurement with uncertainty; upper panel: r_{eff} according to Eq. 2.30; lower panel: $r_{\text{eff}}^* = 3V^*/4A^* = \overline{\xi_{\text{vc}}^3} r_{\text{eff}}$.

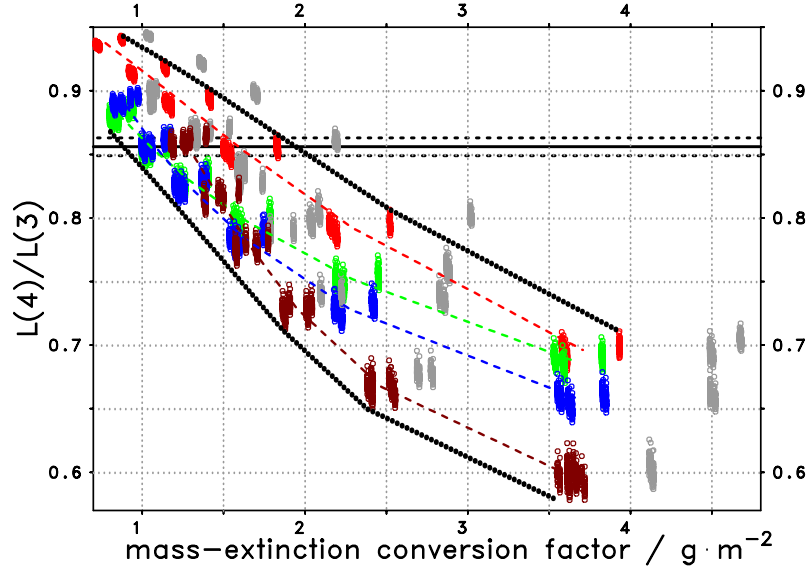


Figure 4.6.: Simulated ratios of aureole radiances $\Lambda = L(4^\circ)/L(3^\circ)$ at $\lambda = 1020$ nm over mass-extinction conversion factor η of ash particles at $\lambda = 532$ nm; red, green, blue, brown: non-spherical ash with SD#1 to SD#4; grey: spherical ash; black dotted: uncertainty range from simulations with non-spherical ash; horizontal lines: CIMEL measurement with uncertainty.

SD	r_{eff}	relative volume in particles with		
		$r > 2.5 \mu\text{m}$	$r > 5 \mu\text{m}$	$r > 10 \mu\text{m}$
#1	$1.47 \mu\text{m}$	27 %	3.7 %	0.1 %
#2	$0.98 \mu\text{m}$	26 %	7.7 %	1.3 %
#3	$1.01 \mu\text{m}$	26 %	4.2 %	0.2 %
#4	$0.82 \mu\text{m}$	25 %	3.5 %	0.1 %

Table 4.2.: Relative volume in particles larger than specific cross-section-equivalent radii; effective radius r_{eff} is extracted from Fig. 4.5 (see text for details).

size distributions (SD#1) than for wide size distributions (e.g. SD#2). For the compatible r_{eff} , Tab. 4.2 also shows the relative volume in particles with radii larger than certain radii. The volume in particles with $r > 2.5 \mu\text{m}$ was approximately 25 % of the total volume, nearly independent of the assumed size distribution. This indicates a strong correlation between Λ and the relative volume in particles with $r > 2.5 \mu\text{m}$. The uncertainty range for the volume in particles with $r > 2.5 \mu\text{m}$, as a result of the uncertainty of the aerosol parameters (Tab. 3.10) and the measurement uncertainty, was from 20 % to 34 %.

4.3. Dust properties from combined lidar and photometer retrieval

This section shows the results from the comparisons of modeled optical properties of complex aerosol ensembles with optical properties from lidar and Sun photometer measurements in desert dust plumes during SAMUM-1 and SAMUM-2. These comparisons were performed in order to find ensembles that explain the measurements. Compared to a rigorous Bayesian retrieval, e.g. like the one applied in Sect. 4.1, this retrieval approach is not as systematic, which means that only a subset of all possible solutions was found. Three case studies were performed (19 May 2006, 4 June 2006, 29 January 2008). In Sect. 3.3.2, the microphysical properties of the model ensembles were described and the sensitivity of their optical properties was investigated. For modeling the lidar ratio S and the linear depolarization ratio δ_1 of ensembles of irregularly-shaped particles, size independence of the backscattering properties for $x > 20.8$ was assumed ($\mathcal{X}_{\text{size-indep.}}$, Sect. 3.3.2.1).

In addition to this retrieval, closure studies were performed using dust size distributions from in-situ optical particle counters operated onboard the Falcon aircraft of the German Aerospace Center (Weinzierl et al., 2009; Weinzierl et al., 2011) and size distributions that were inverted from CIMEL measurements by AERONET (Dubovik et al., 2006); the size distributions from the Falcon were adopted as cross-section-equivalent sizes, the AERONET size distributions were converted from volume-equivalent sizes to cross-section-equivalent sizes (assuming AERONET particle shape distribution, Dubovik et al. (2006)), and parameterized as four-modal size distributions. Large differences between size distributions from in-situ measurements and AERONET inversions were found for the dust plume on 19 May 2006, as demonstrated by Müller et al. (2010b).

4.3.1. 19 May 2006 (SAMUM-1)

A desert dust aerosol layer was present over Ouarzazate (30.93° N, 6.90° W, 1133 m a.s.l.), Morocco, on 19 May 2006 from ground to about 5 km above sea level. Lidar- and in-situ measurements showed that the layer was well-mixed in the vertical (Müller et al., 2010a,b). Heights above the dust layer were virtually aerosol-free, thus the vertical aerosol column was dominated by the dust layer. Lidar- and Sun photometer measurements showed that the aerosol properties remained stable during the day.

4.3.1.1. Lidar observations

In Fig. 4.7 lidar ratios S and linear depolarization ratios δ_1 of the reference ensemble (Sect. 3.3.2.2) are compared with data derived from the lidar measurements of 19 May 2006. $S = 50 \pm 5$ sr at 532 nm was derived from HSRL measurements at 11:09 UTC during an overflight of the Falcon aircraft over Ouarzazate (Esselborn et al., 2009). S of the reference ensemble, which is 48 sr at 532 nm, is in good agreement with this measurement. Tesche et al. (2009) suggested that S of mineral dust aerosols, observed during SAMUM-1, did not show distinct wavelength dependence. The lidar ratio S of the reference ensemble

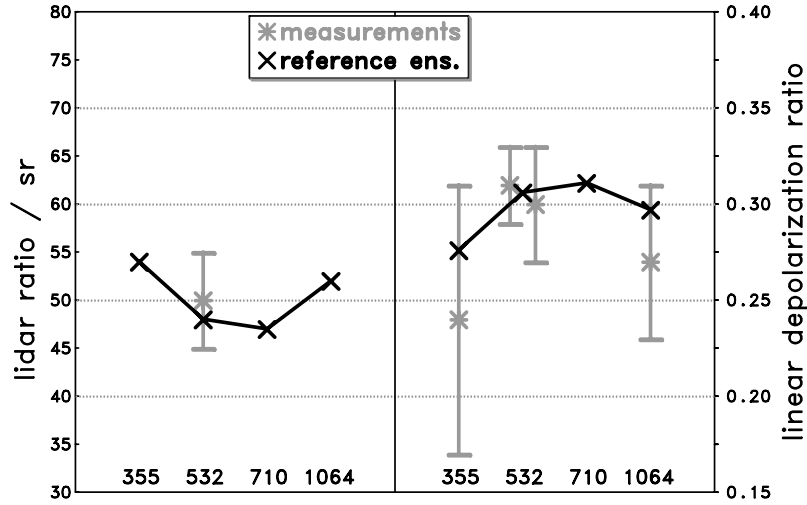


Figure 4.7.: Comparison of lidar-relevant optical properties of reference ensemble with optical properties from lidar measurements at different wavelengths in nm on 19 May 2006 (SAMUM-1).

(mixture of absorbing and non-absorbing irregularly-shaped particles, see Sect. 3.3.2.2) is in agreement with these observations because it is also only weakly wavelength-dependent: it decreases by 6 sr (approx. 10 %) from 355 nm to 532 nm, and increases by 5 sr from 710 nm to 1064 nm. The lidar ratios S for $\mathcal{A}1$ and $\mathcal{A}5$ (see Tab. 3.7) are too small for an agreement with measurements. This suggests that the amount of particles with low aspect ratio ϵ' has to be small for agreement with observed S .

Neglecting their uncertainties, the lidar measurements of 19 May 2006 suggested an increase of the linear depolarization ratio δ_1 from 355 nm to 532 nm, and a slight decrease of δ_1 from 532 nm to 1064 nm (Fig. 4.7). For the reference ensemble the same spectral feature was found. The linear depolarization ratio $\delta_1 = 0.275$ of the reference ensemble at 355 nm is slightly higher than the value derived from the POLIS measurement (0.24), but it is well within the uncertainty range of POLIS (0.17 to 0.31). At 532 nm good agreement of the reference ensemble (0.306) with the values derived from the measurements (MULIS: 0.31; HSRL: 0.30) was found. $\delta_1 = 0.298$ of the reference ensemble at 1064 nm is also within the uncertainty range of the δ_1 derived from HSRL (0.23 to 0.31). Note, that the uncertainties of the lidar measurements do not exclude a wavelength-independent δ_1 close to 0.3 (see Fig. 4.7).

Furthermore, the modeled spectral dependence of the backscattering, expressed by the Ångström exponent for backscatter κ_{bsc} , were compared with data from lidar. Tesche et al. (2009) found $\kappa_{\text{bsc},355-532}$ of about 0.1 to 0.6 and $\kappa_{\text{bsc},532-1064}$ close to 0.3 from measurements

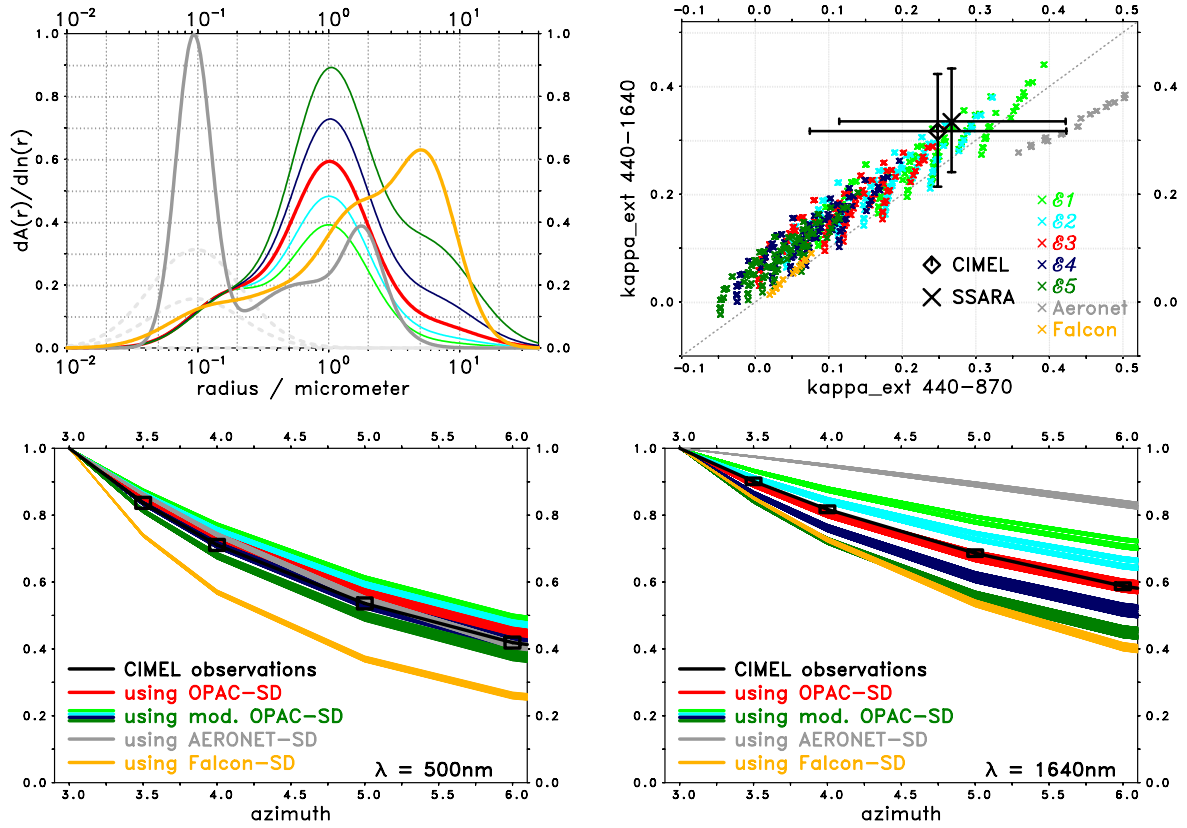


Figure 4.8.: Size distributions (arbitrary scale) from Tab. 3.3, from AERONET retrieval of 8:30 UTC-almucantar scan, and from Falcon measurements between 11 and 12 UTC on 19 May 2006 (upper left); comparison of modeled κ_{ext} with observations of CIMEL and SSARA on 19 May 2006 (upper right); comparison of modeled normalized aureole radiances over azimuth angle at two wavelengths with CIMEL almucantar observations on 19 May 2006 at 8:30 UTC (lower left and right).

of BERTHA. Measurements of POLIS and MULIS indicate $\kappa_{\text{bsc}, 355-532}$ close to 0.0 in the upper part of the dust layer (not shown). For the reference ensemble $\kappa_{\text{bsc}, 355-532} = -0.06$ and $\kappa_{\text{bsc}, 532-1064} = 0.36$ was found, which are in the same range as the values from the measurements.

4.3.1.2. Photometer observations

From the CIMEL measurements at about 8:29 UTC, Ångström exponents for extinction $\kappa_{\text{ext}, 440-870} = 0.25 \pm 0.18$ and $\kappa_{\text{ext}, 440-1640} = 0.32 \pm 0.11$ were derived for the total aerosol column over Ouarzazate ($\tau_{440} = 0.368$). For the calculation of the uncertainty of κ_{ext} , an

uncertainty of ± 0.02 of τ was assumed (Holben et al., 1998). From SSARA observations at about 9:15 UTC, $\kappa_{\text{ext},440-870} = 0.27 \pm 0.16$ and $\kappa_{\text{ext},440-1550} = 0.33 \pm 0.10$ was found. The observed κ_{ext} are well explained by ensembles described in Sect. 3.3.2. For the reference ensemble, $\kappa_{\text{ext},440-870} = 0.222$ and $\kappa_{\text{ext},440-1640} = 0.258$ were found, which are in good agreement with the observations.

To investigate the influence of the size distribution on κ_{ext} , the upper right panel of Fig. 4.8 shows modeled and observed κ_{ext} . The different colors in this figure denote different OPAC size distributions as introduced in Sect. 3.3.2 and the size distributions available from AERONET and Falcon in-situ observations that were used for closure studies. The red, green, and blue crosses cover all cases from Tab. 3.3. As shown in Sect. 3.3.2, a major influencing parameter for κ_{ext} of these cases is the number of WASO particles (\mathcal{F}). For the AERONET (grey) and Falcon (orange) size distributions only parameters \mathcal{A} , \mathcal{B} , \mathcal{C} , and \mathcal{D} , i.e. the shape and the refractive index of the particles were varied. Using the AERONET size distribution, which was inverted by AERONET (Dubovik et al., 2006) from CIMEL almucantar and extinction observations at about 8:30 UTC, modeled $\kappa_{\text{ext},440-870}$ were around the upper end of the uncertainty range of the CIMEL observations. Ensembles with the size distribution from Falcon can not explain the κ_{ext} -observations.

In the lower panels of Fig. 4.8 modeled normalized sky radiances at two wavelengths (500 nm and 1640 nm) are compared to CIMEL observations in the almucantar at about 8:30 UTC. These radiances are normalized by the radiances at azimuth angle 3° . The boxes around the observed normalized radiances illustrate the uncertainty from the 0.05° pointing uncertainty of the CIMEL (Holben et al., 1998). The ratio between scattering angle θ and azimuth angle of the almucantar scan depends on the Sun zenith angle; the zenith angle was 53.5° at 8:30 UTC, thus the ratio is about 0.8 (θ is about 2.4° at azimuth angle 3°). The same cases as in the upper right panel of Fig. 4.8 are considered in the lower panels, that is all cases from Tab. 3.3, as well as the size distributions from Falcon and AERONET with varying particle shapes and refractive index (according to \mathcal{A} , \mathcal{B} , \mathcal{C} , and \mathcal{D}). The normalized aureole radiances are grouped by their size distributions because the radiances are primarily caused by single forward scattering which is primarily sensitive to the coarse mode size distributions (Sect. 3.3.2). The agreement with observations at $\lambda = 500$ nm (lower left of Fig. 4.8) is good for model ensembles with the size distribution from OPAC ($\mathcal{E}3$, red) and from AERONET (grey), but for ensembles with the size distribution from Falcon the decrease of the modeled sky radiance with azimuth angle is notably steeper. At $\lambda = 1640$ nm (lower right), the comparison shows good agreement for the OPAC size distribution (Ref.), thus the reference ensemble agrees with the CIMEL aureole observations at both wavelengths. The angular dependence of the modeled aureole radiances using the size distribution from AERONET is significantly weaker than found from the observation, independent of particle shape or refractive index m ; this indicates too few large particles in the AERONET size distribution; note the differences between the OPAC and the AERONET size distribution, in particular the absence of particles with $r > 5 \mu\text{m}$ in the AERONET size distribution (upper left of Fig. 4.8). The angular dependence of the aureole radiances using the Falcon size distribution is stronger than found from the observations at $\lambda = 1640$ nm, indicating too many large particles. Figure 4.8 (upper left)

shows significantly more particles with $r > 3 \mu\text{m}$ in this size distribution (orange) compared to the OPAC size distribution, for which agreement with the observations was found.

4.3.1.3. Summary

The reference ensemble agrees with all observations of 19 May 2006 from lidar, as well as with κ_{ext} and aureole radiances from Sun photometer. This ensemble is the only ensemble considered in this study that provides a solution of the combined retrieval from lidar and photometer observations of 19 May 2006.

4.3.2. 4 June 2006 (SAMUM-1)

On 4 June 2006 mineral dust aerosols were observed over Ouarzazate in heights up to almost 5 km above sea level. The extinction coefficient α_{ext} , as measured by the HSRL at 9:47 UTC (Esselborn et al., 2009), was height-dependent with maximum values in 3 km a.s.l. The lidar ratio S varied with height, with values close to 42 sr in a layer from about 2.5 to 3.5 km a.s.l., and values close to 50 sr above and below this layer. By contrast, the linear depolarization ratio δ_1 was not height-dependent and airborne in-situ measurements did not show significant height dependence of the size distribution (Weinzierl et al., 2009).

4.3.2.1. Lidar observations

In Fig. 4.9, lidar ratios S of the reference ensemble, of an ensemble including particles with low aspect ratios ϵ' ($\mathcal{A}1$), and an ensemble with an increased real part of the refractive index m_r ($\mathcal{B}3$) are compared with lidar measurements of the aerosol in heights of 2.5 to 3.5 km a.s.l. The reference ensemble (48 sr) can not reproduce the lidar ratio S derived from the HSRL (40 sr to 45 sr at 532 nm). The S of $\mathcal{A}1$, where low ϵ' are included, is only 36 sr, which is lower than the S derived from the HSRL; however, the S of a mixture of $\mathcal{A}1$ and the reference ensemble, that is a mixture of $\mathcal{A}1$ and $\mathcal{A}2$, agrees with the HSRL observations (not shown). An increase of m_r of the dust particles from $m_r = 1.53$ (Ref.) to $m_r = 1.58$ ($\mathcal{B}3$) decreases S at 532 nm from 48 sr to 42 sr, resulting in good agreement with the S derived from the HSRL. Another potential explanation for the comparatively low lidar ratios in this dust layer could be weaker absorption by the dust particles compared to the dust on 19 May (not explicitly calculated here).

Linear depolarization ratios δ_1 derived from measurements are available at 532 nm and 710 nm for 4 June 2006 (Fig. 4.9 right). $\delta_1 = 0.306$ of the reference ensemble at 532 nm is in good agreement with the HSRL measurement (0.27 to 0.33), but slightly lower than values derived from MULIS (0.32 to 0.36) at the same wavelength. At $\lambda = 710$ nm, $\delta_1 = 0.311$ of the reference ensemble is in agreement with the values derived from BERTHA (0.25 to 0.35). δ_1 of the ensemble $\mathcal{B}3$ (increased m_r) is only slightly lower than δ_1 of the reference ensemble, thus the agreement of both ensembles with the measurements is equally good. For the ensemble including particles with low aspect ratios ϵ' ($\mathcal{A}1$), δ_1 is notably higher than for the reference ensemble ($\delta_1 = 0.349$ vs. 0.306 at 532 nm). The agreement of this

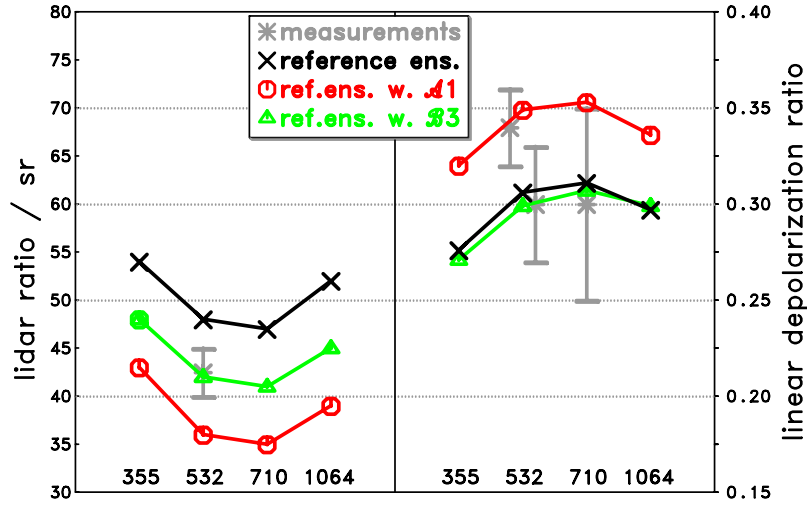


Figure 4.9.: Comparison of lidar-relevant optical properties of reference ensemble and variations of the reference ensemble with optical properties from lidar measurements at different wavelengths in nm on 4 June 2006 (SAMUM-1).

ensemble with the δ_1 at 532 nm from the MULIS measurements is good, but the same parameter from the HSRL is slightly too low for an agreement with this ensemble. At 710 nm, the δ_1 of ensemble A1 (0.353) is close to the upper limit of the uncertainty range of δ_1 derived from BERTHA. A 1:1-mixture of the reference ensemble and ensemble A1 can reproduce the optical properties (S , δ_1) from the lidar measurements of 4 June 2006. In this mixture, shapes A and E have a relative abundance of 0.1, and shapes B, C, D, and F a relative abundance of 0.2.

4.3.2.2. Photometer observations

Ångström exponents $\kappa_{\text{ext},440-870} = 0.14 \pm 0.16$ and $\kappa_{\text{ext},440-1640} = 0.27 \pm 0.10$ were observed by CIMEL at about 7:06 UTC ($\tau_{440} = 0.392$). From simultaneous measurements of SSARA $\kappa_{\text{ext},440-870} = 0.15 \pm 0.16$ and $\kappa_{\text{ext},440-1550} = 0.24 \pm 0.10$ were found. These κ_{ext} are by about 0.1 lower than the κ_{ext} observed on 19 May 2006, but the uncertainty ranges of κ_{ext} from both days are overlapping. The top right panel of Fig. 4.10 shows modeled κ_{ext} in comparison to the observations on 4 June 2006. In this figure, besides the size distributions from Sect. 3.3.2, also the size distribution from AERONET (grey) and Falcon (orange) for 4 June 2006 (shown in top left panel) are considered. The κ_{ext} of many ensembles described in Sect. 3.3.2 were in the same range as the observations. Also the reference ensemble is in agreement with the observations. The ensembles with the size distributions from AERONET and Falcon do not agree with κ_{ext} observed on 4 June, independent of

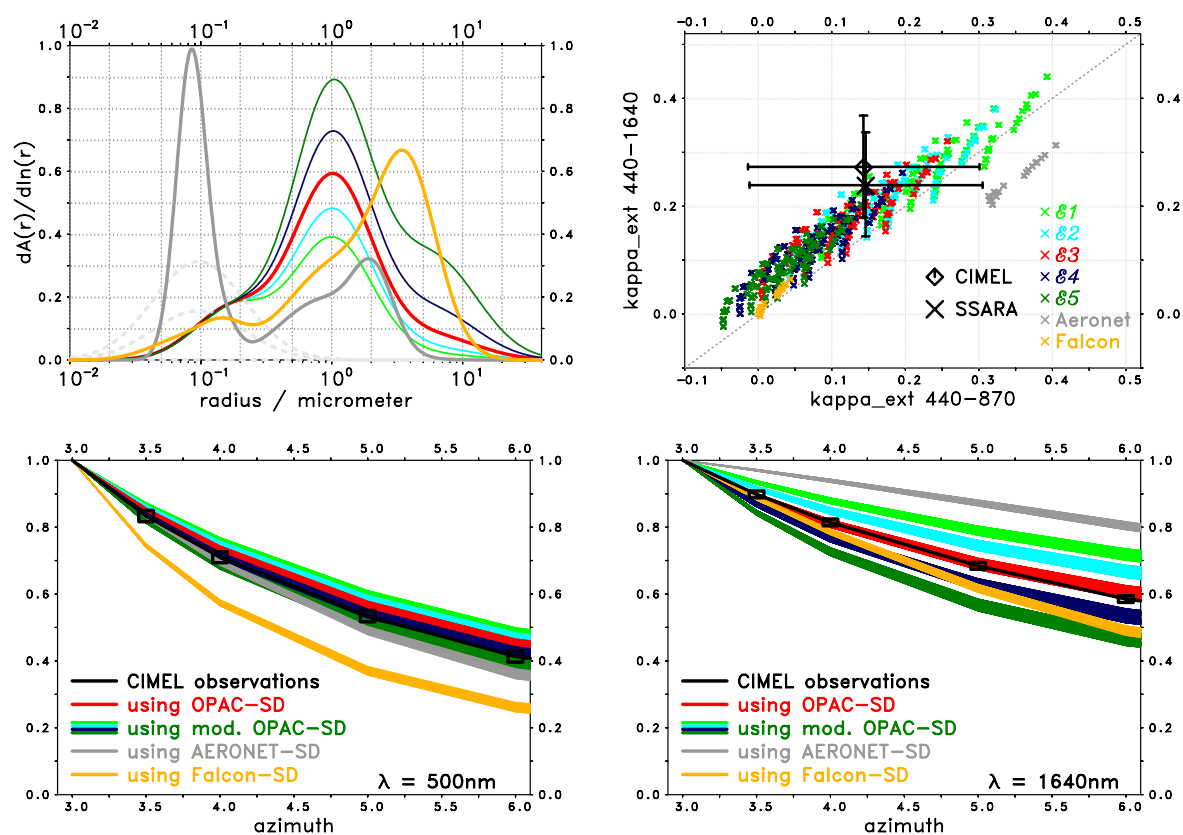


Figure 4.10.: Size distributions (arbitrary scale) from Tab. 3.3, from AERONET retrieval of 7:07 UTC-almucantar scan, and from Falcon measurements between 10:02 UTC to 10:10 UTC on 4 June 2006 (upper left); comparison of modeled κ_{ext} with observations of CIMEL and SSARA on 4 June 2006 (upper right); comparison of modeled normalized aureole radiances over azimuth angle at two wavelengths with CIMEL almucantar observations on 4 June 2006 at 7:07 UTC (lower left and right).

assumed particle shape and refractive index.

The lower panels of Fig. 4.10 compare modeled normalized sky radiances at two wavelengths to CIMEL observations in the almucantar at about 7:07 UTC on 4 June 2006. The Sun zenith angle was 70.0° , thus the ratio between scattering angle θ and azimuth angle is about 0.94. Basically, this comparison shows similar agreements and discrepancies as the comparison for 19 May 2006 (Fig. 4.8): The agreement of normalized radiances using size distributions from OPAC is good at both wavelengths, whereas using the AERONET size distribution gives too weak angular dependence at 1640 nm, and using the Falcon size distribution results in too strong angular dependence, in particular at 500 nm.

4.3.2.3. Summary

An ensemble with an increased number of particles with low aspect ratios (mixture of shape distributions $\mathcal{A}1$ and $\mathcal{A}2$) compared to the reference ensemble provides a solution that agrees with lidar and photometer observations of 4 June 2006.

4.3.3. 29 January 2008 (SAMUM-2)

In the late evening of 29 January 2008, high aerosol extinction coefficients α_{ext} were observed by lidar at the airport of Praia (14.94° N, 23.49° W, 75 m a.s.l.), Cape Verde, during the SAMUM-2 campaign. The mineral dust layer extended up to heights of about 1 km above ground. Above 1 km, only very low amounts of aerosol were detected by lidar (Groß et al., 2011b). Some differences of the linear depolarization ratio δ_1 between the aerosol below and above 0.5 km were observed, probably due to mixing of small amounts of maritime aerosols into the lower layer. Thus, the optical data of the layer from 0.5 km to 0.8 km (δ_1) and 0.6 km to 0.8 km (S , κ_{bsc}) (Groß et al., 2011b) were used for the comparison of lidar observations with optical modeling results.

4.3.3.1. Lidar observations

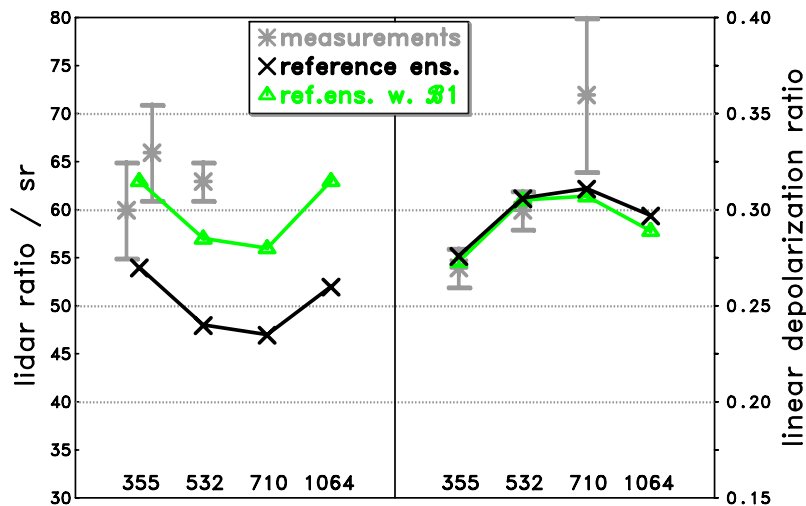


Figure 4.11.: Comparison of optical properties of reference ensemble and variations of the reference ensemble with optical properties from lidar measurements at different wavelengths in nm on 29 January 2008 (SAMUM-2).

Lidar ratios S at 355 nm are available from measurements of POLIS and MULIS; they

were in the range from 60 sr to 66 sr. A lidar ratio S of 63 ± 2 sr at 532 nm was derived from MULIS measurements. These S were higher than the S from the HSRL observations during SAMUM-1 (see above). The lidar ratio S of the reference ensemble is lower than S derived from the measurements (Fig. 4.11). A high lidar ratio S can be explained by a reduced real part of the refractive index m_r . Figure 4.11 shows that S at 355 nm is in good agreement with the measurement for $m_r = 1.48$ (ensemble $\mathcal{B}1$). At 532 nm, however, S of ensemble $\mathcal{B}1$ is still slightly lower (57 sr) than the S derived from the measurement; nonetheless, considering the vertical variability of S within the aerosol layer (± 4 sr, Groß et al., 2011b), the lidar ratio of ensemble $\mathcal{B}1$ is not in contradiction with the observations at 532 nm.

At 355 nm, the linear depolarization ratio of the reference ensemble ($\delta_1 = 0.275$) and of the ensemble with $m_r = 1.48$ ($\mathcal{B}1$, $\delta_1 = 0.272$) are in agreement with the POLIS measurement, which has an uncertainty from $\delta_1 = 0.26$ to 0.28. Likewise, at 532 nm, the agreement is good. The modeled δ_1 at 710 nm (0.311 and 0.309, respectively) are slightly lower than the values derived from BERTHA measurements which, however, were affected by uncertainties due to non-perfect measurement conditions. An increase of δ_1 from 532 nm to 710 nm is a common feature of the models and the measurements, but the increase of δ_1 is smaller in the models than in the measurements.

From the MULIS measurements in the same layer, $\kappa_{\text{bsc},355-532} = -0.15$ with an estimated uncertainty of 0.3 was found (not shown). $\kappa_{\text{bsc},355-532}$ of the reference ensemble (-0.06) and ensemble $\mathcal{B}1$ (0.01) are in good agreement with the observed value from MULIS.

4.3.3.2. Photometer observations

The CIMEL that was deployed during SAMUM-2 in Praia did not include a channel at $\lambda = 1640$ nm. CIMEL observed $\kappa_{\text{ext},440-870} = 0.12 \pm 0.12$ at about 18:23 UTC ($\tau = 0.523$). SSARA simultaneously observed $\kappa_{\text{ext},440-870} = 0.13 \pm 0.12$ and $\kappa_{\text{ext},440-1550} = 0.29 \pm 0.07$. These values are in the same range as the κ_{ext} observed during SAMUM-1. The upper right panels of Fig. 4.12 compares the modeled κ_{ext} with these observations. The size distributions from AERONET retrievals and Falcon in-situ measurements result in κ_{ext} that are lower than observed. The AERONET size distribution of 29 January 2008 (see upper left panel) contains significantly fewer fine mode particles (r around 100 nm) than SAMUM-1-AERONET distributions, which explains the lower κ_{ext} of the AERONET size distributions in SAMUM-2 compared to SAMUM-1. The κ_{ext} of the reference ensemble is within the range of the observed κ_{ext} of 29 January.

The comparison of modeled aureole radiances with CIMEL observations (lower panels of Fig. 4.12) shows significantly better agreement of the size distributions from AERONET and Falcon with the aureole observations, as compared to the SAMUM-1 cases (see above). The OPAC desert size distribution ($\mathcal{E}3$) which is used in the reference ensemble results in normalized aureole radiances that are at the lower margin of the uncertainty of the observations at $\lambda = 440$ nm, whereas at $\lambda = 1020$ nm no agreement was found. Using the size distribution $\mathcal{E}2$, which contains fewer large particles than $\mathcal{E}3$, agreement at both wavelengths was found.

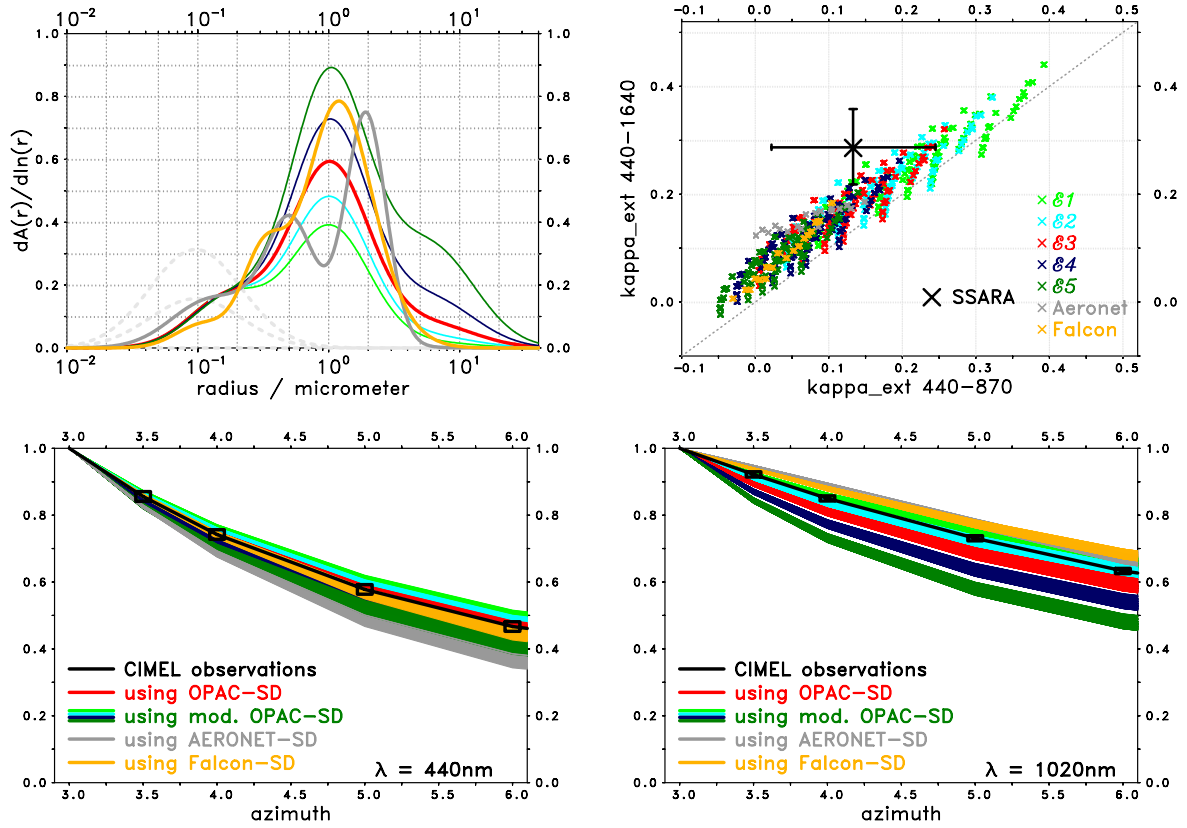


Figure 4.12.: Size distributions (arbitrary scale) from Tab. 3.3, from AERONET inversion of 18:24 UTC-almucantar scan, and from Falcon measurements between 20:35 UTC and 20:38 UTC on 29 January 2008 (upper left); comparison of modeled κ_{ext} with observations of CIMEL and SSARA on 29 January 2008 (upper right); comparison of modeled normalized aureole radiances over azimuth angle at two wavelengths with CIMEL almucantar observations on 29 January 2008 at 18:24 UTC (lower left and right).

4.3.3.3. Summary

An ensemble with a reduced real part of the refractive index m_r (ensemble $\mathcal{B}1$) was found to agree well with the lidar observations. The comparison with photometer observations showed that a reduced number of large particles (ensemble $\mathcal{E}2$) provides agreement with the photometer observations of 29 January 2008. An ensemble with reduced m_r and reduced number of large particles (ensemble $\mathcal{B}1\mathcal{E}2$) provides agreement with the photometer observations and the observed S and κ_{bsc} from lidar, but the linear depolarization ratio is lower than found from lidar observations. By reducing the number of WASO particles (using a 1:1-mixture of ensembles $\mathcal{B}1\mathcal{E}2\mathcal{F}2$ and $\mathcal{B}1\mathcal{E}2\mathcal{F}3$, i.e. 7.5 instead of 10 WASO par-

ticles per dust particles), agreement with all considered observations of 29 January from lidar and photometer was found.

5. Discussion

Microphysical properties of ash and dust aerosols were successfully retrieved from lidar and Sun photometer observations using three types of retrievals. The results from these retrievals are discussed here based on the sensitivities of the observed parameters, which were investigated in Sect. 3.3.

5.1. Ash properties from lidar retrieval

A maximum mass concentration M of 1.1 mg m^{-3} ($0.65 \cdot 1.8 \text{ mg m}^{-3}$) was found by the lidar retrieval for the volcanic ash over Maisach on 17 April 2010. $M = 2.0 \text{ mg m}^{-3}$ is currently considered as the upper limit for “areas of low contamination” (International Civil Aviation Organization, 2011) in which civil flights are typically permitted by the national authorities. In areas with $M > 2.0 \text{ mg m}^{-3}$, flight restrictions are recommended by the International Civil Aviation Organization. The maximum mass concentration M from the lidar retrieval suggests that the upper limit for “areas of low contamination” was not exceeded over Maisach during the volcanic ash event in spring 2010.

The retrieved mass-extinction conversion factor $\eta = 1.45 \text{ g m}^{-2}$ ($0.87 \cdot 2.32 \text{ g m}^{-2}$) is in the same range as the estimate from Ansmann et al. (2010), which was 1.95 g m^{-2} for the younger ash plume over Leipzig, Germany, on 16 April 2010. In their estimate they assumed desert dust size distributions from OPAC (Hess et al., 1998). In a follow-up contribution, Ansmann et al. (2011b) applied a different approach: They used conversion factors of ash retrieved by two different methods, that is the method of O’Neill et al. (2003) and Dubovik et al. (2006). The conversion factors were retrieved for the ash over Leipzig for several days during the volcanic ash event in 2010. The differences between the factors from these methods were in the order of 30 % to 40 %, and on average a mass-extinction conversion factor $\eta = 1.57 \text{ g m}^{-2}$ was found. Also this η is in good agreement with the results from this thesis.

As described in Sect. 3.4.1, several assumptions were applied for the optical modeling of the aerosol ensembles in the context of the lidar retrieval, e.g., assumptions on the spectral variability of the refractive index m , on particle shape, and on the size distribution. These assumptions can potentially bias the results of the retrieval. For example, the retrieved real part of the refractive index m_r was 1.43 ($1.35 \cdot 1.50$), which was smaller than the refractive index typically measured for volcanic ash; for example, Patterson et al. (1983) estimate m_r for ash from the El Chichón volcano to be 1.53. This suggests that the lidar retrieval probably underestimated the real part m_r . Simulations of the sensitivity study in Sect. 3.3 showed that spheroids require a lower m_r than irregularly-shaped particles to provide the

same backscattering and depolarization as irregularly-shaped particles; this explains the underestimation of m_r by the lidar retrieval (in which spheroids were assumed).

Another issue is the physical limitation of the methodology, in particular with respect to the sensitivity for volume in large particles, as investigated in Sect. 3.3. It was shown in Fig. 3.4 that the backscattering cross section per particle volume at $\lambda = 1064$ nm (maximum λ of the considered lidar systems) decreases to only one fifth (20 %) to one half (50 %) when the particle radius increases from $r = 1 \mu\text{m}$ to $r = 3 \mu\text{m}$; this demonstrates that the sensitivity of lidar signals to larger particles is low. The lidar retrieval suggested that most of the particle mass was in particles smaller than $3 \mu\text{m}$; this implies that the retrieved M from lidar could be underestimated, in case many particles with $r > \sim 3 \mu\text{m}$ were present in the plume. The independent retrieval from collocated aureole observations (Sect. 4.2), which are sensitive to particles up to $r \approx 10 \mu\text{m}$, however, confirmed the presence of only a low fraction of particles larger than $3 \mu\text{m}$.

Due to the limited information content of the lidar data, the relative accuracy of the parameters retrieved from lidar is only in the order of ± 50 %. Recently, Veselovskii et al. (2010) developed and applied an approach for the retrieval of dust particle parameters from lidar observations, which uses observed depolarization ratios to separate spherical from non-spherical particles. They apply regularization techniques to retrieve the properties of both components, whereby they assume spheroidal particles with a fixed aspect ratio distribution for the non-spherical particle fraction. They found an relative accuracy of better than 30 % for the effective particle size and particle volume. The difference in relative accuracy of their approach and the approach taken in this thesis can be explained by the difference of the variabilities of the aerosol models. Veselovskii et al. (2010) restricted the variability of particle shapes in their approach by assuming a fixed aspect ratio distribution; as a result of the limited variability of particle shapes, the uncertainty of their approach is lower than the uncertainty of the lidar retrieval developed in this thesis. As a fixed aspect ratio distribution does not take into account the natural variability of aerosol particle shapes, the uncertainty of the approach by Veselovskii et al. (2010) probably does not cover the complete uncertainty imposed by the retrieval problem. Allowing the same variabilities for the microphysical particle properties in both approaches is expected to result in about the same relative uncertainties of the results.

5.2. Ash properties from photometer retrieval

In contrast to the lidar retrieval where a Monte Carlo approach was used, the retrieval from aureole observations did not rigorously explore a range of model parameter values, mainly because of the high computational demand of the required radiative transfer calculations. Instead, only extreme values of each model parameter were considered for the aureole retrieval (Tab. 3.10). These extreme values were the upper and lower bounds of the uncertainty about the model parameters. Thus, the aureole retrieval did not provide statistical results for the model parameters, but only ranges of model parameters that allow for agreement with the aureole observations. In Sect. 4.2, it was found that $0.75 \mu\text{m} \leq r_{\text{eff}} \leq 1.7 \mu\text{m}$

of the ash are required for agreement with the aureole measurements at $\lambda = 1020$ nm; this is in the same range as found from the lidar retrieval.

For the discussion of the physical principles that are relevant for the aureole retrieval, single scattering properties of the ash particles are used, i.e. the ratio of their phase function $\Lambda_{11} = F_{11}(4^\circ)/F_{11}(3^\circ)$, as an approximation for Λ (which was defined as the ratio of sky radiances at 4° and 3° off the Sun in the principle plane). The discussion using Λ_{11} is useful because the radiances in the aureole were dominated by single forward scattering: in all simulations of Sect. 4.2, the condition $|\Lambda - \Lambda_{11}|/\Lambda < 0.1$ was fulfilled at $\lambda = 1020$ nm, which means that the relative difference between Λ and Λ_{11} was always smaller than 10%. E.g., for the simulated Λ that agreed with the measurement (0.856 ± 0.007), the absolute difference $|\Lambda - \Lambda_{11}|$ was always smaller than 0.02. Λ_{11} is used for further discussions.

The dependence of the forward scattering by single particles on their microphysical properties was investigated in Sect. 3.3.1.4. In Fig. 3.6, the size dependence of Λ_{11} was plotted for different particle shapes and refractive indices m . The most remarkable feature is the almost monotonic decrease of Λ_{11} up to size parameter $x \approx 50$, nearly independent of particle shape and m . The decrease of Λ_{11} with increasing x is due to the increase of the height and the decrease of the width of the main diffraction peak with increasing x . At a fixed scattering angle $\theta > 0^\circ$, the flanks of the main peak and the first diffraction minimum come closer with increasing x , until the first diffraction minimum is reached. For example, at $\theta = 4^\circ$ the first diffraction minimum is reached at $x \approx 50$, but $\theta = 3^\circ$ is still within the main diffraction peak at this x . As a consequence, the relative decrease of the phase function F_{11} from $\theta = 3^\circ$ to $\theta = 4^\circ$ is steep and $\Lambda_{11} = F_{11}(4^\circ)/F_{11}(3^\circ)$ is close to zero at size parameter $x \approx 50$.

$\Lambda_{11}(x)$ is concave for $x \lesssim 40$ (Fig. 3.6), thus $\Lambda_{11}(x)$ sharply decreases at large x and the presence of large particles ($x \approx 25$ to 50) reduces the average Λ_{11} of aerosol ensembles considerably. As wide SD contain a larger fraction of large particles than narrow SD with the same r_{eff} and because of the concave shape of $\Lambda_{11}(x)$, wide SD require lower r_{eff} to provide the same Λ as narrow SD; this explains the dependence of the retrieved effective radius r_{eff} on the assumed width of the size distribution (Fig. 4.5, Tab. 4.2). The theoretical upper limit of the compatible r_{eff} is given by the monodisperse SD: a monodisperse distribution with $r = r_{\text{eff}} = 2.3 \mu\text{m}$ to $2.6 \mu\text{m}$ would provide the upper limit of r_{eff} of the ash for the observed Λ in Munich on 17 April 2010. However, as monodisperse size distributions of the ash particles are unrealistic, realistic r_{eff} of the observed ash are notably smaller, as found by the retrieval.

The weak dependence of Λ_{11} on particle shape and refractive index m (Figs. 3.6 and 4.5) suggests that the shape and m are only of minor importance for the retrieval of cross-section-equivalent sizes from aureole observations. However, as Fig. 4.6 shows, the retrieved particle volume and the mass-extinction conversion factor η depend on the particle shape. This dependency is a result of the proportionality between η and the cube of the shape-dependent radius conversion factor ξ_{vc}^3 (Eq. 2.40). For the irregularly-shaped particles used in the aureole retrieval, i.e. shapes B, D, and F of Fig. 2.2, the conversion factor ξ_{vc}^3 is 0.81 (B), 0.66 (D), and 0.65 (F), respectively, whereas for spherical particles ξ_{vc}^3 is equal to 1. An overestimation of the mass concentration by up to 50% may occur,

if those particles were observed, but spheres were assumed for the interpretation of the aureole observations. For vesicular ash particles, $\overline{\xi_{vc}^3}$ would be even smaller than 0.5, and a significant overestimation of the mass would occur if vesicularity of the ash was not considered. Electron microscopy images of ash particles provide valuable information for an estimation of $\overline{\xi_{vc}^3}$. The samples of ash plume particles from Eyjafjallajökull, presented by Schumann et al. (2011), indicate that most of the particles were non-vesicular, thus the $\overline{\xi_{vc}^3}$ of the model particles (Fig. 2.2) might be in a realistic range.

5.3. Dust properties from combined lidar and photometer retrieval

Like the aureole retrieval discussed in the previous section, the retrieval discussed here (described in Sect. 3.4.3 and applied in Sect. 4.3) did not rigorously explore the complete range of model parameter values but considered only a limited number of values for each model parameter (as given in Tab. 3.3), mainly because of the high computational demand of the radiative transfer calculations. The aim of this retrieval was to find at least one desert dust ensemble that agrees both with lidar and considered photometer observations. This aim was achieved for all three case studies of SAMUM observations on which this retrieval was applied. For example, agreement was achieved with lidar and photometer observations of 19 May 2006 by the desert aerosol ensemble from OPAC when it was modified for a more realistic representation of microphysical properties of real dust particles: spherical particles were replaced by particles with irregular shapes and the assumption that all dust particles have the same refractive index m was dropped by mixing absorbing and non-absorbing dust particles. In particular, it was shown that mixing of absorbing and non-absorbing particles is essential for realistic modeling of the lidar ratio of dust aerosols at short wavelengths. Otherwise, discrepancies between modeling and observations are found (see e.g., Müller et al., 2010a; Wiegner et al., 2009).

Consistent with the findings of the sensitivity study in Sect. 3.3.2 and the aureole retrieval of volcanic ash properties in Sect. 4.2, this retrieval demonstrated that the angular dependence of the scattering in the solar aureole primarily depends on the distribution of cross-section-equivalent particle sizes and that there is only a low sensitivity to the particle shape and a negligible sensitivity to the refractive index (see lower panels of Figs. 4.8, 4.10, and 4.12).

The OPAC desert size distribution resulted in a stronger angular dependence of the radiances in the solar aureole at $\lambda = 1020$ nm than observed during SAMUM-2. If the relative amount of large particles was reduced by applying the transport parameterization given by Koepke et al. (1997), agreement with SAMUM-2 aureole observations was found. By relating this agreement to the agreement of the unmodified OPAC desert size distribution with SAMUM-1 observations, it is found that the number of very large particles is reduced in the SAMUM-2 case compared to the SAMUM-1 cases. The effective radius of the dust fraction of these ensembles decreases from $r_{\text{eff}} = 1.75$ μm to $r_{\text{eff}} = 1.43$ μm . This is consis-

tent with stronger fall-out of large particles in the SAMUM-2 case, due to gravitational settling during the transport over a greater distance from the dust source.

Size distributions of desert dust aerosols from AERONET photometer retrievals and from Falcon in-situ optical measurements in the framework of the SAMUM campaign were used, in addition, for closure studies (Sect. 4.3); in these closure studies, the particle shapes and refractive indices of the aerosol particles were varied according to the uncertainty of these parameters. In the upper right and lower panels of Figs. 4.8, 4.10, and 4.12, the modeling results using the size distributions from AERONET (grey) and Falcon (orange) are compared to the photometer observations (black). These comparisons show that in the SAMUM-1 cases, both size distributions were largely in contradiction to the normalized aureole radiances and the wavelength dependence of the extinction by the aerosols observed by the photometers CIMEL and SSARA. The size distributions from AERONET contain significantly fewer particles with radii $r > 4 \mu\text{m}$ than the OPAC desert size distribution (see upper left panels of Figs. 4.8 and 4.10), which resulted in agreement with the aureole observations. The size distribution from Falcon in-situ observations contains more particles with radii $r > 3 \mu\text{m}$ than OPAC desert. This comparison suggests that the size distributions from AERONET contain too few large particles, whereas the size distributions from Falcon contain too many large particles. For the SAMUM-2 case (shown in Fig. 4.12), size distributions from AERONET retrievals and Falcon optical particle counters provided better agreement with aureole observations than for the SAMUM-1 cases. Because of the discrepancies between the radiation fields observed by CIMEL and the fields modeled with the available dust size distributions from SAMUM-1, it is necessary to investigate the accuracy of the aureole observations during SAMUM-1 in more detail. The CIMEL photometer that was deployed in SAMUM-1 is usually operated at the IfT in Leipzig, Germany. The almucantar observations of this instrument were searched for conditions with very low aerosol optical depth (data is available from the AERONET website). Such conditions were observed at 2 December 2006 10 UTC ($\tau_{1640} = 0.0145$, $\kappa_{\text{ext},440-870} = 1.44$, $z_s = 74^\circ$). Low aerosol optical depths are typically correlated with low amounts of large particles, which results in low sky radiances in the solar aureole. Low sky radiances in the aureole provide favorable conditions for the assessment of the instrument performance because error sources like straylight or electronic problems would become apparent. The sky radiance observed at $\lambda = 1640 \text{ nm}$ and azimuth angle 3° on 2 December 2006 is only about 3.5% of the radiance observed on 4 June 2006 7:07 UTC during SAMUM-1 in Morocco at the same azimuth angle of the almucantar (and comparable sun zenith angle z_s). If it is assumed that the radiances observed on 2 December 2006 are purely due to instrumental effects (implying no sky radiance at 1640 nm), this radiance field can be subtracted from any other observed radiance field (with comparable z_s) to yield the 'true' radiance field. It turns out that this subtraction has less effect on the normalized radiances in the solar aureole on 4 June 2006 than the uncertainty from the pointing of the photometer which was already considered in Fig. 4.10. Furthermore, model calculations showed that the non-consideration of the field-of-view and the angular size of the Sun has less effect on normalized radiances than the pointing uncertainties of the photometer. The effects of these uncertainties are smaller than the deviation of the modeled normalized radiances

from the observed radiances (Figs. 4.8 and 4.10), thus instrumental effects of the CIMEL photometer are not expected to explain the deviations using the size distributions from AERONET and Falcon during SAMUM-1.

In case of the size distributions from AERONET, one might expect that they provide the same radiance fields as those measured by the CIMEL because the CIMEL observations were used as input for the AERONET retrieval; but as shown, the radiation fields deviate in the solar aureole. An explanation for this deviation could be that the weighting of radiances at the different scattering angles in the AERONET retrieval was such that the forward scattering angles were only of low importance. In Sect. 3.3, however, it was shown that forward scattering radiances contain robust information about the aerosol size distribution so that radiances at these scattering angles should be used with high priority in size distribution retrievals. Further investigations, for example a review of the AERONET retrieval code, would help to better understand the reasons for the deviations.

The deviations of the radiance fields using the SAMUM-1 size distribution measured by the in-situ optical particle counters aboard the Falcon aircraft from the CIMEL observations might be explained by the dependence of the scattering on the refractive index m . The FSSP-300, which was the main optical particle counter of the Falcon during SAMUM-1 for particles up to $r \approx 10\text{-}20 \mu\text{m}$, registers the forward scattering by single aerosol particles in the angular range from about 3° to 15° at $\lambda = 632 \text{ nm}$ (Weinzierl, 2008). The upper left panels of Figs. 4.8 and 4.10 show that largest discrepancies between the size distribution from Falcon and OPAC (which provides agreement with the aureole observations) were found for particles with radii around $r \approx 5 \mu\text{m}$, which corresponds to $x \approx 50$ at the wavelength of the FSSP. At this size parameter x , the main diffraction peak is only in the range $0^\circ < \theta < 4^\circ$, whereas at larger θ only secondary diffraction peaks are found. The intensity of secondary diffraction peaks is low compared to the main peak, thus the fraction of the light that is refracted by the particle becomes relevant for $\theta \geq 4^\circ$. The refracted fraction of the light, in turn, is very sensitive to the imaginary part of the refractive index m_i . As a consequence, the m_i chosen for the inversion of the FSSP data can have considerable effects on the coarse mode fraction of the inverted size distribution (see e.g., Schumann et al., 2011) because the FSSP observes scattering up to $\theta = 15^\circ$. For example, if $m_i > 0$ is assumed, but large particles with $m_i = 0$ are sampled by the particle counter, their size is overestimated. m_i around 0.004, found for particles with $r < 1.25 \mu\text{m}$ were used in the complete size range for the FSSP-retrieval during SAMUM-1 (Weinzierl, 2008); however, according to Kandler et al. (2009), a considerable fraction of particles with much smaller m_i was present in the dust layers during SAMUM-1; thus, the sizes of these particles were overestimated by the FSSP retrieval. During the SAMUM-2 campaign, non-absorbing particles were assumed by the FSSP retrieval for $r > 1.25 \mu\text{m}$ (Weinzierl et al., 2011), which resulted in significantly smaller differences between modelled and observed radiance fields in the solar aureole (Fig. 4.12). The application of non-absorbing particles for $r > 1.25 \mu\text{m}$ in the FSSP retrieval is expected to improve the agreement also in the SAMUM-1 cases.

6. Conclusions

Aim of this study was the improvement of retrievals of microphysical aerosol properties from lidar and photometer observations. Retrievals for aerosols with non-spherical particle shapes, that is for volcanic ash and desert dust, were developed and applied to observations. These retrievals are based on a Bayesian approach and accept all physically meaningful solutions that agree with the observations. This approach allows for realistic propagation of the uncertainties from the observed parameters to the retrieved aerosol properties.

6.1. Synopsis of findings

In a case study (Sect. 4.1), ensembles of model spheroids were used to retrieve the mass concentration of pure transported volcanic ash aerosols from observations by advanced lidar systems. Due to the limited information content of the optical particles properties observed by lidar, the uncertainty of the retrieval result was in the order of 50 % (Fig. 4.2). The uncertainty of the retrieved mass concentration is mainly determined by the uncertainty of the retrieved particle size (Fig. 4.3). The results from the lidar retrieval were compared to results from an independent retrieval that uses aureole observations from photometer (Sect. 4.2). Good agreement between the retrieval results was found; thus for the first time, volcanic ash mass concentrations were successfully retrieved from lidar observations by means of a fully microphysical retrieval where particle size, particle shape, and refractive index were not known a priori.

In three case studies using measurements from the SAMUM field campaigns (Sect. 4.3), aerosol ensembles were determined that consistently explain lidar observations of Saharan dust aerosols as well as the wavelength dependence of extinction and the angular dependence of aureole radiances observed by collocated photometers. These aerosol ensembles were derived from the OPAC desert mixture (Hess et al., 1998) by using mixtures of absorbing and non-absorbing irregularly-shaped dust particles instead of only absorbing spherical dust particles (Sect. 3.3.2). Size distributions were varied according to transport parameterizations used in the global aerosol data set GADS (Koepke et al., 1997). A consistent picture of the evolution of the dust size distributions as a result of sedimentation was found: For the SAMUM-1 cases, which were located close to the dust source regions, a higher amount of large particles was found compared to the SAMUM-2 case, which was located at a greater distance from the source.

In addition, closure studies using size distributions from AERONET retrievals and optical particle counters were performed. Müller et al. (2010b) found large discrepancies between these size distributions for SAMUM-1. The closure studies in this thesis revealed,

mainly by comparing modeled and observed aureole radiances, that the size distributions from AERONET underestimate the amount of large particles during SAMUM-1, whereas the size distributions from optical particle counters overestimate the amount of large particles. For SAMUM-2 better agreement was found in the closure study.

Sensitivity studies revealed that the consideration of the wavelength dependence of the dust refractive index in model ensembles requires, in addition, the consideration of non-absorbing dust components to explain the observed wavelength dependence of the backscattering (Sects. 3.3.2 and 4.3). This requirement explains the discrepancies between modeling and observations found by Wiegner et al. (2009) and Müller et al. (2010a) for the wavelength dependence of the lidar ratio. However, if the wavelength dependence of the refractive index is not considered, comparatively simple ensembles where all particles have the same refractive index are sufficient to explain the lidar observations (Sects. 3.3.2 and 4.1). Furthermore, it was shown that the amount of particles with small aspect ratios ($\epsilon' < 1.4$) has to be low to explain the observed lidar ratios (Sects. 3.3.2 and 4.3). To also explain the observed depolarization ratios, irregularly-shaped particles (Sect. 4.3) or spheroids (Sect. 4.1) can be used. In case of spheroids, however, a lower refractive index m_r than typically obtained by other methods is required (Sect. 5.1). This is a result of the m_r -dependence of the depolarization by spheroids (Wiegner et al., 2009), which is not found for irregularly-shaped particles (Tab. 3.7). If these irregularly-shaped particles are accepted as realistic ones, it can be concluded that the retrieval of m_r from depolarization observations using a spheroid model is biased towards lower m_r .

The computations in this study demonstrated that aureole radiances are well-suited for the retrieval of the coarse mode fraction of the particle size distribution also in case of dust or ash aerosols: aureole radiances primarily depend on the cross section area of the particles, hardly depend on particle shape or refractive index, and are sensitive to comparatively large particles (Tab. 3.8, Figs. 3.13, 4.5, 4.8, 4.10, 4.12, and 3.5). If particle volume or mass is to be retrieved from aureole and extinction observations, the shape of the particles is also relevant because the cross section of a particle with fixed volume tends to increase with increasing deviation from spherical shape (see Eqs. 2.3 and 2.40). The particle becomes less compact. As a result, the assumption of spherical particles in a retrieval would lead to an overestimation of the volume and the mass of particles, provided that the cross-section-equivalent size of the non-spherical particles is retrieved correctly. In that sense, spheres would provide an upper limit of the volume or mass concentration, the “worst case”.

6.2. Outlook

A significant reduction of the computation time of the rigorous lidar retrieval described in Sect. 3.4.1 is expected from the future availability of highly parallel processors and the application of Markov Chain Monte Carlo methods for the sampling of the model parameter space. Markov Chain Monte Carlo methods are importance sampling methods, which sample acceptable models (i.e. solutions) more frequently than unacceptable models. An

increase of the accuracy of the retrievals can be expected from combining the rigorous sampling approach (Monte Carlo) with synergistic exploration of all available information from lidar and photometer, e.g., including sky radiances at all available wavelengths and scattering angles. This approach would provide sufficient information for successful retrievals even in case of mixed aerosols.

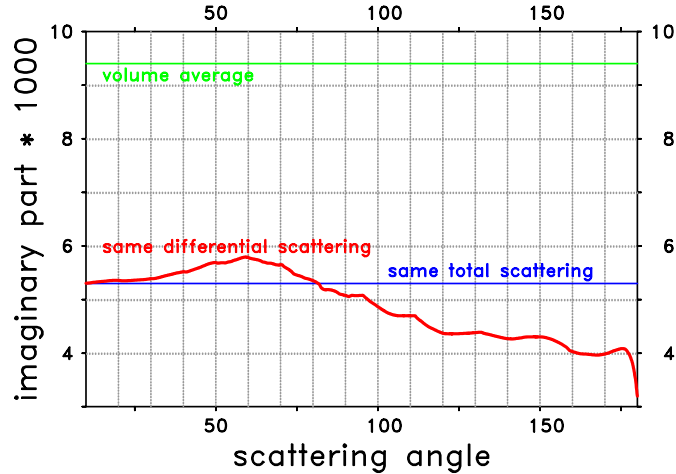


Figure 6.1.: Imaginary part of dust refractive index m_i of homogeneous mixtures which provide same volume-average m_i (green), same total scattering (blue), and same differential scattering (red) as the reference ensemble at $\lambda = 440$ nm (Sect. 3.3.2.2).

The synergistic exploration of lidar and photometer observations of sky radiances outside the solar aureole is expected to require complex aerosol models. As an example, Fig. 6.1 illustrates that homogeneous ensembles are not sufficient for this task: The red line in this figure displays the m_i of homogeneous dust mixtures (all dust particles have the same m_i) that provide the same amount of differential scattering $C_{\text{diffsca}}(\theta)$ at $\lambda = 440$ nm as the reference ensemble (absorbing and non-absorbing dust particles are mixed, Sect. 3.3.2). Photometers typically observe scattering in forward and sideward direction (typically up to $\theta \approx 120^\circ$), whereas lidar systems observe backscattering ($\theta = 180^\circ$). If the reference ensemble is accepted as a realistic aerosol ensemble, it is clear that the homogeneous aerosol model can not be applied for a synergistic retrieval from lidar and sky radiance observations because of the dependence of the required m_i on θ . Instead, a model that considers the mineralogical inhomogeneity of the particles is required. Therefore, an in-depth investigation of the effect of the mineralogical inhomogeneity on the observed parameters may help to develop adequate models.

The consideration of the size dependence of the refractive index and the particle shape may also be beneficial for optical modeling and retrievals. Observations at longer wavelengths and observations at smaller scattering angles extend the sensitivity of the retrievals

to larger particles. Such improvements are desirable in particular for applications close to the source regions. With respect to height-resolved detection, it is worth investigating whether multiple-scattered light provides valuable information about the size of the particles and whether extensions of the lidar technique, e.g. multiple-field-of-view lidar systems, are able to observe it with the required accuracy.

Data sets of optical properties of non-spherical particles, like those created in this work, are also useful for several other applications related to ash and dust aerosols. For example, the above-described spheroid data set (Sect. 3.2.1) was used for the creation of new aerosol scattering libraries of desert dust and volcanic ash (Petzold et al., 2011) in the EarthCare Simulator ECSIM (Donovan et al., 2001). ECSIM allows for the simulation of measurements of various types of instruments, in particular, spaceborne ones. With the consideration of the non-sphericity of the dust and ash aerosols in ECSIM, significantly more realistic simulations of aerosol observations are possible, allowing one to optimize the design of instruments on future satellites.

To facilitate the application of advanced aerosol models, the provision of optical data sets together with an user-friendly software is desirable. In this regard, a unified data format for the scattering properties of single particles is also desirable to allow easier exchange and usage of available modeling results (e.g., from Meng et al. (2010) and several other authors). Accurate methods for optical modeling of irregularly-shaped particles with very large size parameters would be beneficial for large particles at short wavelengths. The simulation of larger size parameters might become feasible by advances in the theoretical basis and the implementations of the modeling codes, but also the availability of highly parallel processors (CPUs or GPUs) may allow existing modeling codes to be used at slightly larger size parameters.

A. Optics of very small particles

Optical properties of very small spherical particles (size parameters $x \ll 1$ and $|mx| \ll 1$) are described by the Rayleigh theory (Rayleigh, 1897). Analytical expressions for the Rayleigh approximation exist only for a few simple particle shapes, as summarized by Mishchenko et al. (2002). According to Mishchenko et al. (2002) the optical properties of very small spheres are

$$q_{\text{sca}} = \frac{8}{3}x^4 \left| \frac{m^2 - 1}{m^2 + 2} \right|^2 \quad (\text{A.1})$$

$$q_{\text{abs}} = 4x \text{Im} \left(\frac{m^2 - 1}{m^2 + 2} \right)^2 \quad (\text{A.2})$$

$$F_{11}(\theta) = \frac{3}{4}(1 + \cos^2 \theta) \quad (\text{A.3})$$

The scattering efficiency q_{sca} is proportional to the fourth power of the size parameter x or, for fixed particle size, inversely proportional to the fourth power of the wavelength λ . The absorption efficiency q_{abs} is inversely proportional to λ . In case of small non-absorbing spheres ($\omega_0 = 1$), the lidar ratio (Eq. 2.24) is

$$S = \frac{8\pi}{3} \approx 8.38. \quad (\text{A.4})$$

Table A.1 presents numerical results for optical properties of spheres and randomly-oriented prolate spheroids with aspect ratio $\epsilon' = 3$ modeled using the Mie theory and the

property	sphere, $m_i = 0$	$\epsilon' = 3$, $m_i = 0$	sphere, $m_i = 0.01$	$\epsilon' = 3$, $m_i = 0.01$
q_{abs}	0	0	$1.96 \cdot 10^{-5}$	$1.79 \cdot 10^{-5}$
q_{sca}	$2.46 \cdot 10^{-13}$	$2.24 \cdot 10^{-13}$	$2.47 \cdot 10^{-13}$	$2.24 \cdot 10^{-13}$
$F_{11}(90^\circ)$	0.750	0.756	0.750	0.756
$F_{11}(180^\circ)$	1.500	1.489	1.500	1.489
S	8.38	8.44	$6.67 \cdot 10^8$	$6.72 \cdot 10^8$
d	0	0.015	0	0.015

Table A.1.: Optical properties of very small spheres and prolate spheroids with aspect ratio $\epsilon' = 3$ and varying imaginary part m_i of the refractive index; $m_r = 1.52$; vol.-equ. size parameter $x_v = 0.001$.

T-matrix method. The q_{sca} and q_{abs} of the spheroids is by about 10% lower compared to spheres with the same volume; the geometrical cross section C_{geo} of the spheroids is 18% larger in this case, thus the cross sections C_{sca} and C_{abs} of the spheroids are by about 8% larger than for spheres. The effect of particle shape on the phase function F_{11} and the lidar ratio S is smaller than 1%. For very small particles with $m_i > 0$, light extinction is dominated by absorption, whereas scattering is negligible. As a consequence, the lidar ratio S is very high for very small absorbing particles.

B. Settings of optical modeling codes

Settings of T-matrix code

For the calculation of optical properties of randomly-oriented spheroids with $\epsilon' > 1$, the LAPACK-based extended-precision version of the T-matrix code from Mishchenko and Travis (1998) was used¹. To maximize the coverage of the particle spectrum (x , ϵ' , and m), the following parameters of the code was chosen: NPN1 = 290 (default 140), NPNG1 = 870 (default 500), and NPN4 = 260 (default 100). Though, in general, the TMM provides exact solutions for scattering problems, non-physical results might be obtained due to numerical problems. To reduce the probability of non-physical results and to increase the accuracy of the results, the parameter DDELTA, i.e. the absolute accuracy of computing the expansion coefficients, was set to 10^{-6} (default 10^{-3}). For particles that could not be simulated with DDELTA = 10^{-6} , DDELTA was increased up to the default value. Particle that could not be simulated even with the default DDELTA were not considered in the database. Nevertheless, some non-physical results were obtained by this approach, for example, $\omega_0 > 1$, or outliers of otherwise smooth $\omega_0(x)$ or $g(x)$. Thus, the results were manually checked for plausibility before they were stored in the database. For the plausibility checks, single scattering albedos ω_0 and asymmetry parameters g were plotted over size parameter and outliers were recalculated, or removed as the last resort.

Settings of CGOM and IGOM codes

The following parameters were used for the CGOM calculations of \mathbf{F} at $\theta > 10^\circ$: n_ray = 1000 (default 250), n_orient = 30 000 (default 10 000), and n_r_max = 1000. The computation time using these parameters is significantly higher compared to the default parameters, but results are more accurate, in particular in backward direction. Individual CGOM runs were necessary for each angular range in Tab. 3.1 because the CGOM code uses equidistant angular steps for the angle bins. For calculations in the range from 1° to 10° smaller values for n_ray and n_orient were used to save computation time. For $\theta < 1^\circ$ the Mie theory was used: For each spheroid, the Mie theory was applied on a size distribution of spheres that results in the same distribution of projected areas as the spheroid, if it is randomly rotated. The following parameters were used for the IGOM calculations: N_RAYS = 30 000 000 (default 8 000 000), N_TIME1 = 100 (default 7), and N_TIME2 = 1000 (default 10). By the higher-than-default values, the accuracy of the IGOM calculations was improved.

¹version 08/06/2005, available under http://www.giss.nasa.gov/staff/mmishchenko/t_matrix.html

Creation of the irregularly-shaped model particles

In the first step, Hyperfun² (Valery et al., 1999) was used to create the three-dimensional particle shown in Fig. 2.2. Hyperfun is a volume modeling language: an object in the three-dimensional space is defined by a continuous real-valued function $G(x, y, z)$. This function is positive inside the particle and negative outside, thus it is zero at the surface. In Hyperfun, the function G can be a combination of different functions. Many pre-defined functions are readily available in Hyperfun. For example, an ellipsoid is constructed using the built-in function *hfEllipsoid*. The parameters of *hfEllipsoid* are the coordinates of its center and the three half-axes of the ellipsoid. Using the function *hfNoiseG*, deformations following the Gardner series (Gardner, 1984) can be added to the three-dimensional space. Parameters of *hfNoiseG* are amplitude *amp*, frequency *freq* and *phase*. The function *hfNoiseG* is implemented in Hyperfun as

$$\begin{aligned}
 Serx &= amp \cdot \sin(freq \cdot x) + amp/1.17 \cdot \sin(freq \cdot x/1.35 + phase \cdot \sin(freq \cdot z)) \\
 Sery &= amp \cdot \sin(freq \cdot y) + amp/1.17 \cdot \sin(freq \cdot y/1.35 + phase \cdot \sin(freq \cdot x)) \\
 Serz &= amp \cdot \sin(freq \cdot z) + amp/1.17 \cdot \sin(freq \cdot z/1.35 + phase \cdot \sin(freq \cdot y)) \\
 hfNoiseG &= Serx \cdot Sery \cdot Serz
 \end{aligned}$$

The shapes A, B, and C (Fig. 2.2) were created by adding solid noise with $amp = 0.5$, $freq = 4.0$, and $phase = 1.4$ on the spheroids:

$$\begin{aligned}
 \text{shape A: } G(x,y,z) &= hfEllipsoid([x,y,z], [0,0,0], 1.4, 1, 1) \\
 &\quad + hfNoiseG([x,y,z], 0.5, 4, 1.4)
 \end{aligned}$$

$$\begin{aligned}
 \text{shape B: } G(x,y,z) &= hfEllipsoid([x,y,z], [0,0,0], 1.8, 1, 1) \\
 &\quad + hfNoiseG([x,y,z], 0.5, 4, 1.4)
 \end{aligned}$$

$$\begin{aligned}
 \text{shape C: } G(x,y,z) &= hfEllipsoid([x,y,z], [0,0,0], 2.4, 1, 1) \\
 &\quad + hfNoiseG([x,y,z], 0.5, 4, 1.4)
 \end{aligned}$$

Shape D consists of overlapping ellipsoids (symbol "|" is the union operator):

$$\begin{aligned}
 \text{shape D: } G(x,y,z) &= hfEllipsoid([x,y,z], [0,0,0], 1, 0.6, 2.4) \\
 &\quad | hfEllipsoid([x,y,z], [0,1,0], 1.4, 1, 1) \\
 &\quad | hfEllipsoid([x,y,z], [0,1,1], 1, 0.4, 1) \\
 &\quad | hfEllipsoid([x,y,z], [1,0,1.5], 0.5, 1, 1) \\
 &\quad | hfEllipsoid([x,y,z], [1,0.5,-1.5], 1, 0.6, 0.4) \\
 &\quad | hfEllipsoid([x,y,z], [-1,0,2], 1, 1, 0.7) \\
 &\quad | hfEllipsoid([x,y,z], [0,-1,2], 1, 0.6, 1) \\
 &\quad | hfEllipsoid([x,y,z], [0,0,-1], 0.8, 0.5, 1.2)
 \end{aligned}$$

²<http://hyperfun.org>

```

| hfEllipsoid([x,y,z],[-1,-0.5,1],0.6,0.4,1)
| hfEllipsoid([x,y,z],[-0.5,0.5,-1.5],0.4,0.7,1)
+ hfNoiseG([x,y,z],0.5,4,1.4)

```

Shape E was created using intersections (symbol "&"):

```

shape E: G(x,y,z) = 3-abs(x)-0.7*abs(y)-0.5*abs(z)
& 3-1.2*z-0.7*y-0.4*x
& 2.5-0.8*y+0.2*x
& 3+0.8*y+1.2*x-0.2*z
& 4+1.2*z-0.3*y

```

Shape F was created from shape E by using the function *hfStretch3D* to stretch the particle by a factor two in the z-direction.

Hyperfun creates a file in the *wrl*-format ("Virtual Reality Modelling Language"), which contains the description of the surface of the particle. For the density of the surface grid (Hyperfun option "-g"), a value of 180 was chosen, thus the surface of the particle is well sampled. Using Accutrans³, the *wrl*-file was converted to the *obj*-format, which still contains the description of the particle surface. In the next step, the *obj*-file was converted in a ADDA-compatible format. This task was done by the program pip ("Point in Polyhedron") provided by Roman Schuh (University of Bremen, Germany). For a given three-dimensional grid, the program decides at each grid point, whether the point is inside or outside the particle. If the point is inside, it is added to the ADDA input file. A command line parameter of pip is the grid density. For the ADDA calculations a minimum number of dipoles per wavelength is required, thus the grid density had to be adjusted for each size parameter.

³<http://www.micromouse.ca/>

C. Modeling of spheroids with ADDA

For the validation of the modeling approach using ADDA, as described in Sect. 2.3.4, it would be useful to compare its results to results from a numerically exact approach. A numerically exact approach for irregularly-shaped particles (Fig. 2.2), however, is not available. Only for spheroids, numerically exact results are available by means of the T-matrix method (Sect. 2.3.2); thus in this appendix, ADDA results for spheroids are compared to results from the T-matrix method.

property	$\epsilon' = 1.8$		$\epsilon' = 2.4$	
	T-matrix	ADDA	T-matrix	ADDA
C_{abs}	$0.699 \mu\text{m}^2$	$0.698 \mu\text{m}^2$	$0.696 \mu\text{m}^2$	$0.691 \mu\text{m}^2$
C_{sca}	$7.131 \mu\text{m}^2$	$7.157 \mu\text{m}^2$	$6.666 \mu\text{m}^2$	$6.687 \mu\text{m}^2$
$F_{11}(0^\circ)$	70.8	71.1	66.4	66.5
$F_{11}(90^\circ)$	0.206	0.209	0.380	0.384
$F_{11}(180^\circ)$	0.383	0.367	0.270	0.321
S	36.1	37.3	51.5	43.1
d	0.317	0.351	0.463	0.474

Table C.1.: Optical properties of randomly-oriented prolate spheroids with different aspect ratios ϵ' , $m = 1.52 + 0.0043i$ and $r_v = 1 \mu\text{m}$ at $\lambda = 0.628 \mu\text{m}$ ($x_v = 10$) modeled using different methods: T-matrix method and ADDA with approach used in this thesis (shape creation as described in Appendix B for shapes B and C but without application of Gardner noise).

As an example, Tab. C.1 compares orientation-averaged results from ADDA and the T-matrix method for spheroids with two aspect ratio ϵ' and a volume-equivalent size parameter $x_v = 10$. For the cross sections and the forward scattering, deviations smaller than 1% are found. The scattering at $\theta = 90^\circ$ deviates by about 1%. In the highly sensitive backward direction, the largest deviations are found: The deviations are up to about 16%.

The uncertainty of the ADDA calculations for spheroids is larger than the uncertainty found for the irregularly-shaped particles in Sect. 2.3.4, which were smaller than 8% for the backscattering properties. The higher uncertainty of spheroids can be explained by the symmetry of the spheroids. Figure C.1 illustrates the effect of the symmetry of the particle on the backscattering cross section. In this figure, the backscattering by a spheroid (left) and by an irregularly-shaped particle (right) is plotted as a function of the particle orientation (vertical: β_e , horizontal: γ_e). Due to the rotational symmetry of spheroids (and

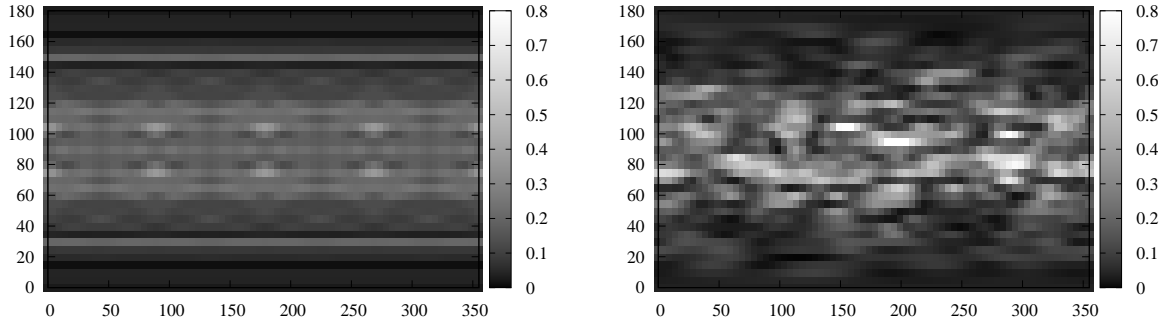


Figure C.1.: Differential backscattering cross section $C_{\text{diffsca}}(180^\circ)$ in μm^2 of prolate spheroids with $\epsilon' = 2.4$ without (left) and with Gardner noise (shape C, right) modeled using ADDA and plotted over Euler angles β_e (vertical) and γ_e (horizontal); $m = 1.52 + 0.0043i$, $r_v = 1 \mu\text{m}$ at $\lambda = 0.628 \mu\text{m}$ ($x_v = 10$); resolution of β_e and γ_e is 5° .

the choice of the coordinate systems), their optical properties do not depend on γ_e (ADDA calculations show a weak γ_e -dependence because of the discretisation of the spheroid on a cubic grid). As a consequence, the orientation averaging scheme, developed in Sect. 2.3.4 and used for the calculations, basically does the same ADDA calculations several times in case of spheroids. Of the 526 ADDA runs of this averaging scheme, only 11 runs are independent for spheroids (β_e from 0° to 90° with step width 9°). Due to the lower number of independent simulations and the resultant diminishing statistics, the application of this averaging approach results in larger errors for spheroids than for irregularly-shaped particles.

D. Publications containing work from this thesis

Main parts of this thesis are published in:

- Gasteiger et al. (2011a)
- Gasteiger et al. (2011b)

Contributions from this thesis' work are published in:

- Groß et al. (2011)
- Groß et al. (2011a)
- Müller et al. (2010a)
- Müller et al. (2011)
- Schladitz et al. (2011)
- Schumann et al. (2011)
- Toledano et al. (2011)
- Wiegner et al. (2009)
- Wiegner et al. (2011a)
- Wiegner et al. (2011b)

Bibliography

- Ansmann, A., Wandinger, U., Riebesell, M., Weitkamp, C., and Michaelis, W.: Independent measurement of extinction and backscatter profiles in cirrus clouds by using a combined Raman elastic-backscatter lidar, *Appl. Opt.*, 31, 7113, doi:10.1364/AO.31.007113, 1992.
- Ansmann, A., Tesche, M., Groß, S., Freudenthaler, V., Seifert, P., Hiebsch, A., Schmidt, J., Wandinger, U., Mattis, I., Müller, D., and Wiegner, M.: The 16 April 2010 major volcanic ash plume over central Europe: EARLINET lidar and AERONET photometer observations at Leipzig and Munich, Germany, *Geophys. Res. Lett.*, 37, doi:10.1029/2010GL043809, 2010.
- Ansmann, A., Petzold, A., Kandler, K., Tegen, I., Wendisch, M., Müller, D., Weinzierl, B., Müller, T., and Heintzenberg, J.: Saharan Mineral Dust Experiments SAMUM-1 and SAMUM-2: What have we learned?, *Tellus B*, 63, 403–429, doi:10.1111/j.1600-0889.2011.00555.x, 2011a.
- Ansmann, A., Tesche, M., Seifert, P., Groß, S., Freudenthaler, V., Apituley, A., Wilson, K. M., Serikov, I., Linné, H., Heinold, B., Hiebsch, A., Schnell, F., Schmidt, J., Mattis, I., Wandinger, U., and Wiegner, M.: Ash and fine-mode particle mass profiles from EARLINET-AERONET observations over central Europe after the eruptions of the Eyjafjallajökull volcano in 2010, *J. Geophys. Res.*, 116, D00U02, doi:10.1029/2010JD015567, 2011b.
- Böckmann, C. and Wauer, J.: Algorithms for the inversion of light scattering data from uniform and non-uniform particles, *J. Aerosol Sci.*, 32, 49 – 61, doi:10.1016/S0021-8502(00)00052-5, 2001.
- Bösenberg, J. et al.: EARLINET: A European Aerosol Research Lidar Network to Establish an Aerosol Climatology, Max-Planck-Institut Report No. 348, Hamburg, 2003.
- Buras, R. and Mayer, B.: Efficient unbiased variance reduction techniques for Monte Carlo simulations of radiative transfer in cloudy atmospheres: The solution, *J. Quant. Spectrosc. Radiat. Transf.*, 112, 434 – 447, doi:10.1016/j.jqsrt.2010.10.005, 2011.
- Buras, R., Dowling, T., and Emde, C.: New secondary-scattering correction in disort with increased efficiency for forward scattering, *J. Quant. Spectrosc. Radiat. Transf.*, 112, 2028–2034, doi:10.1016/j.jqsrt.2011.03.019, 2011.

- Casadevall, T. J., ed.: *Volcanic Ash and Aviation Safety: Proceedings of the First International Symposium on Volcanic Ash and Aviation Safety, July 1991, Seattle, Washington, 1994.*
- Deepak, A., Box, G. P., and Box, M. A.: Experimental validation of the solar aureole technique for determining aerosol size distributions, *Appl. Opt.*, 21, 2236–2243, doi:10.1364/AO.21.002236, 1982.
- Donovan, D. et al.: *The EarthCARE Simulator: Users Guide and Final Report, Tech. rep., ESA CONTRACT NO 15346/01/NL/MM, 2001.*
- Draxler, R. R. and Rolph, G. D.: HYSPLIT (HYbrid Single-Particle Lagrangian Integrated Trajectory) Model access via NOAA ARL READY Website (<http://ready.arl.noaa.gov/HYSPLIT.php>), NOAA Air Resources Laboratory, Silver Spring, MD, 2010.
- Dubovik, O., Holben, B., Eck, T. F., Smirnov, A., Kaufman, Y. J., King, M. D., Tanré, D., and Slutsker, I.: Variability of Absorption and Optical Properties of Key Aerosol Types Observed in Worldwide Locations., *J. Atmos. Sci.*, 59, 590–608, doi:10.1175/1520-0469(2002)059<0590:VOAAOP>2.0.CO;2, 2002.
- Dubovik, O., Sinyuk, A., Lapyonok, T., Holben, B. N., Mishchenko, M., Yang, P., Eck, T. F., Volten, H., Muñoz, O., Veihermann, B., van der Zande, W. J., Leon, J., Sorokin, M., and Slutsker, I.: Application of spheroid models to account for aerosol particle nonsphericity in remote sensing of desert dust, *J. Geophys. Res.*, 111, doi:10.1029/2005JD006619, 2006.
- Eloranta, E. E.: High Spectral Resolution Lidar, in: *LIDAR: Range-Resolved Optical Remote Sensing of the Atmosphere*, edited by Weitkamp, C., pp. 143–163, Springer, doi:10.1007/0-387-25101-4_5, 2005.
- Esselborn, M., Wirth, M., Fix, A., Weinzierl, B., Rasp, K., Tesche, M., and Petzold, A.: Spatial distribution and optical properties of Saharan dust observed by airborne high spectral resolution lidar during SAMUM 2006, *Tellus B*, 61, 131–143, doi:10.1111/j.1600-0889.2008.00394.x, 2009.
- Fernald, F. G.: Analysis of atmospheric lidar observations: some comments, *Appl. Opt.*, 23, 652–653, doi:10.1364/AO.23.000652, 1984.
- Flentje, H., Claude, H., Elste, T., Gilge, S., Köhler, U., Plass-Dülmer, C., Steinbrecht, W., Thomas, W., Werner, A., and Fricke, W.: The Eyjafjallajökull eruption in April 2010 - detection of volcanic plume using in-situ measurements, ozone sondes and lidar-ceilometer profiles, *Atmos. Chem. Phys.*, 10, 10 085–10 092, doi:10.5194/acp-10-10085-2010, 2010.

- Freudenthaler, V., Esselborn, M., Wiegner, M., Heese, B., Tesche, M., Ansmann, A., Müller, D., Althausen, D., Wirth, M., Fix, A., Ehret, G., Knippertz, P., Toledano, C., Gasteiger, J., Garhammer, M., and Seefeldner, M.: Depolarization ratio profiling at several wavelengths in pure Saharan dust during SAMUM 2006, *Tellus B*, 61, 165–179, doi:10.1111/j.1600-0889.2008.00396.x, 2009.
- Gardner, G. Y.: Simulation of natural scenes using textured quadric surfaces, *Proceedings of the 11th annual conference on Computer graphics and interactive techniques*, pp. 11–20, 1984.
- Gasteiger, J., Groß, S., Freudenthaler, V., and Wiegner, M.: Volcanic ash from Iceland over Munich: mass concentration retrieved from ground-based remote sensing measurements, *Atmos. Chem. Phys.*, 11, 2209–2223, doi:10.5194/acp-11-2209-2011, 2011a.
- Gasteiger, J., Wiegner, M., Groß, S., Freudenthaler, V., Toledano, C., Tesche, M., and Kandler, K.: Modeling lidar-relevant optical properties of complex mineral dust aerosols, *Tellus B*, 63, 725–741, doi:10.1111/j.1600-0889.2011.00559.x, 2011b.
- Gertisser, R.: Eyjafjallajökull volcano causes widespread disruption of European air traffic, *Geology Today*, 26, 94–95, doi:10.1111/j.1365-2451.2010.00757.x, 2010.
- Gimmestad, G. G.: Reexamination of depolarization in lidar measurements, *Appl. Opt.*, 47, 3795–3802, doi:10.1364/AO.47.003795, 2008.
- Groß, S., Freudenthaler, V., Toledano, C., Seefeldner, M., and Wiegner, M.: Mini-lidar measurements of particle depolarization and Raman scattering of Saharan-dust and biomass burning at 355 nm during SAMUM 2, *Proc. of 24th International Laser Radar Conference, Boulder, USA, 23-27 June 2008*, S04P-10, 2008.
- Groß, S., Freudenthaler, V., Gasteiger, J., Schnell, F., and Wiegner, M.: Characterization of the Eyjafjallajökull ash-plume by means of Lidar measurements over the Munich EARLINET-site, *Spie Conference, Toulouse, France, 20 - 23 September 2010*, Paper 7832-20, 2010.
- Groß, S., Freudenthaler, V., Wiegner, M., Gasteiger, J., Geiß, A., and Schnell, F.: Dual-wavelength linear depolarization ratio of volcanic aerosols: lidar measurements of the Eyjafjallajökull plume over Maisach, Germany, *Atm. Env.*, In Press, Accepted Manuscript, doi:10.1016/j.atmosenv.2011.06.017, 2011.
- Groß, S., Gasteiger, J., Freudenthaler, V., Wiegner, M., Geiß, A., Schladitz, A., Toledano, C., Kandler, K., Tesche, M., Ansmann, A., and Wiedensohler, A.: Characterization of the planetary boundary layer during SAMUM-2 by means of lidar measurements, *Tellus B*, 63, 695–705, doi:10.1111/j.1600-0889.2011.00557.x, 2011a.
- Groß, S., Tesche, M., Freudenthaler, V., Toledano, C., Wiegner, M., Ansmann, A., Althausen, D., and Seefeldner, M.: Characterization of Saharan dust, marine aerosols

- and mixtures of biomass burning aerosols and dust by means of multi-wavelength depolarization- and Raman-measurements during SAMUM-2, *Tellus B*, 63, 706–724, doi:10.1111/j.1600-0889.2011.00556.x, 2011b.
- Hansen, J. E. and Travis, L. D.: Light scattering in planetary atmospheres, *Space Science Reviews*, 16, 527–610, doi:10.1007/BF00168069, 1974.
- Haywood, J. M., Pelon, J., Formenti, P., Bharmal, N., Brooks, M., Capes, G., Chazette, P., Chou, C., Christopher, S., Coe, H., Cuesta, J., Derimian, Y., Desboeufs, K., Greed, G., Harrison, M., Heese, B., Highwood, E. J., Johnson, B., Mallet, M., Marticorena, B., Marsham, J., Milton, S., Myhre, G., Osborne, S. R., Parker, D. J., Rajot, J., Schulz, M., Slingo, A., Tanré, D., and Tulet, P.: Overview of the Dust and Biomass-burning Experiment and African Monsoon Multidisciplinary Analysis Special Observing Period-0, *J. Geophys. Res.*, 113, D00C17, doi:10.1029/2008JD010077, 2008.
- Heintzenberg, J.: The SAMUM-1 experiment over Southern Morocco: overview and introduction, *Tellus B*, 61, 2–11, doi:10.1111/j.1600-0889.2008.00403.x, 2009.
- Herman, B. R., Gross, B., Moshary, F., and Ahmed, S.: Bayesian assessment of uncertainty in aerosol size distributions and index of refraction retrieved from multiwavelength lidar measurements, *Appl. Opt.*, 47, 1617–1627, doi:10.1364/AO.47.001617, 2008.
- Hess, M., Koepke, P., and Schult, I.: Optical Properties of Aerosols and Clouds: The Software Package OPAC, *Bull. Amer. Meteor. Soc.*, 79, 831–844, doi:10.1175/1520-0477(1998)079<0831:OPOAAC>2.0.CO;2, 1998.
- Holben, B. N., Eck, T. F., Slutsker, I., Tanré, D., Buis, J. P., Setzer, A., Vermote, E., Reagan, J. A., Kaufman, Y. J., Nakajima, T., Lavenu, F., Jankowiak, I., and Smirnov, A.: AERONET—A Federated Instrument Network and Data Archive for Aerosol Characterization, *Remote Sensing of Environment*, 66, 1–16, doi:10.1016/S0034-4257(98)00031-5, 1998.
- International Civil Aviation Organization: EUR DOC 019 - Volcanic Ash Contingency Plan EUR and NAT Regions (2nd Edition), URL http://www.paris.icao.int/documents_open/show_file.php?id=334, access: 19 Aug 2011, 2011.
- Ishimoto, H., Zaizen, Y., Uchiyama, A., Masuda, K., and Mano, Y.: Shape modeling of mineral dust particles for light-scattering calculations using the spatial Poisson-Voronoi tessellation, *J. Quant. Spectrosc. Radiat. Transfer*, 111, 2434 – 2443, doi:10.1016/j.jqsrt.2010.06.018, 2010.
- Jäger, H.: Long-term record of lidar observations of the stratospheric aerosol layer at Garmisch-Partenkirchen, *J. Geophys. Res.*, 110, doi:10.1029/2004JD005506, 2005.
- Kalashnikova, O. V. and Sokolik, I. N.: Modeling the radiative properties of nonspherical soil-derived mineral aerosols, *J. Quant. Spectrosc. Radiat. Transfer*, 87, 137–166, doi:10.1016/j.jqsrt.2003.12.026, 2004.

- Kandler, K., Benker, N., Bundke, U., Cuevas, E., Ebert, M., Knippertz, P., Rodríguez, S., Schütz, L., and Weinbruch, S.: Chemical composition and complex refractive index of Saharan Mineral Dust at Izaa, Tenerife (Spain) derived by electron microscopy, *Atm. Env.*, 41, 8058 – 8074, doi:10.1016/j.atmosenv.2007.06.047, 2007.
- Kandler, K., Schütz, L., Deutscher, C., Ebert, M., Hofmann, H., Jäckel, S., Jaenicke, R., Knippertz, P., Lieke, K., Massling, A., Petzold, A., Schladitz, A., Weinzierl, B., Wiedensohler, A., Zorn, S., and Weinbruch, S.: Size distribution, mass concentration, chemical and mineralogical composition and derived optical parameters of the boundary layer aerosol at Tinfou, Morocco, during SAMUM 2006, *Tellus B*, 61, 32–50, doi:10.1111/j.1600-0889.2008.00385.x, 2009.
- Kandler, K., Lieke, K., Benker, N., Emmel, C., Küpper, M., Müller-Ebert, D., Scheuven, D., Schladitz, A., Schütz, L., and Weinbruch, S.: Electron microscopy of particles collected at Praia, Cape Verde, during the Saharan Mineral dust experiment: particle chemistry, shape, mixing state and complex refractive index, *Tellus B*, 63, 475–496, doi:10.1111/j.1600-0889.2011.00550.x, 2011.
- Koepke, P., Hess, M., Schult, I., and Shettle, E.: Global Aerosol Data Set, Tech. rep., report No. 243 of the Max-Planck-Institut fuer Meteorologie, Hamburg, 1997.
- Lindqvist, H., Muinonen, K., and Nousiainen, T.: Light scattering by coated Gaussian and aggregate particles, *J. Quant. Spectrosc. Radiat. Transfer*, 110, 1398 – 1410, doi:10.1016/j.jqsrt.2009.01.015, 2009.
- Liou, K. N.: An Introduction to Atmospheric Radiation, Academic Press, 2002.
- Lohmann, U. and Feichter, J.: Global indirect aerosol effects: a review, *Atmos. Chem. Phys.*, 5, 715–737, doi:10.5194/acp-5-715-2005, 2005.
- Macke, A., Mishchenko, M. I., Muinonen, K., and Carlson, B. E.: Scattering of light by large nonspherical particles: ray-tracing approximation versus T-matrix method, *Optics Letters*, 20, 1934–1936, doi:10.1364/OL.20.001934, 1995.
- Marchuk, G. I.: Monte Carlo Methods in Atmospheric Optics, Springer, 1980.
- Mather, T. A., Pyle, D. M., and Oppenheimer, C.: Tropospheric Volcanic Aerosol, in: *Volcanism and the Earth's atmosphere*, Geophysical monograph 139, edited by: Robock, A. and Oppenheimer, C., Am. Geophys. Union, Washington, D.C., pp. 189–212, 2003.
- Mattis, I., Siefert, P., Müller, D., Tesche, M., Hiebsch, A., Kanitz, T., Schmidt, J., Finger, F., Wandinger, U., and Ansmann, A.: Volcanic aerosol layers observed with multiwavelength Raman lidar over central Europe in 2008-2009, *J. Geophys. Res.*, 115, doi:10.1029/2009JD013472, 2010.
- Mayer, B.: Radiative transfer in the cloudy atmosphere, *European Physical Journal Conferences*, 1, 75–99, doi:10.1140/epjconf/e2009-00912-1, 2009.

- Mayer, B. and Kylling, A.: Technical note: The libRadtran software package for radiative transfer calculations - description and examples of use, *Atmos. Chem. Phys.*, 5, 1855–1877, doi:10.5194/acp-5-1855-2005, 2005.
- McFarquhar, G. M. and Heymsfield, A. J.: The Definition and Significance of an Effective Radius for Ice Clouds., *Journal of Atmospheric Sciences*, 55, 2039–2052, doi:10.1175/1520-0469(1998)055<2039:TDASOA>2.0.CO;2, 1998.
- Meng, Z., Yang, P., Kattawar, G. W., Bi, L., Liou, K., and Laszlo, I.: Single-scattering properties of tri-axial ellipsoidal mineral dust aerosols: A database for application to radiative transfer calculations, *J. Aerosol Sci.*, 41, 501 – 512, doi:10.1016/j.jaerosci.2010.02.008, 2010.
- Metropolis, N., Rosenbluth, A. W., Rosenbluth, M. N., Teller, A. H., and Teller, E.: Equation of State Calculations by Fast Computing Machines, *J. Chem. Phys.*, 21, 1087–1092, doi:10.1063/1.1699114, 1953.
- Mie, G.: Beiträge zur Optik trüber Medien, speziell kolloidaler Metallösung, *Annalen der Physik*, 25, 377–445, doi:10.1002/andp.19083300302, 1908.
- Mishchenko, M. I. and Travis, L. D.: Capabilities and limitations of a current Fortran implementation of the T-Matrix method for randomly oriented, rotationally symmetric scatterers, *J. Quant. Spectrosc. Radiat. Transfer*, 60, 309–324, doi:10.1016/S0022-4073(98)00008-9, 1998.
- Mishchenko, M. I., Travis, L. D., Kahn, R. A., and West, R. A.: Modeling phase functions for dustlike tropospheric aerosols using a shape mixture of randomly oriented polydisperse spheroids, *J. Geophys. Res.*, 102, 16 831–16 847, doi:10.1029/96JD02110, 1997.
- Mishchenko, M. I., Travis, L. D., and Lacis, A. A.: *Scattering, Absorption, and Emission of Light by Small Particles*, Cambridge University Press, 2002.
- Morales, C., ed.: *Saharan Dust: Mobilization, Transport, Deposition: papers and recommendations from a workshop held in Gothenburg, Sweden, 25-28 April, 1977*, John Wiley & Sons, 1979.
- Mosegaard, K. and Tarantola, A.: Monte Carlo sampling of solutions to inverse problems, *J. Geophys. Res.*, 100, 12 431–12 448, doi:10.1029/94JB03097, 1995.
- Mosegaard, K. and Tarantola, A.: Probabilistic approach to inverse problems, in: *International Handbook of Earthquake & Engineering Seismology, Part A*, pp. 237–265, Academic Press, 2002.
- Müller, D., Wandinger, U., and Ansmann, A.: Microphysical Particle Parameters from Extinction and Backscatter Lidar Data by Inversion with Regularization: Theory, *Appl. Opt.*, 38, 2346–2357, doi:10.1364/AO.38.002346, 1999.

- Müller, D., Ansmann, A., Freudenthaler, V., Kandler, K., Toledano, C., Hiebsch, A., Gasteiger, J., Esselborn, M., Tesche, M., Heese, B., Althausen, D., Weinzierl, B., Petzold, A., and Hoyningen-Huene, W.: Mineral dust observed with AERONET Sun photometer, Raman lidar, and in situ instruments during SAMUM 2006: Shape-dependent particle properties, *J. Geophys. Res.*, 115, D11 207, doi:10.1029/2009JD012523, 2010a.
- Müller, D., Weinzierl, B., Petzold, A., Kandler, K., Ansmann, A., Müller, T., Tesche, M., Freudenthaler, V., Esselborn, M., Heese, B., Althausen, D., Schladitz, A., Otto, S., and Knippertz, P.: Mineral dust observed with AERONET Sun photometer, Raman lidar, and in situ instruments during SAMUM 2006: Shape-independent particle properties, *J. Geophys. Res.*, 115, D07 202, doi:10.1029/2009JD012520, 2010b.
- Müller, D., Gasteiger, J., Otto, S., Tesche, M., Kandler, K., Müller, T., Freudenthaler, V., Toledano, C., Althausen, D., and Ansmann, A.: Comparison of Optical and Microphysical Properties of Pure Saharan Mineral Dust Observed With AERONET Sun Photometer, Raman Lidar, and In-Situ Instruments During SAMUM 2006, *J. Geophys. Res.*, submitted, 2011.
- Müller, H. and Quenzel, H.: Information content of multispectral lidar measurements with respect to the aerosol size distribution, *Appl. Opt.*, 24, 648–654, doi:10.1364/AO.24.000648, 1985.
- Nakajima, T. and Tanaka, M.: Algorithms for radiative intensity calculations in moderately thick atmospheres using a truncation approximation, *J. Quant. Spectrosc. Radiat. Transf.*, 40, 51–69, doi:10.1016/0022-4073(88)90031-3, 1988.
- Nakajima, T., Tanaka, M., and Yamauchi, T.: Retrieval of the optical properties of aerosols from aureole and extinction data, *Appl. Opt.*, 22, 2951–2959, doi:10.1364/AO.22.002951, 1983.
- Nousiainen, T.: Optical modeling of mineral dust particles: A review, *J. Quant. Spectrosc. Radiat. Transfer*, 110, 1261–1279, doi:10.1016/j.jqsrt.2009.03.002, 2009.
- O'Neill, N. T. and Miller, J. R.: Combined solar aureole and solar beam extinction measurements. 2: Studies of the inferred aerosol size distributions, *Appl. Opt.*, 23, 3697–3704, doi:10.1364/AO.23.003697, 1984.
- O'Neill, N. T., Eck, T. F., Smirnov, A., Holben, B. N., and Thulasiraman, S.: Spectral discrimination of coarse and fine mode optical depth, *J. Geophys. Res.*, 108, 4559, doi:10.1029/2002JD002975, 2003.
- Osterloh, L., Böckmann, C., Mamouri, R. E., and Papayannis, A.: An Adaptive Base Point Algorithm for the Retrieval of Aerosol Microphysical Properties, *The Open Atmospheric Science Journal*, 5, 61–73, doi:10.2174/1874282301105010061, 2011.

- Patterson, E. M., Pollard, C. O., and Galindo, I.: Optical properties of the ash from El Chichon Volcano, *Geophys. Res. Lett.*, 10, 317–320, doi:10.1029/GL010i004p00317, 1983.
- Penttilä, A., Zubko, E., Lumme, K., Muinonen, K., Yurkin, M. A., Draine, B., Rahola, J., Hoekstra, A. G., and Shkuratov, Y.: Comparison between discrete dipole implementations and exact techniques, *J. Quant. Spectrosc. and Radiat. Transf.*, 106, 417 – 436, doi:10.1016/j.jqsrt.2007.01.026, 2007.
- Petzold, A., Müller, D., Ansmann, A., Weinzierl, B., Esselborn, M., Reitebuch, O., Wiegner, M., Gasteiger, J., Buras, R., Mayer, B., van Zadelhoff, G.-J., Donovan, D., and Berthier, S.: STSE ICAROHS - Final Report, Tech. rep., ESA Contract No 22169/NL/CT, 2011.
- Pieri, D., Ma, C., Simpson, J. J., Hufford, G., Grindle, T., and Grove, C.: Analyses of in-situ airborne volcanic ash from the February 2000 eruption of Hekla Volcano, Iceland, *Geophys. Res. Lett.*, 29, doi:10.1029/2001GL013688, 2002.
- Piller, N. B. and Martin, O. J. F.: Increasing the performance of the coupled-dipole approximation: a spectral approach, *IEEE Transactions on Antennas and Propagation*, 46, 1126–1137, doi:10.1109/8.718567, 1998.
- Purcell, E. and Pennypacker, C.: Scattering and Absorption of Light by Nonspherical Dielectric Grains, *Astrophysical Journal*, 186, 705–714, doi:10.1086/152538, 1973.
- Ramachandran, G. and Kandlikar, M.: Bayesian analysis for inversion of aerosol size distribution data, *J. Aerosol Sci.*, 27, 1099 – 1112, doi:10.1016/0021-8502(96)00005-5, 1996.
- Rayleigh, L.: On the incidence of aerial and electric waves upon small obstacles in the form of ellipsoids or elliptic cylinders, and on the passage of electric waves through a circular aperture in a conducting screen, *Phil. Mag.*, 44, 28–52, doi:10.1080/14786449708621026, 1897.
- Reid, J. S., Jonsson, H. H., Maring, H. B., Smirnov, A., Savoie, D. L., Cliff, S. S., Reid, E. A., Livingston, J. M., Meier, M. M., Dubovik, O., and Tsay, S.: Comparison of size and morphological measurements of coarse mode dust particles from Africa, *J. Geophys. Res.*, 108, 8593, doi:10.1029/2002JD002485, 2003a.
- Reid, J. S., Kinney, J. E., Westphal, D. L., Holben, B. N., Welton, E. J., Tsay, S., Eleuterio, D. P., Campbell, J. R., Christopher, S. A., Colarco, P. R., Jonsson, H. H., Livingston, J. M., Maring, H. B., Meier, M. L., Pilewskie, P., Prospero, J. M., Reid, E. A., Remer, L. A., Russell, P. B., Savoie, D. L., Smirnov, A., and Tanré, D.: Analysis of measurements of Saharan dust by airborne and ground-based remote sensing methods during the Puerto Rico Dust Experiment (PRIDE), *J. Geophys. Res.*, 108, 8586, doi:10.1029/2002JD002493, 2003b.

- Sanderson, K.: Out of the ashes, *Nature*, 465, 544–545, doi:10.1038/465544a, 2010.
- Sassen, K., DeMott, P. J., Prospero, J. M., and Poellot, M. R.: Saharan dust storms and indirect aerosol effects on clouds: CRYSTAL-FACE results, *Geophys. Res. Lett.*, 30, 1633, doi:10.1029/2003GL017371, 2003.
- Sassen, K., Zhu, J., Webley, P., Dean, K., and Cobb, P.: Volcanic ash plume identification using polarization lidar: Augustine eruption, Alaska, *Geophys. Res. Lett.*, 34, doi:10.1029/2006GL027237, 2007.
- Satheesha, S. K. and Moorthy, K. K.: Radiative effects of natural aerosols: A review, *Atm. Env.*, 39, 2089–2110, doi:10.1016/j.atmosenv.2004.12.029, 2005.
- Schelkunoff, S. A.: Some Equivalence Theorems of Electromagnetics and Their Application to Radiation Problems, *Bell Sys. Tech. J.*, 15, 92–112, 1936.
- Schladitz, A., Müller, T., Nordmann, S., Tesche, M., Groß, S., Freudenthaler, V., and Wiedensohler, A.: In-situ aerosol characterization at Cape Verde. Part 2: Parameterization of relative humidity- and wavelength-dependent aerosol optical properties, *Tellus B*, 63, 549–572, doi:10.1111/j.1600-0889.2011.00568.x, 2011.
- Schmid, B. and Wehrli, C.: Comparison of Sun photometer calibration by use of the Langley technique and the standard lamp, *Appl. Opt.*, 34, 4500–4512, doi:10.1364/AO.34.004500, 1995.
- Schumann, U., Weinzierl, B., Reitebuch, O., Schlager, H., Minikin, A., Forster, C., Baumann, R., Sailer, T., Graf, K., Mannstein, H., Voigt, C., Rahm, S., Simmet, R., Scheibe, M., Lichtenstern, M., Stock, P., Rüba, H., Schäuble, D., Tafferner, A., Rautenhaus, M., Gerz, T., Ziereis, H., Krautstrunk, M., Mallaun, C., Gayet, J.-F., Lieke, K., Kandler, K., Ebert, M., Weinbruch, S., Stohl, A., Gasteiger, J., Groß, S., Freudenthaler, V., Wiegner, M., Ansmann, A., Tesche, M., Olafsson, H., and Sturm, K.: Airborne observations of the Eyjafjalla volcano ash cloud over Europe during air space closure in April and May 2010, *Atmos. Chem. Phys.*, 11, 2245–2279, doi:10.5194/acp-11-2245-2011, 2011.
- Shaw, G. E.: Inversion of optical scattering and spectral extinction measurements to recover aerosol size spectra, *Appl. Opt.*, 18, 988–993, doi:10.1364/AO.18.000988, 1979.
- Shaw, G. E.: Sun photometry, *Bull. Amer. Meteor. Soc.*, 64, 4–10, doi:10.1175/1520-0477(1983)064<0004:SP>2.0.CO;2, 1983.
- Sokolik, I. N. and Toon, O. B.: Incorporation of mineralogical composition into models of the radiative properties of mineral aerosol from UV to IR wavelengths, *J. Geophys. Res.*, 104, 9423–9444, doi:10.1029/1998JD200048, 1999.
- Stamnes, K., Tsay, S.-C., Wiscombe, W., and Jayaweera, K.: Numerically stable algorithm for discrete-ordinate-method radiative transfer in multiple scattering and emitting layered media, *Appl. Opt.*, 27, 2502–2509, doi:10.1364/AO.27.002502, 1988.

- Tanré, D., Haywood, J., Pelon, J., Léon, J. F., Chatenet, B., Formenti, P., Francis, P., Goloub, P., Highwood, E. J., and Myhre, G.: Measurement and modeling of the Saharan dust radiative impact: Overview of the Saharan Dust Experiment (SHADE), *J. Geophys. Res.*, 108, 8574, doi:10.1029/2002JD003273, 2003.
- Tarantola, A.: Popper, Bayes and the inverse problem, *Nature Physics*, 2, 492–494, doi:10.1038/nphys375, 2006.
- Tesche, M., Ansmann, A., Müller, D., Althausen, D., Mattis, I., Heese, B., Freudenthaler, V., Wiegner, M., Esselborn, M., Pisani, G., and Knippertz, P.: Vertical profiling of Saharan dust with Raman lidars and airborne HSRL in southern Morocco during SAMUM, *Tellus B*, 61, 144–164, doi:10.1111/j.1600-0889.2008.00390.x, 2009.
- Tesche, M., Groß, S., Ansmann, A., Müller, D., Althausen, D., Freudenthaler, V., and Esselborn, M.: Profiling of Saharan dust and biomass burning smoke with multiwavelength polarization Raman lidar at Cape Verde, *Tellus B*, 63, 649–676, doi:10.1111/j.1600-0889.2011.00548.x, 2011.
- Thomalla, E. and Quenzel, H.: Information content of aerosol optical properties with respect to their size distribution, *Appl. Opt.*, 21, 3170–3177, doi:10.1364/AO.21.003170, 1982.
- Toledano, C., Wiegner, M., Garhammer, M., Seefeldner, M., Gasteiger, J., Müller, D., and Koepke, P.: Spectral aerosol optical depth characterization of desert dust during SAMUM 2006, *Tellus B*, 61, 216–228, doi:10.1111/j.1600-0889.2008.00382.x, 2009.
- Toledano, C., Wiegner, M., Groß, S., Freudenthaler, V., Gasteiger, J., Müller, D., Müller, T., Schladitz, A., Torres, B., and O’Neill, N. T.: Optical properties of aerosol mixtures derived from sun-sky radiometry during SAMUM-2, *Tellus B*, 63, 435–448, doi:10.1111/j.1600-0889.2011.00573.x, 2011.
- Valery, A., Cartwright, R., Fausett, E., Ossipov, A., Pasko, E., and Savchenko, V.: HyperFun project: a framework for collaborative multidimensional F-rep modeling, *Eurographics/ACM SIGGRAPH Workshop Implicit Surfaces 99*, Bordeaux, France, 1999.
- van de Hulst, H. C.: *Light Scattering by Small Particles*, Dover Publications, New York, 1981.
- Veselovskii, I., Dubovik, O., Kolgotin, A., Lapyonok, T., Di Girolamo, P., Summa, D., Whiteman, D. N., Mishchenko, M., and Tanré, D.: Application of randomly oriented spheroids for retrieval of dust particle parameters from multiwavelength lidar measurements, *J. Geophys. Res.*, 105, D21 203, doi:10.1029/2010JD014139, 2010.
- Wandinger, U.: Introduction to Lidar, in: *LIDAR: Range-Resolved Optical Remote Sensing of the Atmosphere*, edited by Weitkamp, C., pp. 1–18, Springer, doi:10.1007/0-387-25101-4_1, 2005.

- Waterman, P.: Symmetry, unitarity, and geometry in electromagnetic scattering, *Phys. Rev. D*, 4, 825–839, doi:10.1103/PhysRevD.3.825, 1971.
- Weinzierl, B.: Radiatively-driven processes in forest fire and desert dust plumes, Dissertation, Fakultät für Physik, LMU Munich, Germany, 2008.
- Weinzierl, B., Petzold, A., Esselborn, M., Wirth, M., Rasp, K., Kandler, K., Schütz, L., Koepke, P., and Fiebig, M.: Airborne measurements of dust layer properties, particle size distribution and mixing state of Saharan dust during SAMUM 2006, *Tellus B*, 61, 96–117, doi:10.1111/j.1600-0889.2008.00392.x, 2009.
- Weinzierl, B., Sauer, D., Esselborn, M., Petzold, A., Veira, A., Rose, M., Mund, S., Wirth, M., Ansmann, A., Tesche, M., Groß, S., and Freudenthaler, V.: Microphysical and optical properties of dust and tropical biomass burning aerosol layers in the Cape Verde region - An overview of the airborne in situ and lidar measurements during SAMUM-2, *Tellus B*, 63, 589–618, doi:10.1111/j.1600-0889.2011.00566.x, 2011.
- Weitkamp, C., ed.: *LIDAR: Range-Resolved Optical Remote Sensing of the Atmosphere*, Springer, 2005.
- Wiegner, M.: Potential of ceilometers for aerosol remote sensing: a preliminary assessment, Proc. of 25th International Laser Radar Conference, St. Petersburg, Russia, 5-9 July 2010, S07P-05, 2010.
- Wiegner, M., Gasteiger, J., Kandler, K., Weinzierl, B., Rasp, K., Esselborn, M., Freudenthaler, V., Heese, B., Toledano, C., Tesche, M., and Althausen, D.: Numerical simulations of optical properties of Saharan dust aerosols with emphasis on lidar applications, *Tellus B*, 61, 180–194, doi:10.1111/j.1600-0889.2008.00381.x, 2009.
- Wiegner, M., Gasteiger, J., Groß, S., Schnell, F., Freudenthaler, V., and Forkel, R.: Characterization of the Eyjafjallajökull ash-plume: Potential of lidar remote sensing, *Physics and Chemistry of the Earth, Parts A/B/C*, In Press, doi:10.1016/j.pce.2011.01.006, 2011a.
- Wiegner, M., Groß, S., Freudenthaler, V., Schnell, F., and Gasteiger, J.: The May/June 2008 Saharan dust event over Munich: Intensive aerosol parameters from lidar measurements, *J. Geophys. Res.*, 116, D23 213, doi:10.1029/2011JD016619, 2011b.
- Yang, P. and Liou, K. N.: Geometric-optics-integral-equation method for light scattering by nonspherical ice crystals, *Appl. Opt.*, 35, 6568–6584, doi:10.1364/AO.35.006568, 1996.
- Yang, P., Feng, Q., Hong, G., Kattawar, G. W., Wiscombe, W. J., Mishchenko, M. I., Dubovik, O., Laszlo, I., and Sokolik, I. N.: Modeling of the scattering and radiative properties of nonspherical dust-like aerosols, *Journal of Aerosol Science*, 38, 995–1014, doi:10.1016/j.jaerosci.2007.07.001, 2007.

-
- Yurkin, M. A. and Hoekstra, A. G.: The discrete dipole approximation: An overview and recent developments, *J. Quant. Spectrosc. Radiat. Transf.*, 106, 558 – 589, doi:10.1016/j.jqsrt.2007.01.034, 2007.
- Yurkin, M. A. and Hoekstra, A. G.: The discrete-dipole-approximation code ADDA: Capabilities and known limitations, *J. Quant. Spectrosc. Radiat. Transf.*, 112, 2234 – 2247, doi:10.1016/j.jqsrt.2011.01.031, 2011.
- Yurkin, M. A., Min, M., and Hoekstra, A. G.: Application of the discrete dipole approximation to very large refractive indices: Filtered coupled dipoles revived, *Phys. Rev. E*, 82, 036 703, doi:10.1103/PhysRevE.82.036703, 2010.
- Zubko, E., Muinonen, K., Shkuratov, Y., Videen, G., and Nousiainen, T.: Scattering of light by roughened Gaussian random particles, *J. Quant. Spectrosc. Radiat. Transfer*, 106, 604–615, doi:10.1016/j.jqsrt.2007.01.050, 2007.

Acknowledgements

First of all, I like to thank Dr. Matthias Wiegner for giving me the opportunity to work in this interesting research field. Numerous fruitful discussions with him helped me to proceed effectively in this work. I am grateful to my supervisors Prof. Dr. Bernhard Mayer and apl. Prof. Dr. Ulrich Schumann for their support and suggestions that helped me to improve this thesis.

This work was done at the Meteorological Institute of the Ludwig-Maximilians-Universität in Munich. My colleagues Dr. Silke Groß and Dr. Volker Freudenthaler provided lidar data that was crucial for this work. I want to thank them, in particular also for their good support on the data. I thank Dr. Peter Köpke, Dr. Carlos Toledano, Franziska Schnell, and Markus Garhammer for useful discussions on aerosol-related topics.

I am much obliged to colleagues from other institutes with whom I had the opportunity to collaborate. In particular, in the framework of the SAMUM campaigns, observation data of desert dust aerosols from and/or discussions with Dr. Konrad Kandler, Dr. Detlef Müller, Dr. Albert Ansmann, Dr. Matthias Tesche, Dr. Andreas Petzold and Dr. Bernadett Weinzierl provided important input for this work. I thank Dr. Roman Schuh for providing the tool 'pip' for the creation of ADDA shape files and Dr. Jochen Wauer for suggestions on testing the accuracy of ADDA.

Funding by the European Council under grant 025991 (EARLINET-ASOS), by the Helmholtz-Gemeinschaft under grant VH-VI-156 (HALO), by the European Union under grant 4089 (AMMA), and by the European Space Agency under contracts 18366/04/NL/MM (ADM), 21487/08/NL/HE (ESA-Calipso), 22169/NL/CT (ICAROHS) is acknowledged.

Schließlich möchte ich besonders meiner Familie für ihre Geduld und Unterstützung während der Zeit dieser Arbeit danken.

Lebenslauf

Josef Konrad Gasteiger, geboren am 26. November 1980 in Rosenheim

- | | |
|------------------------|--|
| Sept. 1987 - Juli 1991 | Besuch der Grundschule in Rosenheim/Aising |
| Sept. 1991 - Juli 1995 | Besuch des Finsterwalder-Gymnasiums in Rosenheim |
| Sept. 1995 - Juni 2001 | Besuch des Chiemgau-Gymnasiums in Traunstein
Abschluss: Abitur |
| Juli 2001 - Mai 2002 | Zivildienst im Kreiskrankenhaus in Bad Aibling |
| Okt. 2002 - Sept. 2007 | Studium der Meteorologie an der
Ludwig-Maximilians-Universität in München
Abschluss: Diplom Meteorologie |
| Nov. 2007 - Sept. 2011 | Arbeiten an der Dissertation am
Meteorologischen Institut der
Ludwig-Maximilians-Universität in München |